To the Graduate Council:

I am submitting herewith a thesis written by Aubrey L. Modi entitled "Processes controlling the composition of first-cycle sediments deposited in an arid-climate, with implications for provenance reconstruction studies." I have examined the final electronic copy of this thesis for form and content and recommend that it be accepted in partial fulfillment of the requirements for the degree of Master of Science, with a major in Geology.

Chris M. Fedo, Major Professor

We have read this thesis
and recommend its acceptance:

Devon M. Burr

Hap Y. McSween

Accepted for the Council:

Carolyn R. Hodges

Vice Provost and Dean of the Graduate School

(Original signatures are on file with official student records.)

Processes controlling the composition of first-cycle sediments deposited in an arid-climate, with implications for provenance reconstruction studies

A Thesis Presented for the
Master of Science
Degree
The University of Tennessee, Knoxville

Aubrey Lynn Modi
December 2011

Acknowledgements

I would like to thank the Department of Earth and Planetary Sciences at The University of Tennessee Knoxville, especially those that have helped me complete this research. The generous efforts many faculty members and several of my peers are greatly appreciated. Thank you to Chris Fedo, for his patience and insight, as well as my committee members, Devon Burr and Hap McSeween, for critical feedback and revisions. Additionally, thank you to my fellow graduate students for their support and encouragement, specifically Liz Lee, Eric Hogan, Rachel Storniolo, Cara Thompson, Matt Chojnacki, Kevin Thaisen, Melissa Hage, Ian McGlynn, Arya Udry, Meghan Janzen, and Heather Byars. Finally, thank you to my parents for their continued support through my year as a graduate student.

Abstract

Petrologic analysis of first-cycle clastic sediments derived from a single source in an arid environment provides a means to determine how well they resemble the petrology and geochemistry of their source. The Stepladder Mountains, located in the Mojave Desert of southeastern California, represents a well-controlled location (i.e., arid environment; single, known source; short transport distance) to examine how naturally formed sediments acquire their compositions. Compositional modifications associated with sediment production were resolved through direct examination of the weathered components (regolith, grus, and sediments). Sediment compositions strongly vary by grain size, indicating that, after the source itself, hydrodynamic sorting played the dominant role in shaping the composition of Stepladder sediment.

Traditional petrographic and geochemical provenance-seeking indicators were also tested to determine their efficacy. Plots employing major element abundances, including Al_2O_3–CaO^*+Na_2O–K_2O (A–CN–K) and Al_2O_3–CaO^*+Na_2O+K_2O–Fe_2O_3+MgO (A–CNK–FM) ternary plots, proved to be the most accurate at identifying the lack of chemical weathering and the importance of sediment sorting in the production of Stepladder sediments. Plots using trace and rare earth element concentrations reveal the significant modifications that sorting can have on sediment composition. All of the Stepladder sediments are enriched in immobile transition metals, most notably Sc, Cr, Ni, and Co, and even though the sediment sourced from a single pluton, compositions are consistent with the mixing of 10 - 20 % of a basaltic component. Sediment trace element ratios, including Th/Sc, Cr/Th, La/Sc, Th/Co, and Zr/Sc, can differ from average bedrock by up to a factor of 10. It must be known that moderate variations in composition and elemental ratios can be the result of sorting during sediment transport and do not necessarily indicate the mixing between sources.

TABLE OF CONTENTS

1. Introduction **1**
2. Geologic Setting **3**
3. Material and Methods **6**
3.1. Sample collection and preparation *6*
3.2. Textural and mineralogical analyses *7*
3.3. Geochemical analyses *10*
4. Compositional influence of caliche **10**
5. Characterization of the source rock: Stepladder granodiorite **18**
5.1. Petrology *18*
5.2. Geochemistry *21*
5.2.1. Major elements *21*
5.2.2. Rare earth and trace elements *22*
6. Characterization of the weathered source rock: Stepladder regolith and grus **29**
6.1. Petrology *29*
6.2. Geochemistry *33*
6.2.1. Major elements *33*
6.2.2. Rare earth and trace elements *33*
7. Characterization of Stepladder sediments **34**
7.1. Rationale for sample grouping *34*
7.2. Sedimentary petrology – Textures *35*
7.2.1. Gravel group (G) *35*
7.2.2. Very coarse sand group (VC) *35*
7.2.3. Coarse sand group (C) *37*
7.2.4. Medium sand group (M) *37*
7.2.5. Fine sand group (F) *38*
7.2.6. Very fine sand group (VF) *38*
7.3. Sedimentary petrology – Mineralogy *39*
7.3.1 Quartz *39*
7.3.2 Plagioclase *39*
7.3.3 K-feldspar *42*
7.3.4 Biotite *42*
7.3.5 Accessory phases *43*
7.3.6 Modal mineralogy *43*
7.4 Geochemistry *46*
7.4.1. Major elements *46*
7.4.2. Rare earth and trace elements *46*
8. Provenance reconstruction **49**
8.1. A–CN–K and A–CNK–FM plots *49*
8.2. Rare earth element plots *50*
8.2.1. Eu and Ce anomalies *51*
8.3. Trace element plots *54*
8.3.1. Th/Sc vs. Sc (ppm) *55*

8.3.2. Cr/Th vs. Th/Sc *58*
8.3.3. Th/Co vs. La/Sc *59*
8.3.4. Cr (ppm) vs. Ni (ppm) *61*
8.3.5. Cr/V vs. Y/Ni *61*
8.4. Utility of diagrams and indicators *63*
9. Factors influencing compositional changes 63
9.1. Chemical and physical weathering *63*
9.2. Sediment transport and sorting *64*
10. Conclusions 70
References 72
Appendix 1: Stepladder sample descriptions 89
Appendix 2: Supplemental geochemical material........144
Vita........156

LIST OF TABLES

Table **Page**

Table 1. Textural classification of Stepladder sediment samples. 8

Table 2. Point-counted modes of Stepladder sediments. 9

Table 3. Major element analysis of Stepladder samples... 11

Table 4. Trace element analysis of Stepladder samples 12

Table 5. Chondrite-normalized REE ratios of Stepladder samples. 27

Table 6. Average bedrock-normalized REE ratios of Stepladder samples. 28

LIST OF FIGURES

Figure **Page**

Figure 1. Maps and cross-section of Stepladder region and field site 4

Figure 2. Plots showing the influence of caliche on bedrock composition 17

Figure 3. Photographs and geochemical plots of fresh Stepladder bedrock 19

Figure 4. A–CN–K plots showing weathering trend of average fresh bedrock and Stepladder samples.. 23

Figure 5. A–CNK–FM plots showing weathering trend of average fresh bedrock and Stepladder samples.. 25

Figure 6. Photographs and geochemical plots of Stepladder regolith and grus........................... 30

Figure 7. Frequency and cumulative curves of sediment samples grouped by mean grain size .. 36

Figure 8. Photographs and geochemical plots of Stepladder sediments...................................... 40

Figure 9. QFL, QPK, and QFB plots of Stepladder sediments grouped by grain size 44

Figure 10. Average bedrock-normalized REE plots of sediment grain-size groups..................... 48

Figure 11. Bedrock-normalized Eu* and Ce* plots 52

Figure 12. Compatible vs. incompatible trace element plots... 56

Figure 13. High field strength element plots 62

Figure 14. Discrimination diagrams typically used to recognize sorting and sediment recycling... 68

1. Introduction

Understanding sediment origin, weathering intensity, and sedimentary processes, such as hydraulic sorting, are key components for reconstructing the provenance of clastic sedimentary rocks (Haughton et al., 1991; Johnsson, 1993). Because sediment composition is primarily controlled by its source rock and the modifications that occur during transport from source to basin (Johnsson, 1993), it is essential to understand how processes associated with weathering, erosion, and transport physically and chemically fractionate clastic material. Determining sedimentary provenance is, therefore, limited on the ability to recognize and interpret provenance signals that have been preserved in sediment following the above processes. Unfortunately, the variables tested often represent parameters that can no longer be directly confirmed because much of the source-to-sediment system has not been preserved (Johnsson, 1993). Consequently, such studies rely on geochemical and petrographic provenance indicators to interpret bulk provenance characteristics. Despite their extensive use, many of these provenance indicators still require rigorous, first-principle analyses of modern, high-precision analytical data (Armstrong-Altrin and Verma, 2005; Ryan and Williams, 2007). Similar studies exposed a breakdown in the utility of tectonic discrimination diagrams, which were unable to correctly identify the tectonic setting of sediments from a mixed or geochemically unique provenance (Armstrong-Altrin and Verma, 2005; Ryan and Williams, 2007). A related investigation revealed that geochemical discrimination diagrams were unable to distinguish between sediment provenances of similar geology (Pe-Piper et al., 2008); another displayed that physical and chemical weathering can affect important major and trace elemental ratios linked to provenance interpretation (Totten et al., 2000; Nesbitt and Young, 1984, 1996). Such findings call attention to the continued need for controlled studies that identify the factors that influence provenance signatures, which is a primary motive of this paper.

The history of bulk compositional provenance research and the development of petrographic and geochemical indicators are extensive. Petrographic provenance techniques have evolved from the pioneering work of Dickinson (1970), Basu et al. (1975), Dickinson and Suczek (1979), Dickinson et al. (1983), and Ingersoll et al. (1984), which used detrital modes in sedimentary rocks to develop tectonic discrimination diagrams linking sediment provenance to major plate settings. Other petrographic modal analyses by Basu (1976) and Suttner et al. (1981) explored the climactic signals recorded in sediments and sedimentary rocks. Early research using major and trace element compositions worked to understand sedimentary geochemistry (e.g., Nesbitt, 1979; Taylor and McLennan, 1985; Cullers, 1988; Cullers et al., 1988, Nesbitt and Young, 1989; Basu et al., 1990; McLennan et al., 1993), to identify geochemical signatures recorded in sediment over time (Wronkiewicz and Condie, 1987; McLennan and Taylor, 1991; Dinelli et al., 1999), and to recognize specific sedimentary processes, such as hydraulic sorting, sediment recycling, and source mixing (McLennan et al., 1993, 2006). Taylor and McLennan (1981) noted that elements with low solubility and mobility preserve a stronger record of the source rock composition than elements that are readily soluble. Because trace elements, such as rare earth elements (REE) and select high field strength elements (HFSE), are considered relatively immobile and are thought to not fractionate appreciably during weathering (Taylor and McLennan, 1985), the chemical composition of clastic materials has continually been relied on to determine bulk provenance composition (Basu et al., 1982; Fralick and Kromberg, 1997; Roddaz et al., 2006; Fuenlabrada et al., 2010; Hossain et al., 2010).

This study evaluates the effectiveness and limitations of a number of provenance-seeking, geochemical and petrographic indicators by determining how well first-cycle siliciclastic sediments derived from a known single source resemble their source bedrock composition. Although such an approach follows on pioneering studies (e.g. Cullers, 1988; Cullers et al., 1988), this study uses elementally extensive, high-precision analytical data not available at that time. In order to control variables as much as possible, the research examines a sediment drape that mantles a granitic bedrock with limited compositional variability, and that was deposited in a relatively arid paleoclimate where the effect of chemical weathering would be minimized. The geologic setting of the field site provides the ability to identify, and subsequently evaluate, source rock composition, chemical and physical weathering processes, sediment transport, climate, and tectonic setting. If provenance indicators have the ability to reconstruct the sedimentary history of clastic material and identify its bedrock source(s), then they should unambiguously connect Stepladder sediment to its source rock in this study.

2. Geologic Setting

The study area lies within the Mojave Desert of southeastern California, at the northern end of the Stepladder Mountains (Fig. 1A). Because little work has been done on the Stepladder pluton (e.g., Miller and Miller, 1991; Foster et al., 1990), its emplacement, exposure, and erosional history must be inferred from studies in adjacent ranges (Foster et al., 1990; Kingsbury et al., 1993; John and Foster, 1993; McCaffrey et al., 1999). Regional cratonization began in the middle Proterozoic and continued until the middle Paleozoic to early Mesozoic (Miller et al., 1990) when activation of the western continental margin spurred thrust faulting, magmatism, and metamorphism (Anderson and Cullers, 1990). Coeval with Cordilleran mid-crustal thickening and peak regional metamorphism, middle and Late Cretaceous plutons intruded Proterozoic and

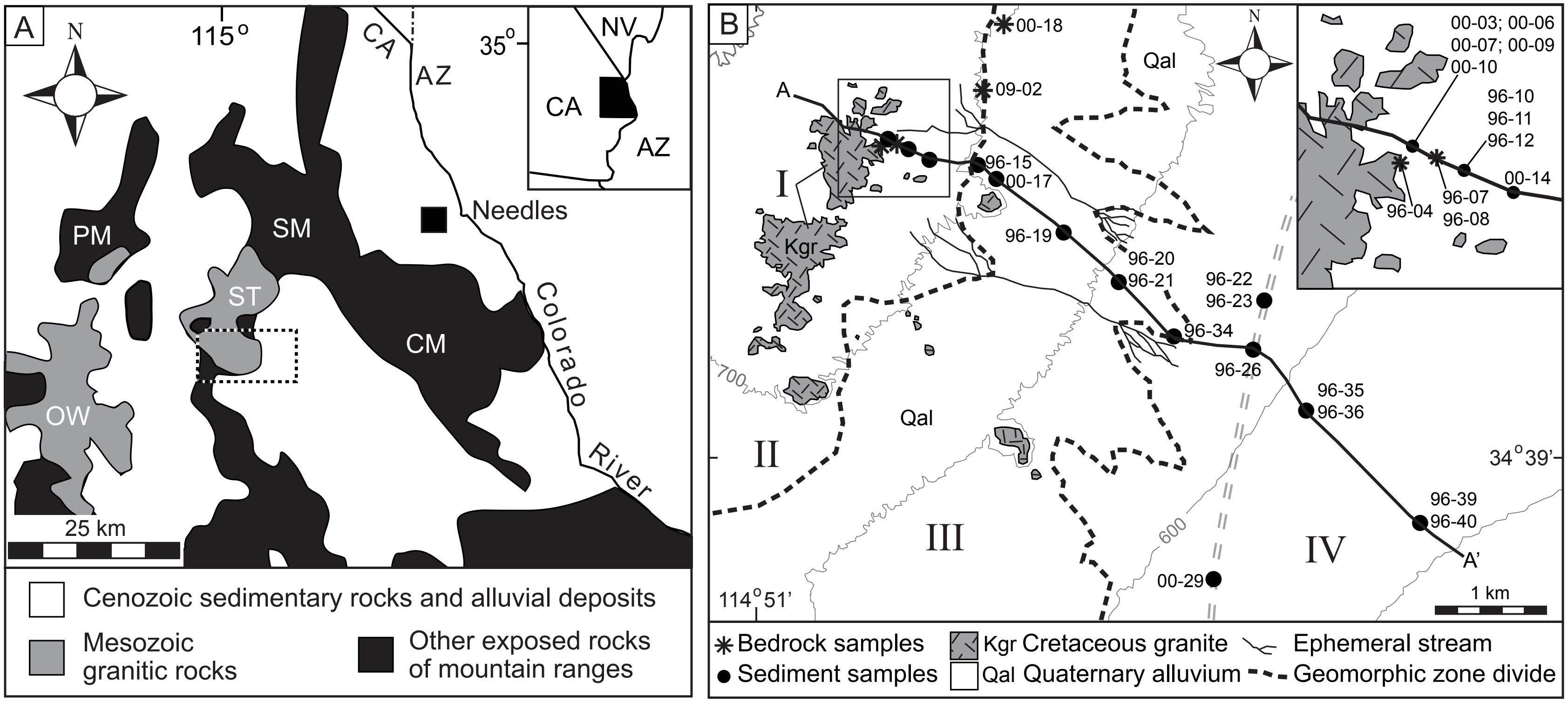

Figure 1. Maps and cross-section of Stepladder region and field site. (A) Simplified geologic map of southeast California showing surrounding mountain ranges (see inset for location); boxed area shows location of (B). Abbreviations = CM: Chemeheuvi Mountains; OW: Old Woman Mountains; PM: Piute Mountains; SM: Sacramento Mountains; ST: Stepladder Mountains. Modified from Fletcher and Karlstrom (1990). (B) Topographic map of field site showing exposed Stepladder bedrock and sample locations. I-IV: geomorphic zones discussed in text. See inset for enlargement of sample locations near exposed bedrock; transect A–A' shows location of (C) topographic profile. (C) Simplified cross section with sample locations (black dots) and labeled geomorphic zones.

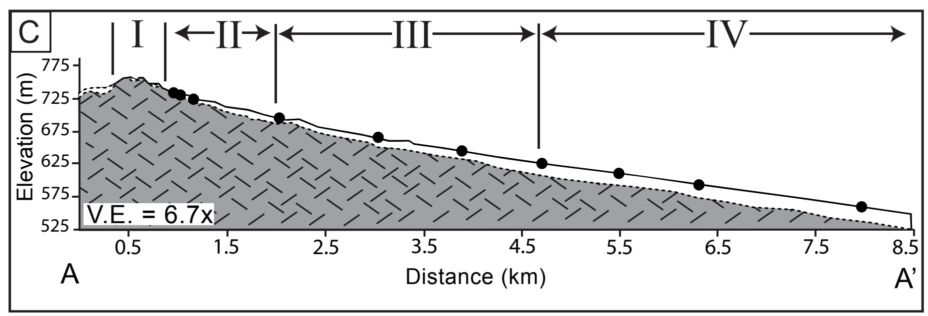

Paleozoic basement (Fletcher and Karlstrom, 1990; Miller and Miller, 1991; Karlstrom et al., 1993; Miller and Wooden, 1994). Rapid uplift and exhumation of the Stepladder and surrounding plutons occurred coevally with Tertiary volcanism (ca. 22-14 Ma; Miller et al., 2000), detachment faulting (Anderson and Cullers, 1990), and regional-scale lithospheric extension (Hileman et al., 1990; Miller et al., 2000).

Bedrock exposures of the granodioritic Stepladder pluton occur as a string of NNE-trending rocky ridges (Fig. 1B) that rise from a pediment dome. A veneer of poorly sorted, autochthonous sediment, ranging in grain size from clay to gravel, mantles the gently sloping bedrock and piedmont (Fig. 1C). Caliche is found as locally developed, thin (< 4 cm) crusts on indurated surfaces and as irregular, rounded grains that contaminate all of the sediment samples to a small degree. The compositional influence of caliche on the Stepladder sediment composition is discussed below.

Cosmogenic nuclide data (Nichols et al., 2005, 2007) document southern Mojave Desert piedmont processes, including sediment erosion, transportation, and deposition, over the past 60,000 years. Sediment deposition persisted through the last interstade (60-30 ka), but ceased around the Pleistocene-Holocene transition when the climate dried and the vegetation cover decreased. During mid-Holocene pluvial events, increased storm magnitude and runoff drove channel incision and spurred distal piedmont aggradation (Nichols et al., 2002). Compared to Pleistocene surfaces, modern piedmonts are stable or, in distal zones, actively transporting sediment. The sparse vegetation, low sloping surfaces, and arid (< 6 cm of rain per year; NOAA, 2010) hot climate prevents significant erosion or aggradation. Instead, sporadic rain events, occurring as short, but intense, summer cyclonic storms or as long, relatively mild, winter fronts (NOAA, 2010), transport sediments decimeters to meters each year (Nichols et al., 2002, 2005).

The study site is divided into four geomorphic zones as defined by topographic and geomorphic features (Fig. 1B). Zone I comprises a series of meter-scale-relief, jointed inselburgs of granodiorite that forms the topographic high point in the study area (Fig. 1C). In contact with the pluton is zone II, which consists of small bedrock knobs mantled by boulders and meter-thick patches of varnished alluvium, all of which are incised by channels up to 3 m deep. Beginning where channels converge about 1 km from pluton exposures, zone III is dissected by a series of sub-parallel and weakly integrated channels. Zone IV starts about 4-6 km from the Stepladder front where the isolated channels shallow and bifurcate, the incised surface smoothes, and the low-sloping wash sheet thickens to completely bury bedrock.

3. Material and Methods

3.1. Sample collection and preparation

One hundred six (106) samples, representing bedrock, grus and sediment from the geomorphic zones and spanning all grain sizes, were collected during three field seasons (1996, 2000, and 2009). From the total collection of samples, 38 were selected for geochemical and petrographic analysis, including 4 fresh granodiorite samples, 3 weathered bedrock samples (2 regolith, 1 grus), 4 minor plutonic phases, 1 caliche sample, and 24 sediment samples. Sediment samples were selected to ensure that all grain sizes of the site were represented, regardless of geomorphic zone.

All sediments were dried at 55 °C for at least 24 hours prior to preparation for geochemical analysis, thin section mounting, and sediment sieving. Sediments were coned-and-quartered into 25 g and 10 g aliquots in preparation for geochemical analysis and thin-section production, respectively. The 25 g aliquots were crushed in a jaw crusher and then powdered for two minutes in a ceramic shatterbox dish. Approximately 10 mg of each powdered sample was kept to determine total-carbonate CO_2 by coulometry. For epoxy mount preparation, the 10 g aliquots were mixed with epoxy, vacuum impregnated, dried, and cut into discs, which were made into conventional 30 μm-thick thin-sections.

3.2. Textural and mineralogical analyses

The remaining sediment of each sample (approximately 70-80 g for the finer-grained samples and 200-250 g for coarser-grained samples) was sieved into eight, single-phi, grain-size fractions from -2 to 5 Φ (4 to 0.03 mm; Table 1). The 24 samples naturally define six grain-size-distribution groups (Table 1) that are further characterized by their graphic mean, median, range, sorting, modality, kurtosis, and skewness (Folk, 1974). Four samples were assigned to the gravel group (*G*), three to the very coarse sand group (*VC*), six to the coarse sand group (*C*), three to the medium sand group (*M*), six to the fine sand group (*F*), and two to the very fine sand group (*VF*).

Loose sediment and thin sections were analyzed with a Nikon SMZ-800 stereo zoom microscope and a Nikon LV100D POL polarizing petrographic microscope, respectively. Modal analyses (Table 2) of the sediment thin sections followed a modified Gazzi-Dickinson point counting method (Dickinson, 1970; Ingersoll et al., 1984). Where possible, modal analyses of bedrock samples were calculated from 1000 points to acquire an accurate representation of accessory minerals (Table 2). For sediment samples, 300 to 700 points were counted depending on the grain-size of the sample, where the coarser groups had less counts.

Table 1. Textural classification of Stepladder sediment samples.

Sample	Geomorphic zone	Texture class[a]	Sorting[b]	Avg. rounding[c]	Mean grain size[d]	Kurtosis[e]	Skewness[f]	Grain size distribution (ϕ) in %								
								>-2	-1	0	1	2	3	4	<5	Total
Gravel Group (G)																
CF96-11	II	sG	P	1	-1.3	1.32	+0.2	27	40	21	6	4	1	0	0	100
CF00-10	II	sG	VP	1	-1.0	1.09	+0.2	33	22	15	9	7	6	4	4	100
CF96-36	IV	sG	VP	1	-1.1	0.89	+0.3	41	20	9	7	8	7	4	3	100
CF00-09	II	msG	VP	2	-0.3	0.72	+0.1	32	14	9	8	9	8	9	11	100
Very Coarse Sand Group (VC)																
CF96-40	IV	sG	P	1	-0.1	1.01	+0.2	14	22	19	17	13	8	4	2	100
CF96-22	IV	sG	P	1	-0.1	0.87	+0.2	11	25	20	18	16	8	3	1	100
CF00-07	II	gS	P	1	-0.2	1.04	0.0	8	20	28	27	12	2	1	1	100
Coarse Sand Group (C)																
CF96-19	III	gS	P	1	0.2	0.98	-0.1	9	14	20	23	22	10	2	0	100
CF96-12	II	gS	P	1	0.8	1.02	-0.1	1	6	15	32	35	9	1	0	100
CF96-15	II	(g)S	P	1	0.8	1.01	0.0	2	3	16	38	32	8	1	0	100
CF96-34	III	gS	P	1	0.7	0.94	-0.1	2	6	16	33	31	10	1	0	100
CF96-20	III	gS	P	2	0.4	1.02	-0.1	2	10	22	38	22	4	1	0	100
CF96-26	IV	gS	P	2	0.9	1.08	-0.1	3	5	15	25	34	14	2	1	100
Medium Sand Group (M)																
CF00-17	III	(g)S	MW	3	1.3	1.13	-0.1	0	1	8	26	42	19	3	1	100
CF00-06	II	gS	MW	3	1.5	2.17	-0.3	3	3	4	9	58	21	1	0	100
CF96-07	II	gmS	P	3	1.9	1.21	-0.2	6	6	5	10	23	25	17	9	100
Fine Sand Group (F)																
CF00-14	II	gmS	VP	2	1.4	0.62	-0.1	9	13	13	11	10	10	14	21	100
CF00-03	II	gmS	VP	2	1.5	0.69	-0.2	12	10	11	10	10	9	13	26	100
CF96-23	IV	gmS	VP	2	2.0	0.87	-0.4	9	6	7	9	10	16	21	22	100
CF00-29	IV	gmS	VP	2	2.5	0.71	-0.7	6	8	7	8	9	9	13	40	100
CF96-35	IV	gmS	VP	2	2.5	0.73	-0.7	4	9	7	8	7	8	17	40	100
CF96-39	IV	gS	P	2	2.6	0.81	-0.5	0	7	7	9	10	15	23	29	100
Very Fine Sand Group (VF)																
CF96-21	III	gS	P	3	3.1	1.11	-0.3	2	1	2	3	12	25	33	23	100
CF96-10	II	sG	P	3	3.5	1.02	-0.3	0	0	2	2	7	19	38	33	100

[a]Texture classifications after Folk (1974).

[b]Sorting calculations and classifications after Folk (1974); abbreviations = VP: very poorly sorted; P: poorly sorted; MW: moderately well sorted.

[c]Roundness determined using rho (ρ) scale from Folk (1955) and images of Powers (1953); scale ranges from 0 = very angular to 6 = well rounded.

[d]Grain size in phi (ϕ) units.

[e]Graphic kurtosis (from Folk, 1974): $K_G = \frac{(\Phi95-\Phi5)}{2.44(\Phi75-\Phi25)}$

[f]Inclusive graphic skewness (from Folk, 1974): $Sk_I = \frac{(\Phi16+\Phi84-2\Phi50)}{2(\Phi16+\Phi84)} + \frac{(\Phi5+\Phi95-2\Phi50)}{2(\Phi95+\Phi5)}$

Table 2. Point-counted modes of Stepladder sediments.

	Modal composition										QFL%			QPK%			QFB%		
Sample	Q	P	K	C_1	C_2	B	D	misc	Total	n	Q	F	L	Q	P	K	Q	F	B
Fresh Bedrock																			
ST09-02	25	41	27	0	*0*	6	1	1	100	997				27	45	29	30	63	7
CF00-18	28	40	23	0	*0*	7	1	0	100	1031				31	44	25	27	66	7
CF96-4	31	37	29	0	*0*	1	1	1	100	966				32	38	30	29	70	1
CF96-8	26	45	24	0	*0*	4	1	0	100	1019				27	48	25	27	69	4
Avg	28	41	26	0	*0*	5	1	0	100	*1003*				29	44	27	28	67	5
Regolith																			
CF00-04	27	38	27	0	*0.1*	6	2	0	100	1060				29	42	30	27	67	6
CF00-05	33	36	27	0	*0*	2	1	0	100	904				35	37	28	34	64	2
Grus																			
CF96-01	25	23	24	1	*0.5*	9	4	14	100	418				34	32	33	30	59	11
Gravel Group (G)																			
CF96-11	27	21	40	1	*0.3*	10	1	0	100	335	30	70	0	30	24	45	27	62	11
CF00-10	28	25	37	1	*2.3*	6	2	2	100	378	31	69	0	31	27	42	29	65	6
CF96-36	24	35	28	2	*2.3*	8	1	1	100	365	27	73	0	28	41	32	27	63	10
CF00-09	20	25	24	2	*1.4*	9	2	18	100	479	33	67	0	29	37	34	29	59	12
Very Coarse Sand Group (VC)																			
CF96-40	32	28	33	1	*1.2*	6	0	0	100	295	34	66	0	34	30	36	32	62	6
CF96-22	36	29	32	0	*2.3*	3	0	0	100	315	36	64	0	37	30	33	35	62	3
CF00-07	24	31	34	2	*1.8*	6	4	0	100	358	27	73	0	27	34	39	25	69	6
Coarse Sand Group (C)																			
CF96-19	23	40	28	3	*4.7*	4	3	0	100	356	27	73	0	26	44	31	26	70	4
CF96-12	27	41	26	0	*1.5*	6	1	0	100	342	28	72	0	29	44	28	26	68	6
CF96-15	28	36	23	0	*2.3*	10	1	1	100	345	27	73	0	32	41	27	29	61	10
CF96-34	30	38	24	2	*3.5*	5	1	0	100	308	33	67	0	33	41	26	31	64	5
CF96-20	31	29	28	1	*1.9*	9	3	0	100	336	35	65	0	35	33	32	32	59	9
CF96-26	28	34	24	0	*1.7*	11	1	1	100	392	33	67	0	33	40	28	29	60	11
Medium Sand Group (M)																			
CF00-17	24	39	23	2	*2.3*	9	3	0	100	495	25	75	0	28	45	27	26	65	10
CF00-06	21	38	24	2	*1.6*	13	2	0	100	496	26	74	0	25	46	29	22	64	14
CF96-07	20	38	21	3	*5.2*	14	3	0	100	451	29	71	0	25	48	26	20	65	15
Fine Sand Group (F)																			
CF00-14	17	21	19	14	*8.8*	10	2	19	100	448	29	71	0	29	36	34	25	60	15
CF00-03	17	34	29	1	*0.4*	7	1	10	100	484	21	79	0	21	42	37	19	73	8
CF96-23	16	20	14	11	*4.9*	6	2	32	100	586	31	69	0	31	40	29	28	61	11
CF00-29	16	22	24	14	*2.3*	3	0	21	100	621	26	74	0	26	35	39	25	70	4
CF96-35	12	14	10	21	*4.2*	10	1	32	100	592	38	62	0	35	38	28	29	47	24
CF96-39	12	26	15	8	*2.3*	10	1	28	100	737	23	77	0	23	48	28	21	63	17
Very Fine Sand Group (VF)																			
CF96-21	10	18	12	7	*4.2*	14	1	38	100	442	25	75	0	25	45	30	19	55	27
CF96-10	9	12	11	8	*1.8*	14	0	46	100	422	28	72	0	28	37	35	19	50	31

Q: total quartz; P: total plagioclase; K: total K-feldspar; C1: total carbonate determined by point-counting

C_2: total carbonate determined by mixing exercise; Not included in Total % calculation

B: total biotite; D: total accessory phases; misc: total miscellaneous phases (grains too small too identify)

n: total points counted; F: total feldspar (P + K)

3.3. Geochemical analyses

With the exception of two bedrock samples (CF96-04 and CF96-08), major (Table 3) and trace elements (Table 4) were analyzed at the Chemical Fingerprinting Laboratory of Laurentian University, Sudbury, Ontario using a Thermo Fisher Series II inductively coupled plasma quadruple mass spectrometer (ICP-MS). Instrument operating conditions and analytical procedures follow those from Eggins et al. (1997), with modifications outlined in Kamber et al. (2003). All major oxides and LOI have detection limits of 0.01 wt. % and 0.05 wt. %, respectively. Samples were analyzed in parts per billion for a suite of 46 trace elements (Table 4). Multiple digestions of the USGS reference material W-2 were used for instrumental calibration (Table 4). The USGS standards BHVO-1 and GSP-2b were analyzed as unknowns and compared to the long-term reproducibility reported in Kamber (2009). For USGS standard BHVO-1, the majority of the elements have a long-term (3-year) external reproducibility of better than 1 %. Activation Laboratories Ltd. measured major oxide and REE geochemistry of samples CF96-04 and CF96-08 (Tables 3, 4).

Powdered aliquots of all samples were analyzed by coulometry following procedures outlined by Huffman and Stuber (1985) to determine total carbonate-CO_2. Analytical uncertainty for analysis of total CO_2 (Table 3) had a precision of better than 1 %.

4. Compositional influence of caliche

In the study area, caliche occurs as a crust that discontinuously coats bedrock and fills open joints. Once it weathers and enters the transport system, caliche consists of up to 3 mm diameter, spherical, micrite-cemented aggregates that include silicate phases (from the sediment). Because caliche aggregates are present in all 24 sediment samples (Table 2; Appendix A1.1, p. 82), it is necessary to determine its abundance and account for its composition where it may interfere with

Table 3. Major element analysis of Stepladder samples. All major oxides in weight percent

Sample	SiO_2	TiO_2	Al_2O_3	Fe_2O_3	MnO	MgO	CaO	Na_2O	K_2O	P_2O_5	CO_2	LOI	Total	CIA
Fresh Bedrock														
ST09-02	70.71	0.33	15.38	1.93	0.03	0.57	2.09	4.76	3.63	0.11	--	0.85	100.39	50.1
CF00-18	71.84	0.31	15.09	1.68	0.03	0.61	2.27	4.66	3.45	0.10	--	0.65	100.69	49.7
CF96-4	71.39	0.25	15.32	1.75	0.03	0.48	2.01	4.24	4.19	0.10	--	0.44	100.20	50.7
CF96-8	73.69	0.22	14.75	1.45	0.03	0.49	1.92	4.40	3.37	0.08	--	0.51	100.91	51.0
Avg	71.91	0.28	15.14	1.70	0.03	0.54	2.07	4.52	3.66	0.10	--	0.61	--	50.4
Regolith														
CF00-04	71.59	0.29	14.54	1.90	0.02	0.40	1.85	4.23	4.11	0.08	0.02	0.75	99.78	50.0
CF00-05	73.69	0.23	14.48	1.41	0.02	0.36	1.82	4.24	3.94	0.09	0.12	0.57	100.97	50.7
Avg	72.64	0.26	14.51	1.66	0.02	0.38	1.84	4.24	4.03	0.09	0.07	0.66	--	50.3
Grus														
CF96-01	69.59	0.44	14.23	2.87	0.04	0.87	1.98	3.27	3.67	0.10	0.15	3.36	100.58	53.4
Gravel Group (G)														
CF96-11	74.46	0.26	12.41	1.46	0.02	0.29	1.46	3.48	3.99	0.06	0.09	0.69	98.67	50.1
CF00-10	72.63	0.31	12.26	1.81	0.04	0.71	2.31	2.98	3.58	0.08	0.59	2.25	99.55	51.5
CF96-36	72.70	0.28	13.67	1.54	0.03	0.47	2.33	3.88	3.81	0.09	0.60	1.09	100.49	50.7
CF00-09	66.83	0.47	14.63	2.93	0.05	1.09	2.85	3.85	2.99	0.13	0.38	3.52	99.70	51.7
Avg	71.66	0.33	13.24	1.94	0.04	0.64	2.24	3.55	3.59	0.09	0.42	1.89	--	51.0
Very Coarse Sand Group (VC)														
CF96-40	72.86	0.59	12.80	3.71	0.04	0.36	1.77	3.54	3.62	0.09	0.30	1.25	100.92	51.4
CF96-22	69.28	0.32	14.38	1.75	0.03	0.42	2.67	4.49	3.52	0.09	0.61	1.20	98.74	49.7
CF00-07	73.97	0.23	13.07	1.32	0.02	0.42	1.97	3.71	3.75	0.06	0.47	1.05	100.03	50.9
Avg	72.04	0.38	13.42	2.26	0.03	0.40	2.14	3.91	3.63	0.08	0.46	1.17	--	50.6
Coarse Sand Group (C)														
CF96-19	66.06	0.28	16.33	1.55	0.03	0.65	3.62	4.92	3.65	0.09	1.23	1.46	99.86	50.8
CF96-12	68.56	0.35	16.11	1.83	0.03	0.69	2.64	4.99	3.48	0.08	0.39	1.26	100.42	50.5
CF96-15	67.82	0.33	16.33	1.84	0.03	0.60	2.91	5.18	3.30	0.08	0.59	1.31	100.33	50.6
CF96-34	70.52	0.33	15.53	1.61	0.03	0.40	2.42	4.91	3.21	0.10	0.91	0.61	100.58	52.9
CF96-20	70.76	0.22	15.43	1.18	0.02	0.39	2.33	4.72	3.80	0.06	0.48	1.06	100.46	50.8
CF96-26	69.34	0.24	16.35	1.27	0.02	0.42	2.56	5.18	3.39	0.07	0.46	1.20	100.51	51.0
Avg	68.84	0.29	16.01	1.55	0.03	0.53	2.75	4.98	3.47	0.08	0.67	1.15	--	51.1
Medium Sand Group (M)														
CF00-17	65.81	0.53	16.81	2.56	0.05	0.75	3.25	5.37	3.07	0.20	0.60	1.77	100.77	50.7
CF00-06	63.27	1.18	15.43	4.80	0.08	0.81	3.44	4.95	2.78	0.48	0.42	1.74	99.38	50.1
CF96-07	61.34	0.57	15.90	3.46	0.06	1.58	4.42	4.27	2.87	0.20	1.36	3.68	99.71	51.7
Avg	63.47	0.76	16.05	3.61	0.06	1.05	3.70	4.86	2.91	0.29	0.80	2.39	--	50.8
Fine Sand Group (F)														
CF00-14	65.14	0.44	13.32	2.58	0.04	1.32	4.72	3.25	3.25	0.08	2.30	3.49	99.93	51.7
CF00-03	67.74	0.47	15.28	3.21	0.05	0.94	2.29	3.89	3.36	0.16	0.11	3.51	101.00	52.9
CF96-23	65.45	0.51	14.67	3.02	0.05	1.21	3.91	3.91	3.15	0.16	1.28	2.70	100.01	51.4
CF00-29	68.33	0.45	13.32	2.91	0.05	1.17	2.74	3.14	3.23	0.16	0.58	4.27	100.34	52.5
CF96-35	63.01	0.53	14.20	3.31	0.06	1.64	3.64	3.15	3.24	0.17	1.10	5.56	99.61	53.0
CF96-39	65.16	0.74	14.15	4.17	0.07	1.41	3.08	3.45	2.99	0.17	0.59	3.35	99.32	52.3
Avg	65.81	0.52	14.16	3.20	0.05	1.28	3.40	3.47	3.20	0.15	0.99	3.81	--	52.3
Very Fine Sand Group (VF)														
CF96-21	63.47	0.59	15.83	3.49	0.06	1.28	4.06	4.29	2.87	0.19	1.09	3.26	100.47	51.6
CF96-10	61.72	0.58	15.26	3.72	0.07	1.70	4.28	3.64	2.79	0.20	0.47	5.84	100.28	49.9
Avg	62.60	0.59	15.55	3.61	0.07	1.49	4.17	3.97	2.83	0.20	0.78	4.55	--	50.8
Caliche														
CF00-01	26.02	0.57	1.91	0.98	0.02	3.74	31.31	0.05	0.44	0.11	26.04	34.78	99.54	39.5

Table 4. Trace element analysis of Stepladder samples. All trace element abundances in ppm.

Type	CV	*Bedrock*					*Regolith*			*Grus*
Sample	W-2	ST09-02	CF00-18	CF96-4	CF96-8	*Avg*	CF00-04	CF00-05	*Avg*	CF96-01
Li	9.16	33.34	29.00	--	--	*31.17*	22.26	18.29	*20.27*	21.43
Be	0.62	2.46	2.74	--	--	*2.60*	1.88	1.92	*1.90*	2.14
Sc	36.07	0.63	0.61	--	--	*0.62*	0.85	0.41	*0.63*	3.08
Ti	6354.61	1951.03	1816.12	--	--	*1883.58*	1673.21	1407.35	*1540.28*	2788.32
V	261.60	22.94	20.53	--	--	*21.73*	18.75	15.73	*17.24*	37.43
Cr	92.79	1.75	1.26	--	--	*1.51*	1.38	1.27	*1.33*	15.63
Co	44.53	1.14	1.29	--	--	*1.21*	1.37	0.99	*1.18*	3.18
Ni	69.99	0.86	0.79	--	--	*0.82*	0.94	0.76	*0.85*	6.20
Cu	103.00	2.20	1.79	--	--	*1.99*	1.75	1.98	*1.87*	7.99
Zn	77.00	10.64	12.30	--	--	*11.47*	20.69	12.23	*16.46*	28.59
Ga	17.42	16.68	16.44	--	--	*16.56*	16.38	14.85	*15.61*	18.05
Rb	19.80	46.60	42.53	--	--	*44.56*	66.88	60.60	*63.74*	51.02
Sr	194.83	348.31	342.28	--	--	*345.30*	307.60	286.34	*296.97*	233.76
Y	20.11	6.65	5.68	--	--	*6.17*	4.67	4.38	*4.53*	12.87
Zr	87.87	151.60	188.81	--	--	*170.20*	130.13	131.38	*130.75*	253.27
Nb	7.28	7.40	7.44	--	--	*7.42*	6.19	5.14	*5.67*	11.20
Ag	0.08	0.03	0.04	--	--	*0.03*	0.03	0.04	*0.03*	0.12
Cd	0.08	0.06	0.07	--	--	*0.06*	0.05	0.05	*0.05*	0.12
In	0.06	0.02	0.03	--	--	*0.02*	0.02	0.02	*0.02*	0.03
Sn	1.95	1.16	1.16	--	--	*1.16*	1.38	1.12	*1.25*	1.47
Sb	0.71	0.05	0.02	--	--	*0.04*	0.04	0.02	*0.03*	0.27
Cs	0.89	1.04	0.90	--	--	*0.97*	0.66	0.65	*0.65*	1.55
Ba	169.68	872.11	615.92	--	--	*744.02*	797.73	712.47	*755.10*	650.85
La	10.52	32.13	18.25	19.60	17.00	*21.74*	20.85	19.94	*20.39*	39.35
Ce	23.22	42.92	20.02	36.80	31.70	*32.86*	35.77	29.51	*32.64*	72.14
Pr	3.03	7.16	3.96	4.10	3.50	*4.68*	4.54	4.25	*4.39*	9.63
Nd	12.91	24.68	13.92	14.70	12.50	*16.45*	15.62	14.59	*15.10*	35.08
Sm	3.27	3.68	2.36	2.42	2.06	*2.63*	2.47	2.24	*2.36*	6.31
Eu	1.09	0.77	0.61	0.75	0.68	*0.70*	0.63	0.66	*0.64*	0.81
Gd	3.71	2.33	1.66	1.47	1.34	*1.70*	1.60	1.44	*1.52*	4.40
Tb	0.62	0.28	0.22	0.20	0.19	*0.22*	0.20	0.18	*0.19*	0.54
Dy	3.81	1.37	1.10	0.94	0.86	*1.07*	1.00	0.89	*0.94*	2.70
Ho	0.80	0.25	0.21	0.16	0.15	*0.19*	0.18	0.17	*0.17*	0.50
Er	2.22	0.64	0.56	0.42	0.38	*0.50*	0.45	0.43	*0.44*	1.31
Tm	0.33	0.09	0.08	0.06	0.05	*0.07*	0.07	0.06	*0.06*	0.20
Yb	2.06	0.57	0.56	0.37	0.32	*0.46*	0.41	0.40	*0.40*	1.25
Lu	0.30	0.09	0.09	0.06	0.05	*0.07*	0.06	0.06	*0.06*	0.19
Hf	2.36	4.06	5.38	--	--	*4.72*	3.59	3.71	*3.65*	6.84
Ta	0.45	0.45	0.50	--	--	*0.47*	0.43	0.33	*0.38*	0.77
W	0.24	1.95	0.07	--	--	*1.01*	0.07	0.05	*0.06*	0.54
Tl	0.09	0.43	0.43	--	--	*0.43*	0.42	0.42	*0.42*	0.43
Pb	7.53	10.00	10.67	--	--	*10.33*	14.58	12.85	*13.71*	11.68
Th	2.10	9.33	3.89	--	--	*6.61*	6.36	5.11	*5.74*	19.66
U	0.51	0.32	0.26	--	--	*0.29*	0.41	0.36	*0.39*	1.25

Table 4 ***(cont.)***

Type	*Gravel Group (G)*					*Very Coarse Sand Group (VC)*				*(C)*
Sample	CF96-11	CF00-10	CF96-36	CF00-09	*Avg*	CF96-40	CF96-22	CF00-07	*Avg*	CF96-19
Li	13.31	20.83	15.37	25.76	*20.65*	11.55	14.70	14.82	*13.69*	21.32
Be	1.85	1.74	2.39	2.34	*2.16*	2.16	2.82	1.92	*2.30*	3.13
Sc	0.79	2.10	1.37	3.43	*2.30*	1.45	1.16	0.68	*1.10*	1.97
Ti	1549.65	1789.26	1645.64	2943.91	*2126.27*	3420.57	1822.63	1369.60	*2204.27*	1650.28
V	17.54	22.77	18.02	36.95	*25.91*	49.17	21.30	16.12	*28.86*	16.94
Cr	2.07	4.82	6.96	14.92	*8.90*	8.66	5.71	4.04	*6.14*	6.47
Co	1.06	1.78	1.74	3.63	*2.39*	2.07	1.67	1.12	*1.62*	2.31
Ni	1.26	2.24	2.95	5.40	*3.53*	3.06	2.76	1.73	*2.51*	3.94
Cu	1.35	2.53	3.95	5.60	*4.03*	4.99	3.45	4.72	*4.38*	3.62
Zn	11.61	28.33	16.37	42.85	*29.18*	15.52	15.13	13.00	*14.55*	27.83
Ga	15.24	15.03	16.56	18.16	*16.58*	16.38	18.11	14.82	*16.44*	21.59
Rb	68.36	71.37	53.84	52.37	*59.19*	49.40	47.48	60.04	*52.31*	63.94
Sr	213.51	296.16	239.34	324.15	*286.55*	180.55	244.23	285.25	*236.68*	354.45
Y	4.31	5.38	7.49	11.59	*8.15*	13.11	7.20	4.10	*8.14*	6.63
Zr	132.25	158.37	196.00	259.01	*204.46*	298.54	172.96	123.10	*198.20*	125.82
Nb	6.93	6.59	7.60	11.33	*8.51*	15.05	8.00	5.64	*9.56*	8.06
Ag	0.06	0.03	0.09	0.08	*0.07*	0.12	0.10	0.06	*0.09*	0.08
Cd	0.05	0.06	0.10	0.13	*0.10*	0.14	0.10	0.05	*0.10*	0.08
In	0.01	0.02	0.02	0.04	*0.03*	0.02	0.03	0.02	*0.02*	0.02
Sn	1.15	1.34	1.05	1.87	*1.42*	1.43	1.02	0.91	*1.12*	1.10
Sb	0.09	0.05	0.20	0.16	*0.14*	0.26	0.18	0.07	*0.17*	0.16
Cs	0.65	1.00	0.97	1.62	*1.20*	0.79	0.94	0.65	*0.79*	1.31
Ba	786.64	687.38	858.60	520.08	*688.69*	702.05	593.60	684.23	*659.96*	647.15
La	15.13	20.12	18.17	26.19	*21.49*	38.26	21.63	18.93	*26.27*	14.36
Ce	25.95	38.74	29.25	50.85	*39.61*	62.14	28.66	33.81	*41.54*	25.68
Pr	3.31	4.49	4.10	6.14	*4.91*	8.19	4.77	4.27	*5.75*	3.28
Nd	11.72	15.79	14.55	22.03	*17.46*	28.18	16.38	14.90	*19.82*	11.91
Sm	1.86	2.63	2.49	3.90	*3.01*	4.42	2.65	2.38	*3.15*	2.14
Eu	0.40	0.57	0.57	0.83	*0.66*	0.48	0.53	0.53	*0.51*	0.64
Gd	1.26	1.78	1.87	2.98	*2.21*	3.11	1.84	1.50	*2.15*	1.63
Tb	0.16	0.23	0.26	0.41	*0.30*	0.42	0.25	0.18	*0.28*	0.23
Dy	0.84	1.12	1.41	2.24	*1.59*	2.32	1.34	0.86	*1.51*	1.24
Ho	0.15	0.21	0.28	0.45	*0.31*	0.47	0.26	0.16	*0.30*	0.24
Er	0.41	0.54	0.77	1.23	*0.85*	1.30	0.74	0.40	*0.81*	0.66
Tm	0.06	0.08	0.12	0.19	*0.13*	0.20	0.12	0.06	*0.13*	0.10
Yb	0.41	0.50	0.78	1.21	*0.83*	1.30	0.81	0.37	*0.83*	0.64
Lu	0.06	0.08	0.12	0.19	*0.13*	0.20	0.13	0.06	*0.13*	0.10
Hf	3.75	4.45	5.25	6.76	*5.49*	8.09	4.72	3.44	*5.41*	3.36
Ta	0.48	0.36	0.55	0.68	*0.53*	1.22	0.60	0.38	*0.73*	0.52
W	0.31	0.15	1.07	0.43	*0.55*	1.34	2.55	0.17	*1.35*	1.04
Tl	0.46	0.42	0.45	0.39	*0.42*	0.41	0.43	0.41	*0.42*	0.51
Pb	10.53	13.04	11.98	13.80	*12.94*	9.79	10.98	11.88	*10.88*	15.37
Th	5.55	7.91	5.72	8.96	*7.53*	16.32	6.58	6.22	*9.71*	4.89
U	0.62	0.59	0.67	1.03	*0.76*	1.45	0.70	0.48	*0.87*	1.04

Table 4 *(cont.)*

Type	*Coarse Sand Group (C)*						*Medium Sand Group (M)*			
Sample	CF96-12	CF96-15	CF96-34	CF96-20	CF96-26	*Avg*	CF00-17	CF00-06	CF96-07	*Avg*
Li	23.69	10.42	18.51	19.46	17.12	*18.42*	23.30	25.23	30.82	*26.45*
Be	2.82	2.86	3.01	2.83	3.17	*2.97*	3.57	3.10	2.80	*3.16*
Sc	1.06	1.55	0.98	1.12	1.30	*1.33*	1.16	2.17	3.95	*2.42*
Ti	2025.99	1879.39	1899.97	1313.87	1473.44	*1707.16*	3099.82	6949.05	3517.56	*4522.14*
V	19.08	9.90	17.93	12.12	14.36	*15.06*	31.81	66.79	43.11	*47.24*
Cr	11.37	3.75	4.38	1.86	5.27	*5.52*	9.26	16.00	34.14	*19.80*
Co	2.56	1.73	1.81	1.79	2.06	*2.05*	1.70	3.18	5.86	*3.58*
Ni	6.59	3.33	2.25	1.74	3.04	*3.48*	2.88	5.31	16.05	*8.08*
Cu	2.26	2.63	3.70	4.35	3.20	*3.29*	5.14	2.66	8.56	*5.45*
Zn	30.08	23.34	24.65	25.15	24.82	*25.98*	17.86	28.22	55.45	*33.84*
Ga	20.04	19.13	19.54	19.48	20.36	*20.02*	19.48	20.83	21.12	*20.48*
Rb	38.72	40.63	49.68	73.93	60.28	*54.53*	33.96	23.58	23.76	*27.10*
Sr	236.69	325.92	165.96	213.42	231.48	*254.65*	389.38	419.56	256.30	*355.08*
Y	4.79	5.16	4.45	2.98	4.27	*4.71*	14.82	22.08	15.56	*17.49*
Zr	125.41	51.09	158.18	117.84	135.94	*119.05*	214.52	468.68	274.57	*319.26*
Nb	8.95	9.50	9.57	6.91	7.02	*8.34*	14.33	28.39	14.21	*18.98*
Ag	0.06	0.06	0.10	0.09	0.09	*0.08*	0.10	0.07	0.12	*0.09*
Cd	0.06	0.05	0.08	0.06	0.09	*0.07*	0.14	0.18	0.15	*0.15*
In	0.03	0.02	0.02	0.02	0.02	*0.02*	0.03	0.04	0.05	*0.04*
Sn	1.42	1.34	1.36	0.97	0.99	*1.20*	1.99	1.36	1.28	*1.54*
Sb	0.14	0.28	0.23	0.16	0.22	*0.20*	0.23	0.19	0.27	*0.23*
Cs	0.94	1.09	0.92	1.05	0.98	*1.05*	1.35	0.97	1.63	*1.32*
Ba	551.49	497.20	493.05	605.73	589.37	*564.00*	453.40	472.34	490.20	*471.98*
La	12.48	17.88	14.16	11.26	7.97	*13.02*	33.41	68.64	37.77	*46.60*
Ce	25.09	34.76	31.81	24.56	19.41	*26.89*	54.66	112.56	61.62	*76.28*
Pr	3.02	4.04	2.95	2.56	1.86	*2.95*	7.80	15.59	8.90	*10.76*
Nd	10.88	14.37	10.04	9.30	6.82	*10.55*	28.20	56.23	32.17	*38.87*
Sm	1.93	2.38	1.59	1.53	1.24	*1.80*	4.99	9.66	5.64	*6.76*
Eu	0.47	0.60	0.26	0.29	0.33	*0.43*	0.92	1.27	1.09	*1.10*
Gd	1.42	1.65	1.09	1.01	0.99	*1.30*	3.75	6.84	4.21	*4.93*
Tb	0.19	0.21	0.15	0.12	0.14	*0.17*	0.51	0.88	0.57	*0.65*
Dy	0.96	1.07	0.77	0.59	0.76	*0.90*	2.78	4.47	3.04	*3.43*
Ho	0.18	0.20	0.15	0.11	0.15	*0.17*	0.55	0.83	0.59	*0.66*
Er	0.46	0.50	0.42	0.29	0.42	*0.46*	1.51	2.14	1.58	*1.74*
Tm	0.07	0.07	0.07	0.04	0.07	*0.07*	0.23	0.31	0.23	*0.26*
Yb	0.43	0.45	0.44	0.29	0.44	*0.45*	1.46	1.95	1.50	*1.64*
Lu	0.06	0.06	0.07	0.05	0.07	*0.07*	0.22	0.28	0.22	*0.24*
Hf	3.50	1.64	4.43	3.29	3.70	*3.32*	6.01	13.26	7.19	*8.82*
Ta	0.55	0.79	0.75	0.52	0.51	*0.61*	1.07	2.29	0.88	*1.41*
W	0.33	0.74	1.22	1.11	1.12	*0.93*	1.64	0.61	0.63	*0.96*
Tl	0.43	0.31	0.42	0.52	0.45	*0.44*	0.44	0.36	0.36	*0.38*
Pb	10.46	11.90	12.21	14.24	15.47	*13.28*	16.33	15.04	14.67	*15.35*
Th	4.19	7.02	5.19	7.24	3.26	*5.30*	13.90	28.02	10.47	*17.47*
U	0.57	0.71	1.04	0.94	1.05	*0.89*	0.59	1.92	1.08	*1.20*

Table 4 ***(cont.)***

Type	*Fine Sand Group (F)*							*Very Fine Sand Group (VF)*		
Sample	CF00-14	CF00-03	CF96-23	CF00-29	CF96-35	CF96-39	*Avg*	CF96-21	CF96-10	*Avg*
Li	26.59	26.72	23.59	24.01	28.92	21.27	*25.18*	26.14	30.93	*28.53*
Be	2.18	2.41	2.82	2.31	2.53	2.51	*2.46*	3.09	2.72	*2.90*
Sc	4.28	3.93	4.10	2.89	4.25	4.42	*3.98*	3.66	6.34	*5.00*
Ti	2557.59	2727.01	3009.92	2779.78	3089.85	4271.41	*3072.59*	3330.32	3365.42	*3347.87*
V	37.69	38.43	40.23	40.61	44.76	58.25	*43.33*	44.74	48.58	*46.66*
Cr	21.49	17.46	20.79	20.70	27.55	33.51	*23.58*	23.12	32.13	*27.62*
Co	3.38	4.32	4.67	3.03	5.87	5.23	*4.42*	4.87	6.95	*5.91*
Ni	7.40	6.59	8.99	6.87	12.35	11.18	*8.90*	9.20	14.80	*12.00*
Cu	7.70	9.63	8.47	10.71	15.82	12.10	*10.74*	9.11	15.30	*12.21*
Zn	31.86	47.30	45.06	34.99	53.99	40.70	*42.32*	45.96	67.74	*56.85*
Ga	16.13	18.64	19.25	16.40	18.03	17.56	*17.67*	20.33	21.28	*20.80*
Rb	64.64	59.18	46.71	62.97	23.52	17.95	*45.83*	17.78	63.85	*40.81*
Sr	354.79	349.42	273.52	312.51	177.49	176.75	*274.08*	226.36	298.05	*262.20*
Y	13.73	15.25	18.71	15.56	19.44	25.04	*17.96*	21.40	21.43	*21.41*
Zr	248.92	272.17	325.03	250.02	262.81	572.18	*321.86*	342.63	354.28	*348.45*
Nb	10.82	10.40	12.55	11.83	12.73	17.07	*12.57*	15.07	13.62	*14.35*
Ag	0.13	0.08	0.15	0.11	0.16	0.20	*0.14*	0.15	0.16	*0.16*
Cd	0.13	0.14	0.19	0.15	0.19	0.28	*0.18*	0.20	0.21	*0.20*
In	0.03	0.04	0.04	0.04	0.05	0.05	*0.04*	0.05	0.05	*0.05*
Sn	1.49	1.74	1.18	1.53	1.29	1.13	*1.39*	0.97	0.86	*0.91*
Sb	0.29	0.22	0.32	0.27	0.49	0.44	*0.34*	0.37	0.36	*0.37*
Cs	2.12	2.03	1.99	2.26	2.57	1.92	*2.15*	1.73	2.58	*2.15*
Ba	700.55	736.83	562.62	814.26	605.37	567.42	*664.51*	517.27	587.45	*552.36*
La	25.74	50.11	28.95	35.96	27.15	41.87	*34.96*	41.57	46.93	*44.25*
Ce	46.56	91.13	46.67	64.67	39.74	61.93	*58.45*	69.93	78.96	*74.44*
Pr	6.16	11.48	6.89	8.31	6.60	10.03	*8.24*	9.93	10.93	*10.43*
Nd	22.32	40.79	25.34	29.68	24.58	36.79	*29.92*	36.45	39.21	*37.83*
Sm	4.06	6.76	4.63	5.13	4.67	6.75	*5.33*	6.65	6.80	*6.72*
Eu	0.87	1.08	0.96	0.92	0.99	1.14	*0.99*	1.06	1.23	*1.14*
Gd	3.22	4.74	3.82	3.93	4.00	5.50	*4.20*	5.29	5.27	*5.28*
Tb	0.46	0.61	0.57	0.55	0.60	0.80	*0.60*	0.75	0.74	*0.74*
Dy	2.60	3.11	3.32	3.02	3.49	4.53	*3.35*	4.06	4.10	*4.08*
Ho	0.53	0.60	0.69	0.60	0.72	0.94	*0.68*	0.80	0.81	*0.80*
Er	1.45	1.59	1.97	1.63	2.04	2.64	*1.89*	2.20	2.21	*2.20*
Tm	0.22	0.24	0.31	0.24	0.31	0.41	*0.29*	0.33	0.34	*0.33*
Yb	1.47	1.53	2.08	1.56	2.04	2.73	*1.90*	2.18	2.17	*2.17*
Lu	0.22	0.23	0.32	0.23	0.31	0.42	*0.29*	0.33	0.33	*0.33*
Hf	6.50	7.14	8.41	6.50	6.82	14.31	*8.28*	8.94	9.17	*9.05*
Ta	0.74	0.68	0.83	0.87	0.82	1.18	*0.86*	1.05	0.83	*0.94*
W	0.94	0.49	2.74	0.74	1.32	1.43	*1.27*	1.75	0.88	*1.31*
Tl	0.47	0.43	0.45	0.47	0.41	0.35	*0.43*	0.46	0.46	*0.46*
Pb	12.45	17.12	14.84	13.40	13.11	11.84	*13.79*	14.18	19.71	*16.95*
Th	8.20	16.62	9.34	11.12	11.27	17.56	*12.35*	14.79	14.29	*14.54*
U	2.02	1.37	1.47	1.05	1.37	1.68	*1.49*	1.50	1.79	*1.64*

interpreting the sediment geochemistry. The amount of caliche in each sediment sample was first estimated via point counting (Table 2), although a clear connection between modal mineralogy and weight percent CO_2 (as a proxy for calcite) did not always correlate because of grain-size effects in point counting.

A more accurate evaluation of caliche abundance was determined using iterative compositional mixing of the bulk bedrock and caliche geochemistry. The composition of fresh average bedrock, which had no measurable CO_2, was mixed with caliche in 0.02 % increments from 0.02 to 10 %. Because chemical weathering is so limited in the sediments samples, bedrock is a close approximation for the bulk major-element geochemistry of the sediments. Mixture results of wt. % CO_2 were compared to the measured values in sediment samples and the percent caliche was matched with the percent mixed value (average of all samples = 2.3 %, minimum = 0.04 %, maximum = 8.8 %).

Three modeled compositions of Stepladder granodiorite mixed with 2 %, 5 %, and 9 % caliche were normalized to average bedrock (Fig. 2A, B). For an average of about 2 % caliche addition as discussed above, there is less than a maximum factor of 1.3 changes in composition relative to bedrock for all effected elements of interest (MgO, CaO, Sc, Cr, Co, Ni), which corresponds to concentration changes of less than 1 ppm for most trace elements in the studied samples. At 9 % caliche addition (1 sample), concentration changes by less than 2 ppm for the selected trace elements. The rare earth element (REE) pattern for caliche is very similar to average bedrock (Fig. 2C), and so has no effect on either bedrock or sediment composition, or on interpreting provenance with REE.

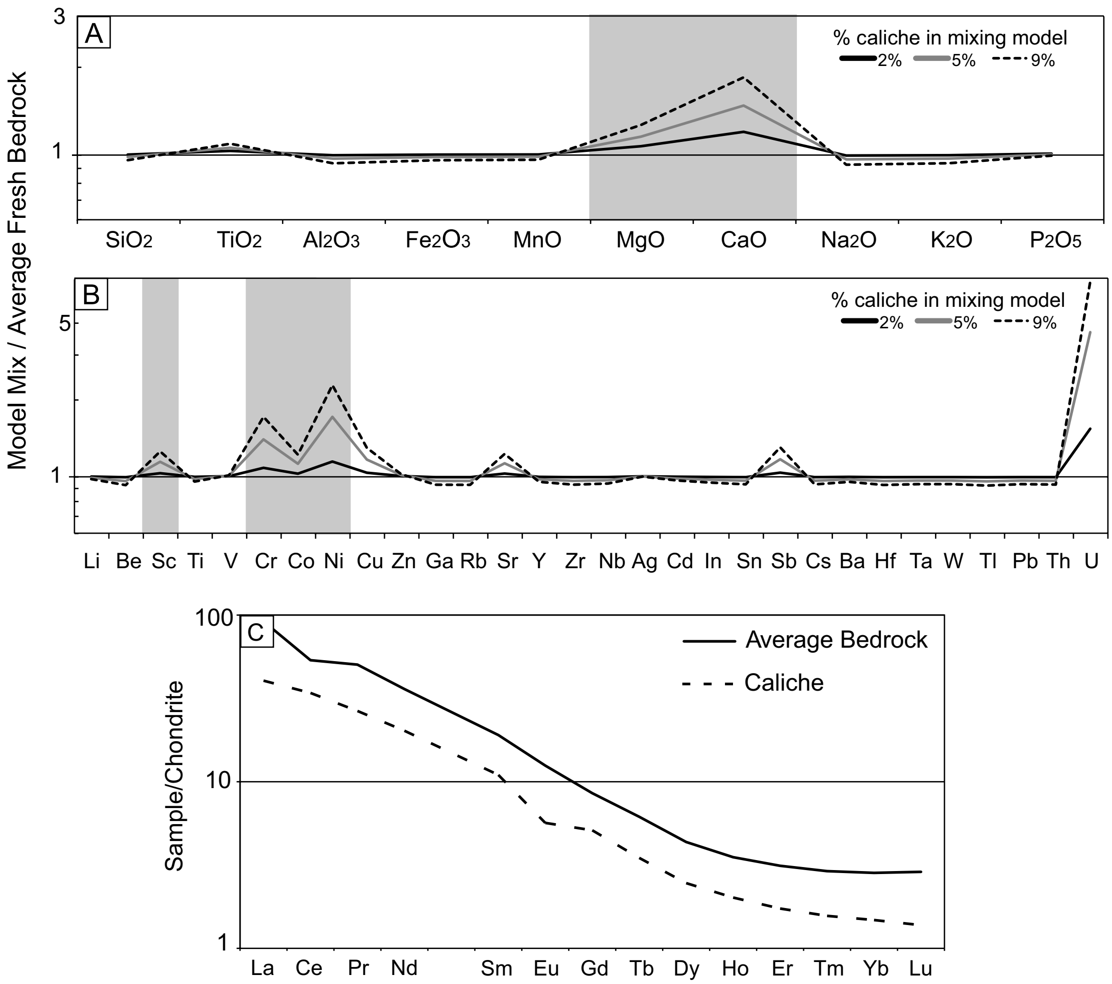

Figure 2. Plots showing the influence of caliche on bedrock composition. Mixing models represent change in bedrock composition with 2 %, 5 %, and 9 % caliche addition for (A) major elements and (B) trace elements. Gray boxes highlight the elements of interest that caliche is enriched in. (C) Chondrite normalized REE plot of average bedrock and caliche; chondrite composition from McDonough and Sun (1995). Note the similarities in shapes of REE patterns.

5. Characterization of the source rock: Stepladder granodiorite

5.1. Petrology

A critical understanding of the Stepladder bedrock is needed to determine the starting reference composition (which, from this point on, is referred to as 'average bedrock') for comparison purposes. The Stepladder pluton (Fig. 3A) is a coarse-grained, hypidiomorphic biotite granodiorite (Fig. 3B) with minor leucocratic phases and rare andesitic to basaltic xenoliths. From the samples examined, the pluton is compositionally and texturally homogeneous with only minor variations in biotite abundance (Table 2). In Quartz – Alkali feldspar – Plagioclase (QAP) space, the four bedrock samples are classified as granodiorite that plot near the granite boundary (Appendix A1.2, Fig. A1.4). Modal composition of average bedrock includes zoned plagioclase (dominated by oligoclase; 42 %), quartz (28 %), K-feldspar (25 %), and biotite (5 %)(Fig. 3C, D). Accessory minerals include apatite (up to 0.7 %; Fig. 3C), titanite, zircon, opaques (magnetite, ilmenite, and rutile), and allanite.

Euhedral to subhedral plagioclase megacrysts, 1 to 4 cm in length, dominate the rock. The majority of plagioclase is fresh and commonly shows albite twinning or oscillatory zoning. Select megacrysts exhibit both albite twinning and oscillatory zoning (Fig. 3D), while fewer grains show complex combinations of albite–Carlsbad twinning. Locally, plagioclase is altered along twins, oscillatory zones, and cores to secondary clays (Fig. 3D) and, in select grains, is replaced by microcrystalline aggregates of secondary micas (Appendix A1.2, Fig.A1.7). Although plagioclase-quartz grain boundaries are sharp, straight, and clear (Fig. 3D), symplectic contacts occur where plagioclase touches K-feldspar. Nearly all K-feldspar megacrysts are

Figure 3. Photographs and geochemical plots of fresh Stepladder bedrock. (A) Field photograph of bedrock exposure along the central ridge of the pluton. (B) Photograph of fresh granodiorite. Note the lack of fractures and secondary Fe-oxides. (C) Photomicrograph (crossed polarized light) of biotite and euhedral apatite poikilitically included in perthitic megacryst. (D) Photomicrograph (crossed polarized light) of sharp contact between quartz and plagioclase. Note other plagioclase contacts are intergrown and irregular. Clays preferentially replace plagioclase along albite twins and oscillatory zones (solid black arrows). Abbreviations in (B, C and D): Ap, apatite; Bt, biotite; Ksp, K-feldspar; Pl, plagioclase; Q, quartz. (E) Chondrite-normalized REE plot; chondrite composition from McDonough and Sun (1995). Gray boxes highlight Ce and Eu anomalies. (F) Upper continental crust-normalized spider plot of average and fresh Stepladder granodiorite; UCC composition from McLennan (2001). Note the similar patterns of the bedrock samples in both charts (E) and (F).

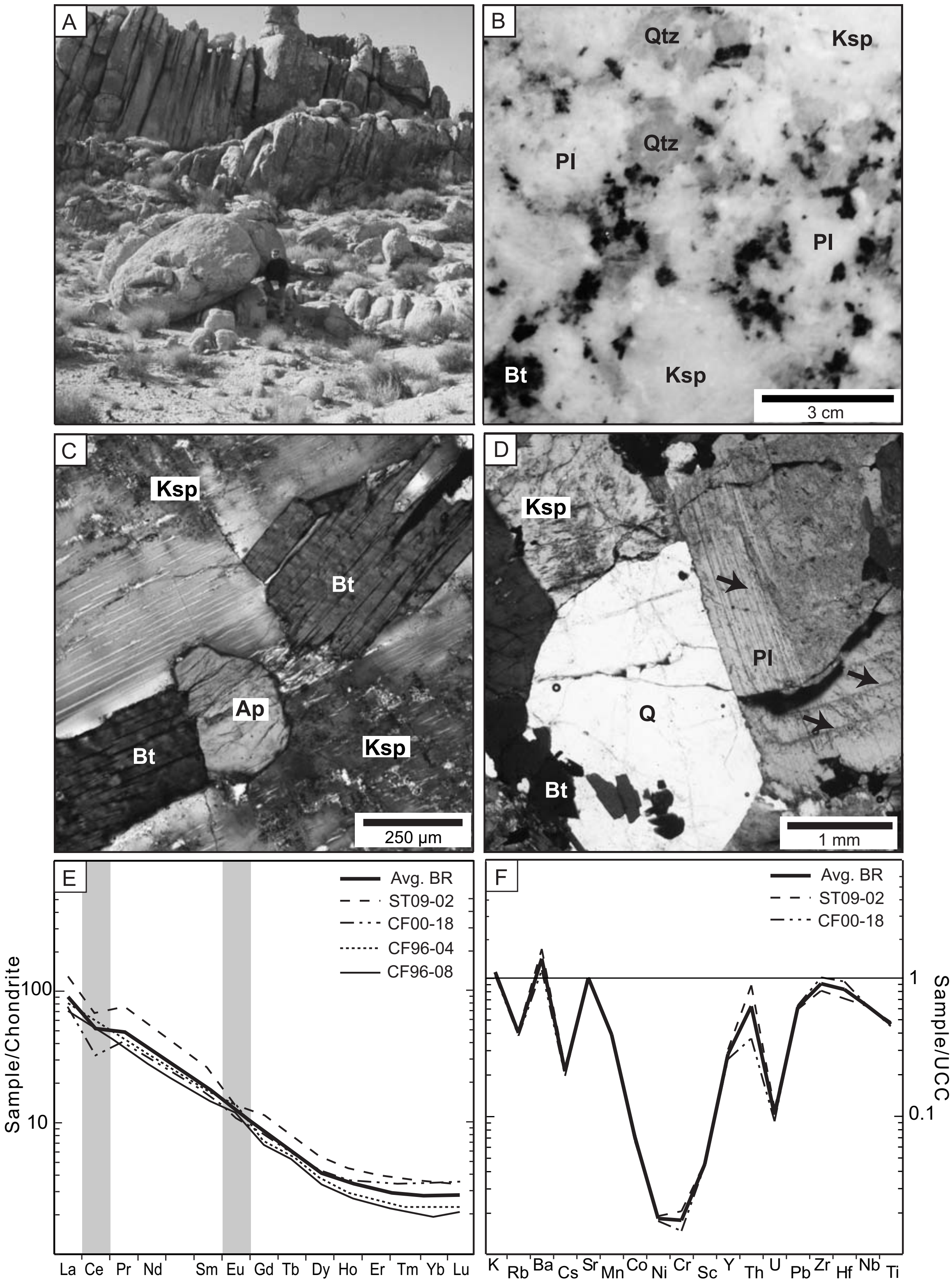
A
B
Qtz
Ksp
Pl
Qtz
Pl
Bt
Ksp
3 cm
C
Ksp
Bt
Ap
Bt
Ksp
250 µm
D
Ksp
Pl
Q
Bt
1 mm
E
Avg. BR
ST09-02
CF00-18
CF96-04
CF96-08
Sample/Chondrite
100
10
La Ce Pr Nd Sm Eu Gd Tb Dy Ho Er Tm Yb Lu
F
Avg. BR
ST09-02
CF00-18
Sample/UCC
1
0.1
K Rb Ba Cs Sr Mn Co Ni Cr Sc Y Th U Pb Zr Hf Nb Ti

perthitic (Fig. 3C) and poikilitically include euhedral accessory phases, lath-shaped plagioclase, and elongate biotite (Fig. 3C, D). Most quartz grains occur as interstitial crystals (Fig. 3B) with undulatory extinction, but can be subhedral and up to 2 cm in size. Biotite, the dominant mafic phase within the Stepladder pluton, is interstitial to or partially included by anhedral megacrysts of K-feldspar and plagioclase (Fig. 3C, D) and is associated with apatite, zircon, and opaque minerals. Chlorite partially replaces select biotite grains, creating a washed-out green color that extends along grain margins and cleavage planes (Appendix A1.2, Fig. A1.9). Additional secondary minerals include muscovite, Fe- and Ti-oxides, sericite, and lesser amounts of rutile, hematite, and calcite (Appendix A1.2, Fig. A1.5-10).

5.2. Geochemistry

5.2.1. Major elements

The Stepladder pluton is a calc-alkaline, metaluminous to weakly peraluminous granodiorite, with A/CNK values ranging from 0.97-1.03 (Appendix A2, Table A2.1). The SiO_2 contents (Table 3) of the individual bedrock samples range from 70.7 to 73.7 wt. % and have an average of 71.9 wt. %. The other major oxide abundances of the four bedrock samples differ by less than 1 wt. %, suggesting that the average fresh bedrock composition is representative of the pluton. The Stepladder pluton is similar in major element composition to other nearby Cretaceous granitoids, including the granodioritic ‘main unit’ of the East Piute pluton (Karlstrom et al., 1993), the weakly peraluminous granodiorites of the Old Woman and Sweetwater Wash plutons (Miller et al., 1990), and the biotite granodiorites of the Chemehuevi Mountains and Whipple Wash suites (John and Wooden, 1990; Anderson and Cullers, 1990).

In Al_2O_3–CaO^*+Na_2O–K_2O (A–CN–K) composition space (Fig. 4), bedrock samples plot along the feldspar join at an average CN:K ratio of 6:1 (Fig. 4B) and have an average *chemical* *index of alteration* (CIA; Nesbitt and Young, 1982) of 50.4 (Table 3). Such low CIA values indicate that the exposed Stepladder bedrock has experienced minimal chemical weathering (e.g., Nesbitt and Young, 1996). In Al_2O_3–CaO*+Na_2O+K_2O–FeO+MgO (A–CNK–FM) compositional space (Fig. 5), average bedrock plots along the feldspar – FM tie line close to the A–CNK join (Fig. 5B). In both major element plots (Figs. 4, 5), fresh bedrock plots in a position that indicates it has not been chemically weathered.

5.2.2. Rare earth and trace elements

Rare earth and trace element abundances and ratios of individual bedrock samples, as well as calculated average fresh bedrock are given in Tables 4, 5, and 6. Chondrite-normalized REE abundances (Table 5) of the four analyzed bedrocks generate similar, sub-parallel patterns (Fig. 3E). Average fresh bedrock is enriched in light REE (LREE), with $La_{CN}/Yb_{CN} = 32.3$. Light REE in average bedrock are slightly more fractionated ($La_{CN}/Sm_{CN} = 4.80$) than the heavy REE (HREE; $Gd_{CN}/Yb_{CN} = 3.01$).

REE anomalies are calculated as REE_{CN}/REE^{*}_{CN} (Table 5), where REE^{*}_{CN} is the expected chondrite-normalized concentration (of a particular REE) when interpolated from near neighbor concentrations. Where $_{CN}$ is replaced with $_{BR}$, elements are normalized to average fresh Stepladder bedrock composition (Table 6). Values >1 indicate a positive anomaly, while values <1 indicate a negative anomaly. Cerium anomalies were calculated from the nearest non-anomalous REE Pr_{CN} and Nd_{CN} due to the possible fractionation of La_{CN}. Thus, Ce* calculations assume that the difference in concentration between near neighbor pairs is constant (Lawrence

Figure 4. A–CN–K plots showing weathering trend of average fresh bedrock and Stepladder samples. (A) All Stepladder samples plot along the feldspar tie line; low CIA values indicate lack of chemical weathering associated with production of weathered bedrock and sediment. Average compositions of major minerals and rocks plotted for reference; CIA scale (Nesbitt and Young, 1982) to left of ternary diagram quantifies degree of alteration (50 = fresh bedrock - 100 = fully altered to clay); solid arrow represents predicted weathering trend of granodiorite; dashed line shows path of Toorongo granodiorite (Nesbitt and Markovics, 1997) weathering trend; box shows location of (B-E). Abbreviations in (A): Cpx, clinopyroxene; Hbl, hornblende; Pl, plagioclase; Ksp, K-feldspar; Bi, biotite; Ch, chlorite; Sm, smectite; Mu, muscovite; Il, illite; Ka, kaolinite; and G, gibbsite; A=Al_2O_3, CN=CaO*+Na_2O, and K=K_2O (molar proportions of silicate fractions only). Modified from Nesbitt and Young (1984, 1989). (B) Detail of fresh and weathered bedrock samples; average fresh bedrock and regolith has CIA values of ~50, grus is slightly more weathered with a CIA value of 53. Details of sediments grouped: (C) as a whole; (D) by geomorphic zone; and (E) by grain size.

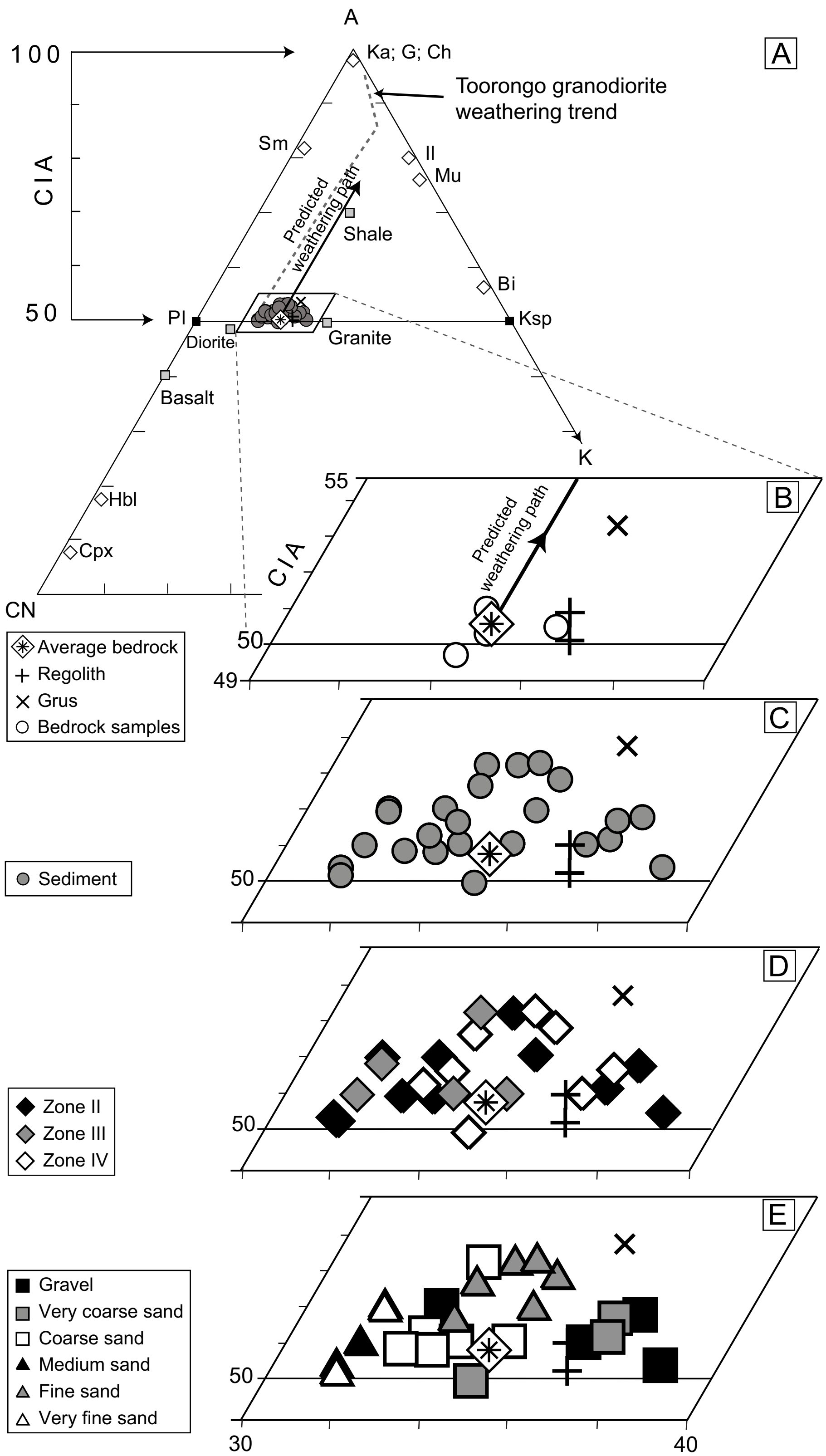
A
100
50
CIA
Ka; G; Ch
Toorongo granodiorite
weathering trend
Sm
Il
Mu
Predicted
weathering path
Shale
Bi
Pl
Ksp
Diorite
Granite
Basalt
K
Hbl
Cpx
CN
Average bedrock
Regolith
Grus
Bedrock samples
B
55
50
49
C
Sediment
D
Zone II
Zone III
Zone IV
E
Gravel
Very coarse sand
Coarse sand
Medium sand
Fine sand
Very fine sand
30
40

Figure 5. A–CNK–FM plots showing weathering trend of average fresh bedrock and Stepladder samples. (A) Sediment grouped as a whole. Average compositions of major minerals and rocks plotted for reference; solid arrow represents predicted weathering trend of fresh Stepladder granodiorite; dashed line shows path of Toorongo granodiorite (Nesbitt and Markovics, 1997) weathering trend; small triangle shows location of (B-D). Abbreviations in (A): Cpx, clinopyroxene; Hbl, hornblende; Pl, plagioclase; Ksp, K-feldspar; Bi, biotite; Ch, chlorite; Sm, smectite; Mu, muscovite; Il, illite; Ka, kaolinite; and G, gibbsite; A=Al_2O_3, CNK=CaO^*+Na_2O+K_2O, and FM=Fe_2O_3+MgO (molar proportions of silicate fractions only). (B) Detail of fresh and weathered bedrock samples. Details of sediments grouped: (C) by geomorphic zone; and (D) by grain size. Solid arrows (C) and (D) indicate fining of sediments through sorting. Modified from Nesbitt and Young (1984, 1989).

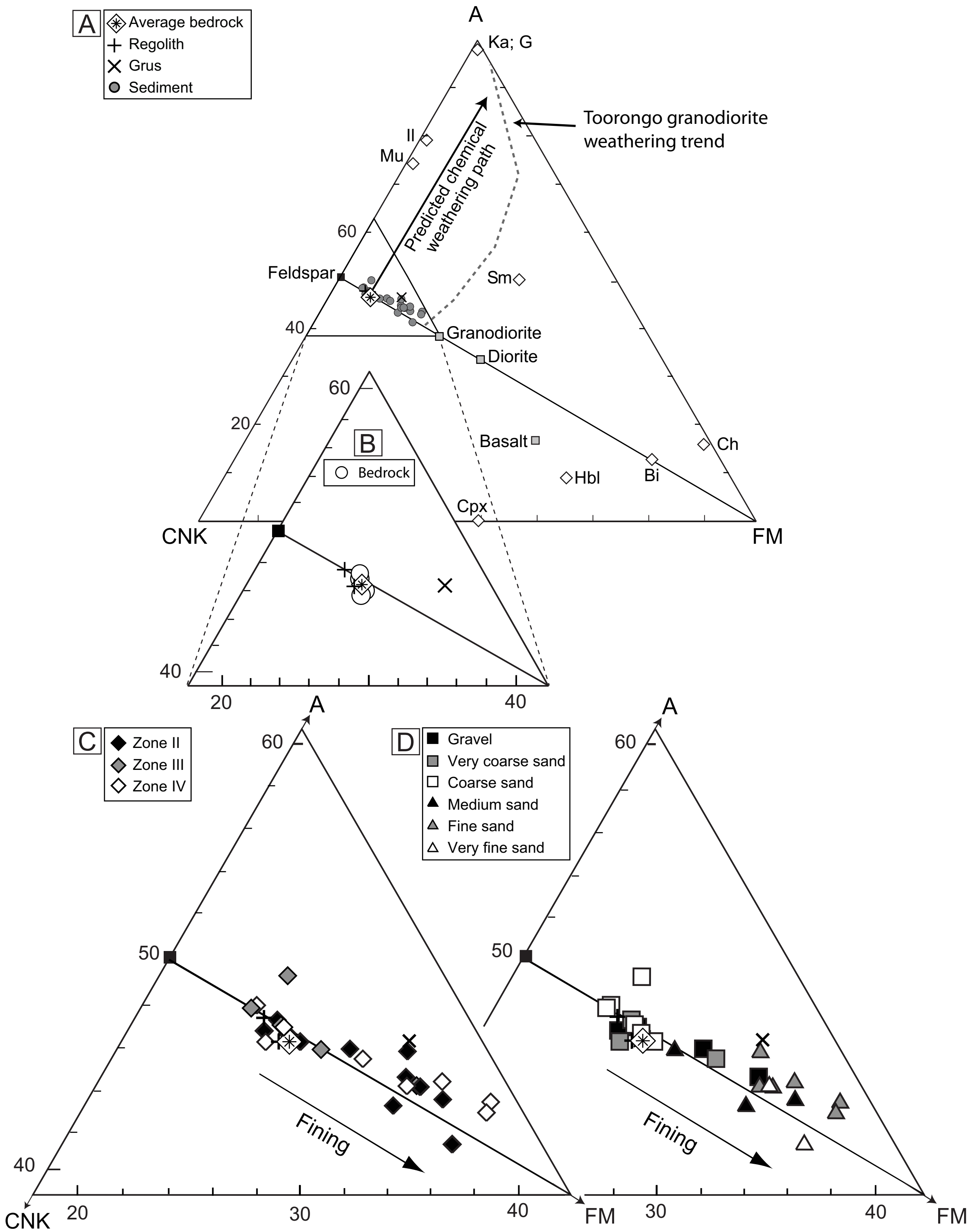
A
Average bedrock
Regolith
Grus
Sediment
A
Ka; G
Toorongo granodiorite weathering trend
Il
Mu
Predicted chemical weathering path
60
Feldspar
Sm
40
Granodiorite
Diorite
20
B
Bedrock
Basalt
Ch
Hbl
Bi
Cpx
CNK
FM
60
40
20
40
C
Zone II
Zone III
Zone IV
A
60
50
Fining
40
CNK
20
30
40
FM
D
Gravel
Very coarse sand
Coarse sand
Medium sand
Fine sand
Very fine sand
A
60
50
Fining
30
40
FM

Table 5. Chondrite-normalized REE ratios of Stepladder samples.

Sample	Ce_{CN}/Sm_{CN}	La_{CN}/Yb_{CN}	Gd_{CN}/Yb_{CN}	La_{CN}/Sm_{CN}	Eu/Eu^*_{CN}	Ce/Ce^*_{CN}
Fresh Bedrock						
ST09-02	2.63	38.00	3.28	5.08	0.78	0.70
CF00-18	1.91	22.00	2.38	4.50	0.91	0.59
CF96-4	3.42	35.99	3.21	4.72	1.17	1.07
CF96-8	3.46	36.09	3.39	4.81	1.21	1.08
Avg	*2.81*	*32.33*	*3.01*	*4.81*	*0.98*	*0.83*
Regolith						
CF00-04	3.26	34.72	3.18	4.91	0.92	0.92
CF00-05	2.96	33.76	2.91	5.18	1.07	0.81
Avg	*3.11*	*34.24*	*3.05*	*5.05*	*1.00*	*0.86*
Grus						
CF96-01	2.57	21.45	2.86	3.63	0.45	0.90
Gravel Group (G)						
CF96-11	3.14	25.07	2.49	4.74	0.76	0.92
CF00-10	3.31	27.58	2.91	4.45	0.78	1.02
CF96-36	2.64	15.91	1.95	4.24	0.78	0.84
CF00-09	2.93	14.65	1.98	3.91	0.71	0.99
Avg	*2.99*	*18.68*	*2.21*	*4.26*	*0.75*	*0.95*
Very Coarse Sand Group (VC)						
CF96-40	3.16	19.94	1.93	5.04	0.38	0.88
CF96-22	2.43	18.09	1.83	4.75	0.70	0.70
CF00-07	3.19	34.97	3.31	4.63	0.82	0.93
Avg	*2.97*	*21.56*	*2.10*	*4.85*	*0.58*	*0.84*
Coarse Sand Group (C)						
CF96-19	2.70	15.22	2.06	3.91	1.01	0.94
CF96-12	2.92	19.81	2.69	3.76	0.84	0.99
CF96-15	3.29	26.96	2.96	4.38	0.89	1.02
CF96-34	4.52	21.67	1.98	5.20	0.57	1.25
CF96-20	3.62	26.15	2.79	4.29	0.68	1.15
CF96-26	3.53	12.33	1.82	3.75	0.87	1.25
Avg	*3.36*	*19.69*	*2.34*	*4.21*	*0.83*	*1.08*
Medium Sand Group (M)						
CF00-17	2.47	15.51	2.07	3.90	0.63	0.84
CF00-06	2.62	23.95	2.84	4.14	0.46	0.86
CF96-07	2.46	17.12	2.27	3.90	0.66	0.83
Avg	*2.54*	*19.35*	*2.44*	*4.01*	*0.56*	*0.85*
Fine Sand Group (F)						
CF00-14	2.58	11.93	1.78	3.69	0.71	0.90
CF00-03	3.03	22.26	2.51	4.31	0.56	0.94
CF96-23	2.27	9.48	1.49	3.64	0.67	0.82
CF00-29	2.84	15.64	2.04	4.08	0.60	0.92
CF96-35	1.92	9.04	1.59	3.38	0.68	0.73
CF96-39	2.07	10.40	1.63	3.61	0.55	0.74
Avg	*2.47*	*12.49*	*1.79*	*3.82*	*0.62*	*0.85*
Very Fine Sand Group (VF)						
CF96-21	2.37	12.96	1.97	3.64	0.52	0.85
CF96-10	2.62	14.70	1.97	4.02	0.60	0.86
Avg	*2.49*	*13.83*	*1.97*	*3.83*	*0.56*	*0.86*

Table 6. Average bedrock-normalized REE ratios of Stepladder samples.

Sample	Ce_{BR}/Sm_{BR}	La_{BR}/Yb_{BR}	Gd_{BR}/Yb_{BR}	La_{BR}/Sm_{BR}	Eu/Eu^*_{BR}	Ce/Ce^*_{BR}	ΣREE	ΣLREE	ΣHREE	ΣLREE/ ΣHREE
Fresh Bedrock										
ST09-02	0.93	1.18	1.09	1.06	0.79	0.84	116.97	110.56	6.40	17.27
CF00-18	0.68	0.68	0.79	0.93	0.93	0.72	63.61	58.51	5.10	11.48
CF96-04	1.22	1.11	1.07	0.98	1.19	1.31	82.04	77.62	4.42	17.55
CF96-08	1.23	1.12	1.13	1.00	1.23	1.31	70.79	66.76	4.03	16.58
Avg	*1.00*	*1.00*	*1.00*	*1.00*	*1.00*	*1.00*	*83.35*	*78.36*	*4.99*	*15.71*
Regolith										
CF00-04	1.16	1.07	1.06	1.02	0.94	1.10	83.85	79.26	4.59	17.27
CF00-05	1.05	1.04	0.97	1.08	1.09	0.97	74.81	70.52	4.29	16.42
Avg	*1.11*	*1.06*	*1.01*	*1.05*	*1.02*	*1.03*	*79.33*	*74.89*	*4.44*	*16.85*
Grus										
CF96-01	0.91	0.66	0.95	0.75	0.46	1.11	174.40	162.51	11.89	13.67
Gravel Group (G)										
CF96-11	1.12	0.78	0.83	0.98	0.78	1.12	61.73	57.97	3.76	15.40
CF00-10	1.18	0.85	0.97	0.92	0.79	1.23	86.86	81.76	5.09	16.05
CF96-36	0.94	0.49	0.65	0.88	0.80	1.03	74.74	68.56	6.18	11.09
CF00-09	1.04	0.45	0.66	0.81	0.73	1.20	118.84	109.11	9.72	11.22
Avg	*1.06*	*0.58*	*0.73*	*0.88*	*0.77*	*1.16*	*85.54*	*79.35*	*6.19*	*12.82*
Very Coarse Sand Group (VC)										
CF96-40	1.13	0.62	0.64	1.05	0.39	1.06	150.99	141.20	9.79	14.42
CF96-22	0.87	0.56	0.61	0.99	0.72	0.84	80.10	74.08	6.02	12.31
CF00-07	1.14	1.08	1.10	0.96	0.84	1.12	78.40	74.29	4.11	18.08
Avg	*1.06*	*0.67*	*0.70*	*1.01*	*0.59*	*1.01*	*103.17*	*96.52*	*6.64*	*14.54*
Coarse Sand Group (C)										
CF96-19	0.96	0.47	0.68	0.81	1.03	1.15	62.86	57.37	5.49	10.45
CF96-12	1.04	0.61	0.89	0.78	0.86	1.21	57.63	53.40	4.23	12.62
CF96-15	1.17	0.83	0.98	0.91	0.91	1.24	78.23	73.42	4.81	15.25
CF96-34	1.61	0.67	0.66	1.08	0.59	1.49	63.97	60.55	3.42	17.72
CF96-20	1.29	0.81	0.93	0.89	0.69	1.41	52.00	49.22	2.78	17.70
CF96-26	1.26	0.38	0.61	0.78	0.89	1.55	40.67	37.30	3.36	11.10
Avg	*1.20*	*0.61*	*0.78*	*0.87*	*0.85*	*1.32*	*59.23*	*55.21*	*4.02*	*13.75*
Medium Sand Group (M)										
CF00-17	0.88	0.48	0.69	0.81	0.64	1.03	140.98	129.05	11.92	10.82
CF00-06	0.93	0.74	0.94	0.86	0.47	1.06	281.65	262.68	18.97	13.85
CF96-07	0.87	0.53	0.76	0.81	0.67	1.01	159.13	146.10	13.03	11.21
Avg	*0.90*	*0.60*	*0.81*	*0.83*	*0.57*	*1.04*	*193.92*	*179.28*	*14.64*	*12.24*
Fine Sand Group (F)										
CF00-14	0.92	0.37	0.59	0.77	0.72	1.11	115.88	104.84	11.04	9.50
CF00-03	1.08	0.69	0.83	0.90	0.58	1.14	213.99	200.26	13.73	14.59
CF96-23	0.81	0.29	0.50	0.76	0.69	1.01	126.52	112.48	14.04	8.01
CF00-29	1.01	0.48	0.68	0.85	0.62	1.13	156.43	143.74	12.69	11.32
CF96-35	0.68	0.28	0.53	0.70	0.69	0.91	117.25	102.75	14.50	7.08
CF96-39	0.73	0.32	0.54	0.75	0.56	0.92	176.48	157.37	19.11	8.23
Avg	*0.88*	*0.39*	*0.59*	*0.79*	*0.63*	*1.04*	*151.09*	*136.91*	*14.19*	*9.65*
Very Fine Sand Group (VF)										
CF96-21	0.84	0.40	0.65	0.76	0.53	1.05	181.53	164.54	16.99	9.68
CF96-10	0.93	0.45	0.65	0.84	0.62	1.05	200.03	182.83	17.19	10.63
Avg	*0.89*	*0.43*	*0.65*	*0.80*	*0.58*	*1.05*	*190.78*	*173.68*	*17.09*	*10.16*

and Kamber, 2006) and are expressed as follows:

$$Ce^*_{CN} = (2 * Pr_{CN} - Nd_{CN})$$

Using Sm_{CN} and Gd_{CN}, Eu-anomalies are calculated from a geometric average where it is assumed that the ratio between near neighbor concentrations is constant (McLennan, 1989) and are expressed as follows:

$$Eu^*_{CN} = (Sm_{CN} * Gd_{CN})^{1/2}$$

Two bedrock samples have negative chondrite-normalized Ce (0.70 and 0.59) and Eu anomalies (0.79 and 0.91), while two have slightly positive chondrite-normalized Ce (1.07 and 1.08) and Eu (1.17 and 1.21) anomalies (Table 5). Average Stepladder bedrock is characterized by a negative chondrite-normalized Ce anomaly (0.83) and a negligible Eu anomaly (0.99).

Relative to Phanerozoic TTG and Mesozoic-Cenozoic granite compositions (Condie, 1993), average Stepladder granodiorite is moderately depleted in Rb, Th, Ti, and U, and significantly depleted in Sc (~20x). Strontium and Ba are similar in concentration to Phanerozoic TTG, whereas Zr and Hf are slightly enriched (Fig. 3F).

6. Characterization of the weathered source rock: Stepladder regolith and grus

6.1. Petrology

Formed through *in situ* weathering, regolith and grus (Fig. 6) comprise the friable rock layers covering and shedding from bedrock (Taylor and Eggleton, 2001). Regolith maintains a primary igneous fabric (Fig. 6A, B) until it disintegrates into grus through grain-by-grain fragmentation of large feldspar and quartz grains. Stepladder regolith is characterized by the onset of fracturing likely induced by biotite expansion upon oxidation (Buss et al., 2008) and its

Figure 6. Photographs and geochemical plots of Stepladder regolith and grus. (A) Field photograph of regolith; note that regolith maintains primary granitic texture. (B) Detailed photograph of regolith; dashed lines trace fractures, most of which follow grain boundaries and radiate from or propagate through biotite. (C) Photomicrograph (crossed polarized light) of fractures (white arrows) extending from altered plagioclase core into adjacent quartz. (D) Photomicrograph (plane light) of an irregular fracture cutting through biotite (black arrow) and K-feldspar along mineral grain boundaries. Abbreviations in (B, C and D): Ap, apatite; Bt, biotite; Ksp, K-feldspar; Pl, plagioclase; Q, quartz; Fxt, fracture; Hm, hematite; Mt, magnetite; Op, opaque. (E) Chondrite-normalized REE plot; chondrite composition from McDonough and Sun (1995). Gray boxes highlight Ce and Eu anomalies. (F) Average fresh bedrock-normalized spider plot of regolith (CF00-04 and CF00-05) and grus (CF96-01). Gray boxes highlight anomalous enrichment of Co, Ni, Cr, and Sc in all sediment samples. Note the similar patterns of regolith and bedrock in both charts (E) and (F).

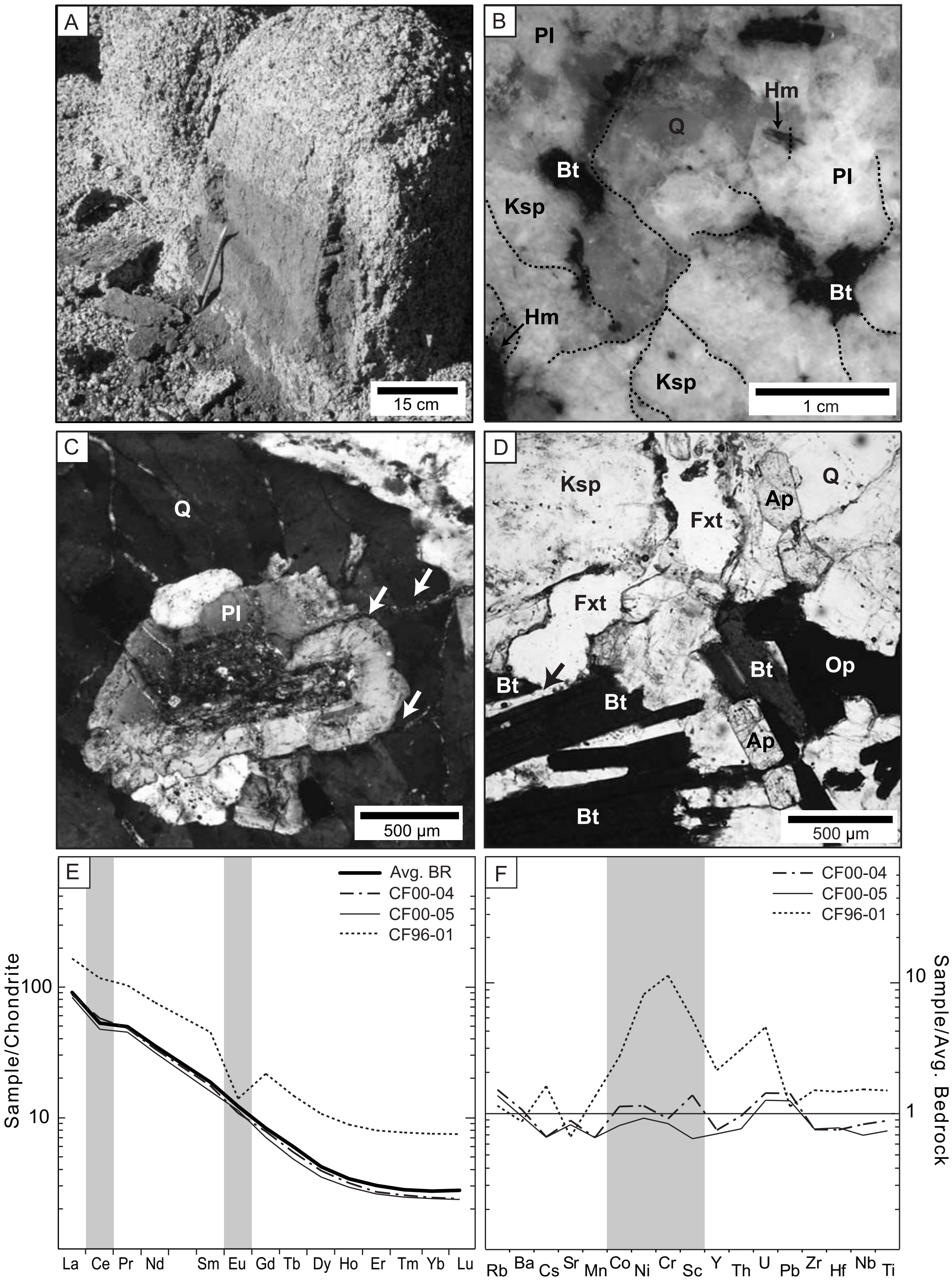
A
15 cm
B
Pl
Hm
Q
Bt
Pl
Ksp
Bt
Hm
Ksp
1 cm
C
Q
Pl
500 µm
D
Ksp
Fxt
Ap
Q
Fxt
Bt
Bt
Bt
Op
Ap
Bt
500 µm
E
Avg. BR
CF00-04
CF00-05
CF96-01
Sample/Chondrite
100
10
La Ce Pr Nd Sm Eu Gd Tb Dy Ho Er Tm Yb Lu
F
CF00-04
CF00-05
CF96-01
Sample/Avg. Bedrock
10
1
Rb Ba Cs Sr Mn Co Ni Cr Sc Y Th U Pb Zr Hf Nb Ti

initial transformation to secondary clays (e.g. vermiculite; Graham et al., 2010). Most fractures follow crystal boundaries (Fig. 6B) or cut through weathered biotite and plagioclase grains along cleavage planes, and locally propagate into adjacent crystals (Fig. 6C, D). K-feldspar becomes dusty from minor weathering (Fig. 6C), while quartz remains unaltered (Fig. 6C, D). Irregular fracture networks can cut these grains independent of crystal boundaries or cleavage orientation (Fig. 6C, D). Fracture walls tend to be accordant surfaces (e.g., Delvigne, 1998, p. 69) that cut at right or oblique angles to one another and are coated by brown autochthonous material (Fig. 6D). Along with the fine brown material, rock and monocrystalline fragments accumulate in the regolith fractures. Except for the increased porosity and clay content, Stepladder regolith greatly resembles fresh bedrock texture, while both regolith and grus have comparable mineralogy.

Despite the increased surface area associated with fracture and sediment development, dissolution features and secondary clays are localized within regolith and grus (Girty et al., 2003). Secondary alteration is confined to plagioclase cores and twins (Fig. 6C), exsolved phases in perthite, and biotite aggregates (Figs. 6D, A1.15). Minute inclusions of clays and muscovite are responsible for the cloudy habit of plagioclase (Fig. A1.15) and exsolved perthite phases (Fig. 6C, D). The pseudomorphic replacement of biotite by chlorite and opaque Fe-oxides occurs along margins and cleavage planes and stains contiguous leucocratic minerals red (Fig. 6D, A1.15). Apatite is associated with most biotite aggregates and, even where rimmed by secondary phases, no grain shows evidence of intense weathering or dissolution (Fig. 6D). Euhedral opaque oxides are associated with oxidized biotite grains and red-brown stains (Fig. A1.15), suggesting the occurrence of minor alteration, which is consistent with incipient weathering in other paleosols (e.g., Nesbitt and Markovics, 1997).

6.2. *Geochemistry*

6.2.1. *Major elements*

Stepladder regolith is weakly peraluminous, with A/CNK values ranging from 1.00 to 1.03, while grus is more peraluminous with an A/CNK value of 1.15 (Appendix A2, Table A2.1). In A–CN–K space (Fig. 4B; Table 3), regolith closely resembles bedrock components. Grus shows a greater depletion in Na_2O and CaO* relative to bedrock. Only grus is relatively enriched in Al_2O_3 (Fig. 4B) and FeO + MgO (Fig. 5B). The MnO and MgO contents are depleted in regolith but enriched in grus, along with TiO_2 and Fe_2O_3. Low, CO_2-corrected, CIA values of regolith and grus (50 and 53, respectively; Table 3) indicate that, like bedrock, they have experienced only a minimal amount of chemical weathering.

6.2.2. *Rare earth and trace elements*

Chondrite-normalized REE patterns of regolith (Fig. 6E) are nearly identical to that of average bedrock. Like average bedrock, regolith also lacks an Eu anomaly and has slightly negative Ce anomalies = 0.92 and 0.81 (Fig. 6E; Table 5). The chondrite-normalized REE pattern of grus (sample CF96-01) begins to show difference from that of bedrock. While the overall LREE to HREE fractionation is similar, grus is characterized by a large negative Eu anomaly (Eu/Eu*= 0.45), and an enrichment in total REE abundance (Fig. 6E; Tables 4,5).

Regolith differs only slightly (less than a factor of 3) from the trace-element composition of average fresh bedrock (Fig. 6F; Table 4). The behavior of the transition metals is slightly different between the two regolith samples, as one sample is slightly depleted and the other is slightly enriched in Co, Ni, Cr, and Sc relative to bedrock (Fig. 6F), an effect likely the result of very low concentrations of these elements (≈ 1 ppm, Table 4). Although grus has light ion lithophile element (LILE: K, Rb, and Ba) concentrations similar to those of average bedrock and regolith, it is consistently enriched in Mn, the transition metals (Co, Ni, Cr, and Sc), and all of the HFSE (Y, Th, U, Zr, Hf, Nb, and Ti) except for Pb, which is present at concentrations similar to those in regolith. The mobile element concentrations (K, Rb, Ba, Cs, and Sr) of regolith and grus are comparable to that of average bedrock, whereas the abundances of immobile elements in grus, particularly Co, Ni, Cr, and Sc, are the most enriched (up to a factor of 10) relative to average bedrock (Fig. 6F), a feature common to caliche, but at much greater abundances.

7. Characterization of Stepladder sediments

7.1. Rationale for sample grouping

Twenty-four sediment samples were examined to identify potential variables influencing composition and texture. To test whether natural geochemical groupings would emerge, all sediment samples were first grouped as a single population (e.g., Fig 4C), and compared to bedrock, regolith, and grus. Second, sediments were grouped by geomorphic zone (e.g., Fig. 4D) to determine whether these zones, apparent in aerial imagery, are linked compositional variations. Third, sediments were grouped by mean grain size (e.g., Fig. 4E; Table 1) to determine whether sorting effects govern any compositional variation.

When plot in A–CN–K and A–CNK–FM compositional space (Figs. 4, 5), sediments grouped as a whole (Figs. 4C, 5A) and by geomorphic zone (Figs. 4D, 5C) show no clear compositional trends. Consequently, these groupings are not considered as strongly effecting the sediment composition (select plots in Appendix A2, p. 136). Rather, because of the apparent grain-size control on the composition (Figs. 4E, 5D), the remainder of the discussion is focused on sediment sorting characteristics, with each sample being classified to one of six naturally occurring groups: gravel group (*G*), very coarse sand group (*VC*), coarse sand group (*C*), medium sand group (*M*), fine sand group (*F*), very fine sand group (*VF*).

7.2. Sedimentary petrology – Textures

7.2.1. Gravel group (G)

The four sediment samples in group *G* (Table 1; Appendix A1.4.1, p. 106) have mean grain sizes ranging from -1.3 to -0.3 Φ (gravel to very coarse sand; Fig. 7A). Measured grain sizes range from gravel to coarse silt, with the exception of one sample that consists of sediment coarser than fine sand (<3 Φ). Texturally, the samples are poorly to very poorly sorted, muddy to sandy granule gravels (Table 1). Of the four samples, all are very poorly sorted except for CF96-11, which is poorly sorted. All samples in group *G* have strongly fine-skewed, platykurtic to mesokurtic size frequency distributions. All grains are angular (mean ρ=1.25), but vary in form depending on grain type. Rock fragments and monomineralic plagioclase, quartz, and K-feldspar grains are compact to compact-bladed or compact-elongate, while biotite grains are platy to bladed.

7.2.2. Very coarse sand group (VC)

The three sediment samples that fall in group *VC* (Table 1; Appendix A1.4.2, p. 111) have mean grain sizes of very coarse sand (-0.2 to -0.1 Φ; Fig. 7B). They have measured grain sizes that range from gravel to coarse silt and, texturally, are poorly sorted gravelly sands to sandy granule gravels (Table 1). All three very coarse sand samples are poorly sorted and have size frequency distributions that are near-symmetrical to fine-skewed and platykurtic to mesokurtic. On average, all grains are angular (mean ρ=1.1). Rock fragments and monomineralic grains of plagioclase, quartz, and K-feldspar are compact-bladed to compact-elongate. Individual biotite grains are bladed to very platy.

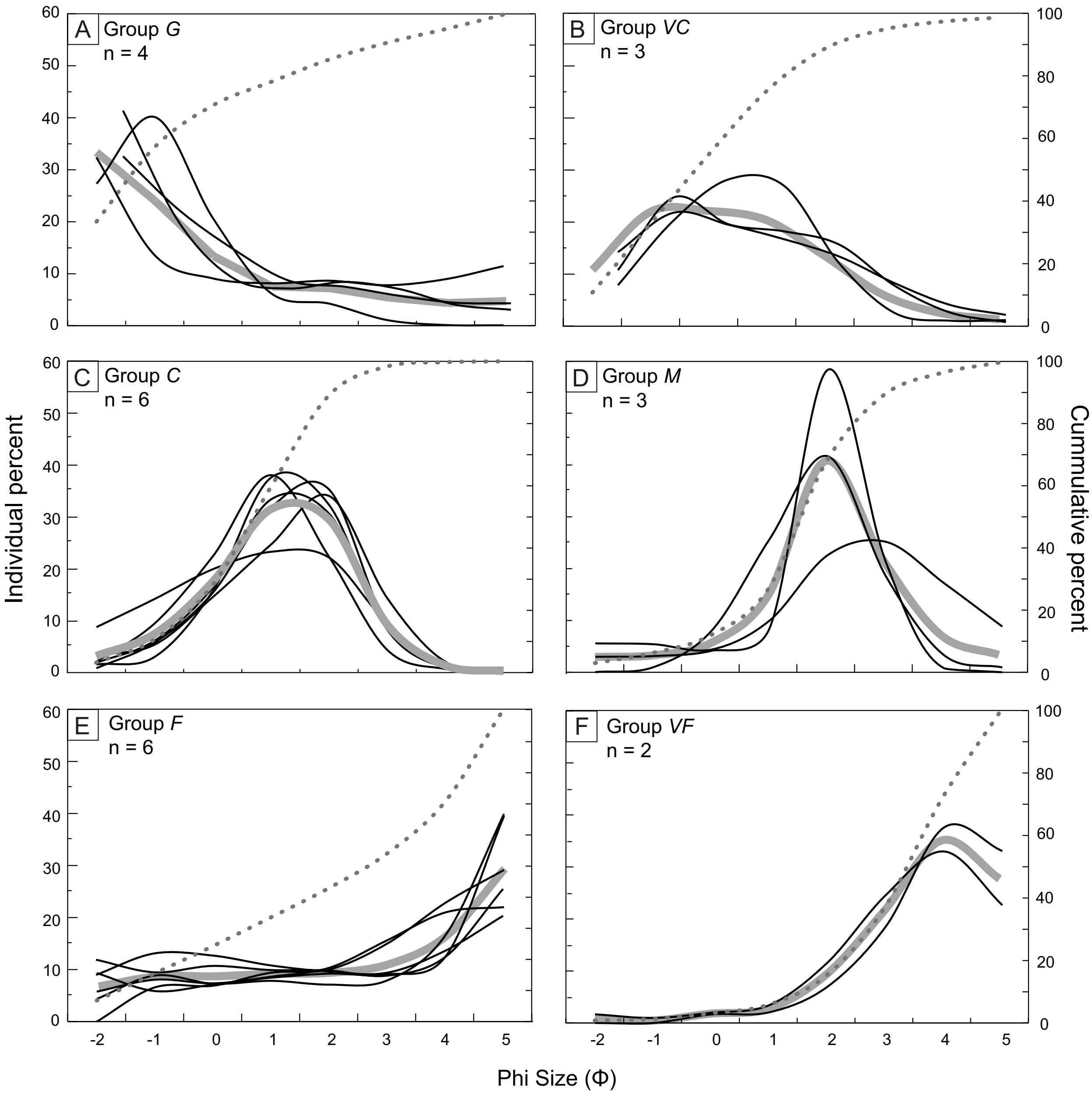

Figure 7. Frequency and cumulative curves of sediment samples grouped by mean grain size. Frequency distribution curves (thin black lines) of individual samples (n = number of samples) and group averages (thick gray lines) are reported in individual percent. Cumulative distribution curves of group averages (dotted lines) are reported in cumulative percent. (A) Gravel group, (B) very coarse sand group, (C) coarse sand group, (D) medium sand group, (E) fine sand group, and (F) very fine sand group.

7.2.3. Coarse sand group (C)

The six sediment samples that fall in group *C* (Table 1; Appendix A1.4.3, p. 116) have mean grain sizes ranging from 0.2 to 0.9 Φ (coarse sand; Fig. 7C). They are poorly sorted, gravelly sands with measured grain sizes ranging from gravel to very fine sand (Table 1). All samples in group *C* are poorly sorted and have a near-symmetrical to coarse-skewed, platykurtic to mesokurtic size frequency distribution. Grains are mostly angular (mean ρ=1.3), however individual biotite grains can be sub-angular. Rock fragments and monomineralic grains of plagioclase, quartz, and K-feldspar are compact-bladed to compact-elongate, while biotite grains are bladed to very platy.

7.2.4. Medium sand group (M)

The three sediment samples that fall in group *M* (Table 1; Appendix A1.4.4, p. 121) have mean grain sizes ranging from 1.3 to 1.9 Φ (medium sand; Fig. 7D). All three samples have measured grain sizes that range from gravel to coarse silt and are texturally diverse. One sample, a gravelly muddy sand, is poorly sorted while the other two samples, gravelly sands, are moderately well sorted (Table 1). All three samples are coarse-skewed, but CF00-17 is mesokurtic, CF96-07 is leptokurtic, and CF00-06 is very leptokurtic. Individual grains within group M are more rounded than those of the coarser groups (mean ρ=3.1). Rock fragments and monomineralic grains of quartz and K-feldspar are compact to compact-bladed and are angular. Monomineralic plagioclase grains are compact-bladed to elongate and are angular to sub-angular, while individual biotite grains are bladed to very platy and are sub-angular to slightly sub-rounded.

7.2.5. Fine sand group (F)

The six sediment samples that fall in group *F* (Table 1; Appendix A1.4.5, p. 126) have mean grain sizes that range from 1.4 to 2.6 Φ (medium to fine sand; Fig. 7E). Measured grain sizes range from gravel to coarse silt. Texturally, all samples are very poorly sorted, gravelly muddy sands except for one, which is a poorly sorted, gravelly sand (Table 1). All samples in group *F* have a near symmetrical to strongly coarse-skewed, platykurtic size frequency distribution. Grains are mostly sub-angular (mean ρ=2.3), but vary with grain type. Rock fragments and monomineralic grains of plagioclase, quartz, and K-feldspar angular to sub-angular and are compact-bladed to compact-elongate. Individual biotite grains are sub-angular to sub-rounded and are bladed to very platy.

7.2.6. Very fine sand group (VF)

The two sediment samples that fall group *VF* (Table 1; Appendix A1.4.6, p. 131) have mean grain sizes of 3.1 and 3.5 Φ (very fine sand; Fig. 7F). Measured grain sizes range from gravel to coarse silt. One sample, however, only contains sediment finer than very coarse sand (<0 Φ). Texturally, one sample is a gravelly sand and one is a sandy gravel (Table 1). Both are poorly sorted and have coarse-skewed, mesokurtic size frequency distributions. Compared to the other sediments, grains in group *VF* are the most rounded (mean ρ=3.3). Rock fragments and monomineralic grains of plagioclase, quartz, and K-feldspar are mostly sub-angular and are compact to compact-bladed. Individual biotite grains are sub-angular to sub-rounded and are platy to very platy.

7.3. Sedimentary petrology – Mineralogy

The primary minerals quartz, plagioclase, K-feldspar, and biotite are found in all sediment samples (Fig. 8) and because they maintain similar petrographic characteristics over all grain sizes, they are described by mineral phase here. Additional descriptions and figures are included in Appendix A1.4, p. 102 - 135.

7.3.1 Quartz

Quartz occurs as angular, clear, mono- and polycrystalline grains or as anhedral crystals in rock fragments. Most quartz exhibits slight-to-strong undulose extinction (few show straight extinction), and commonly contains thin trails of fluid inclusions (Fig. 8B). Only rarely does quartz include accessory phases or small lath-like biotite and plagioclase grains. As expected given its chemical stability, quartz is essentially unaltered within the Stepladder sediments. While quartz is abundant in all sediment samples, it is more common in medium sand and coarser sized fractions (groups *VC* and *G*). Individual quartz grains larger than fine sand are mostly quartz – feldspar, quartz – biotite, or quartz – quartz polycrystalline rock fragments (Fig. 8A, B), while very fine sand and silt-sized grains are predominately monocrystalline quartz.

7.3.2 Plagioclase

Plagioclase is common in all sediment samples, and particularly abundant in the finer grain-size groups (groups *VF* and *M*). Using the extinction angle between polysynthetic twin sets, the plagioclase is determined to be oligoclase in composition (average = An_{27}; range = An_{21} - An_{34}). Most grains show albite twinning, oscillatory zoning, or no apparent twinning (Fig. 8C, D); only select grains display complex combinations of polysynthetic twinning (Fig. 8C). Nearly all plagioclase crystals are clear with well-defined twins (Fig. 8C), as would be expected in

Figure 8. Photographs and geochemical plots of Stepladder sediments. (A) Transmitted light image showing rock fragments in group *C* (CF96-11). (B) Photomicrograph (crossed polarized light) detailing mono- and polycrystalline quartz. (C) Photomicrograph (plain light) showing nature of K-feldspar and plagioclase. Note the rippled texture of the K-feldspar (upper right) and the albite twinning of the plagioclase grain (lower center). (D) Photomicrograph (plain light) showing nature of biotite and angular to sub-angular monomineralic grains: K-feldspar, quartz, and plagioclase. Note the lath-shaped biotite with anhedral opaque oxides extending along cleavage planes. Abbreviations in (B, C and D): Bt, biotite; Ksp, K-feldspar; Pl, plagioclase; Q, quartz; Op, opaque. (E) Chondrite-normalized REE plot; chondrite composition from McDonough and Sun (1995). Gray boxes highlight Ce and Eu anomalies. (F) Average fresh bedrock-normalized trace element plot of sediment grain-size groups. Gray boxes highlight anomalous enrichment of Co, Ni, Cr, and Sc in all sediment samples.

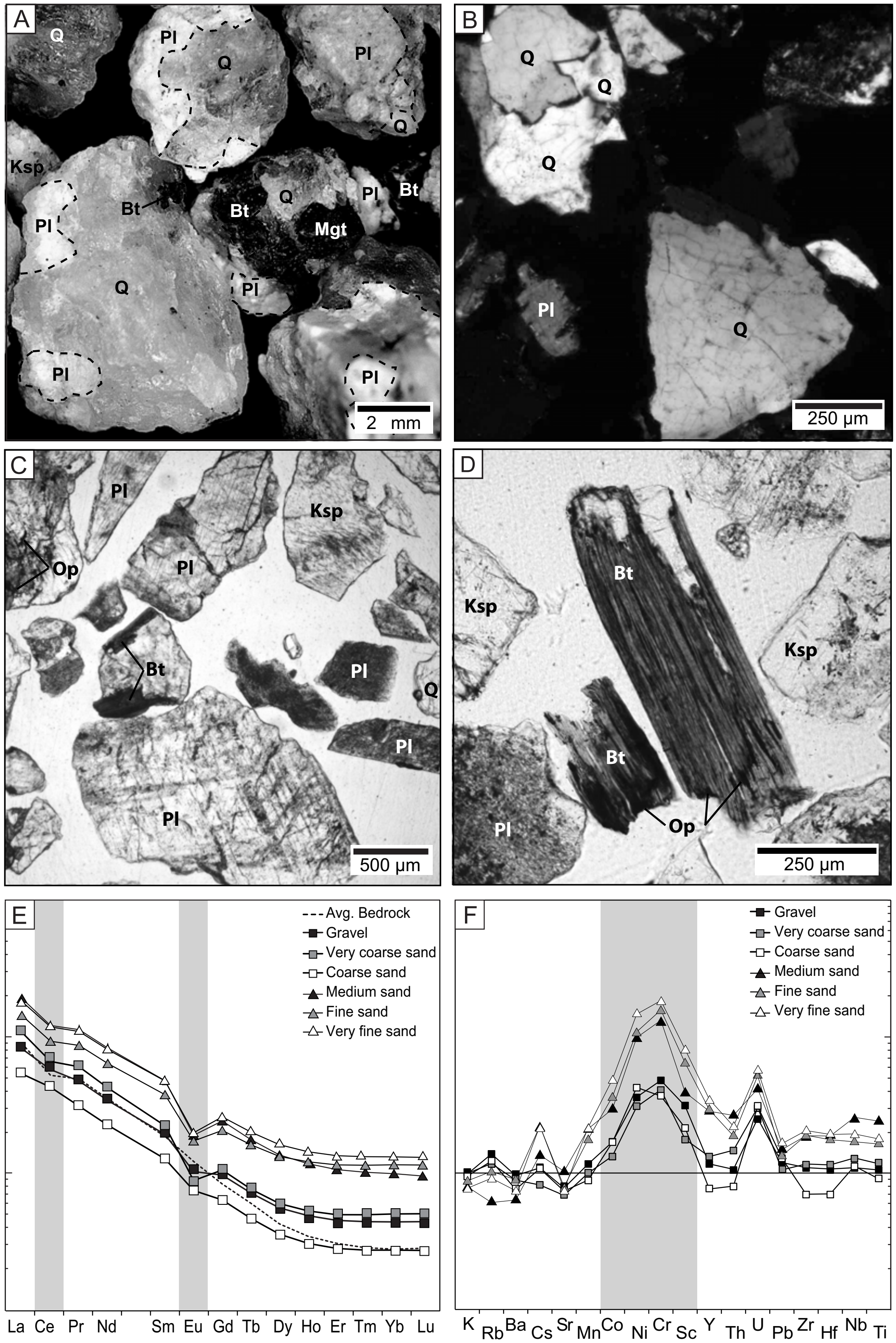
A
Q
Pl
Q
Pl
Q
Ksp
Bt
Pl
Q
Bt
Mgt
Pl
Bt
Q
Pl
Pl
Pl
2 mm
B
Q
Q
Q
Pl
Q
250 µm
C
Pl
Ksp
Op
Pl
Bt
Pl
Q
Pl
Pl
500 µm
D
Bt
Ksp
Ksp
Bt
Pl
Op
250 µm
E
Avg. Bedrock
Gravel
Very coarse sand
Coarse sand
Medium sand
Fine sand
Very fine sand
Sample/Chondrite
100
10
La Ce Pr Nd Sm Eu Gd Tb Dy Ho Er Tm Yb Lu
F
Gravel
Very coarse sand
Coarse sand
Medium sand
Fine sand
Very fine sand
Sample/Average Fresh Bedrock
10
1
K Rb Ba Cs Sr Mn Co Ni Cr Sc Y Th U Pb Zr Hf Nb Ti

sediment that has not experienced much hydrolysis. In select grains where minor weathering is apparent, secondary clays are concentrated along cleavage and twin planes, fractures, and Ca-rich zones, creating a more cloudy appearance (Fig. 8C, D). Monocrystalline plagioclase grains are more abundant in group *M*, *F*, and *VF* sediments, but polymineralic rock fragments (that include plagioclase) of the bedrock are dominant in groups *C*, *VC*, and *G* (Fig. 8C).

7.3.3 K-feldspar

K-feldspar is also common in all sediment groups and predominately occurs as perthite, where exsolved Ca-Na-rich plagioclase feldspar forms a patchwork to rippled texture (Fig. 8C). While perthitic grains are mostly clear, some develop a slight dusty appearance, where clays preferentially replace plagioclase-rich zones of perthite (Fig. 8C, D). Where plagioclase grains are not perthitic, they occur as clear, angular orthoclase grains that rarely include patchy secondary clays. Compared to the plagioclase grains within the sediments, K-feldspar is replaced by fewer secondary phases. Monomineralic and K-feldspar – containing polycrystalline rock fragments are both common, but their abundances vary with grain size. K-feldspar – containing rock fragments are most abundant in the coarser-grained sediment groups (especially groups *G* and *VC*), whereas monomineralic grains dominate sediments in groups *F* and *VF*.

7.3.4 Biotite

Most biotite grains within the sediment retain a compact, platy shape (Fig. 8C, D), but develop edges that expand in a fan-like manner. Compared to bedrock, biotite in sediment has a more muted brown-green pleochroism and more opaque oxides that extend along cleavage planes. Individual biotite grains show substantial alteration, as nearly 50 % of the modal biotite has been replaced by chlorite and opaque Fe-(oxy)hydroxides (Fig. 8C, D). The behavior of biotite differs from that of the other primary minerals because it is more readily broken down during physical weathering. As a result, platy monomineralic biotite grains are more abundant in the sediments than polycrystalline-biotite rock fragments, which tend to occur in coarse sediment larger than ~1.5 Φ.

7.3.5 Accessory phases

Zircon and apatite are among the most abundant phases identified in the sediments and mostly occur as inclusions in biotite and plagioclase. Within the finer-grained sediments, apatite also occurs as individual grains that exhibit little alteration or dissolution. Titanite and allanite were identified as inclusions (typically in plagioclase or biotite crystals) in large rock fragments and were not readily identified in the fine sediment fractions.

7.3.6 Modal mineralogy

With only a small, but important, amount of mineralogical variation in the sediment groups relative to average bedrock and each other, and many shared characteristics, the modal trends for all groups are discussed together. In quartz – total feldspar – lithic fragment (QFL) space, all six grain-size groups classify as arkoses (Folk, 1974), but there is considerable scatter of the data in the total amount of quartz (Fig. 9A). Following the modified Gazzi-Dickinson point-counting technique (Dickinson, 1970; Ingersoll et al., 1984), coarse lithic fragments are classified as individual minerals, although the proportion of rock fragments was also determined. As long recognized in the breakdown of granitic bedrock (e.g., McEwen, 1959), finer grain sizes concentrate total feldspar relative to coarser grain sizes, and to the composition of average bedrock (Fig. 9A); conversely, coarser grain sizes are depleted in feldspar with respect to

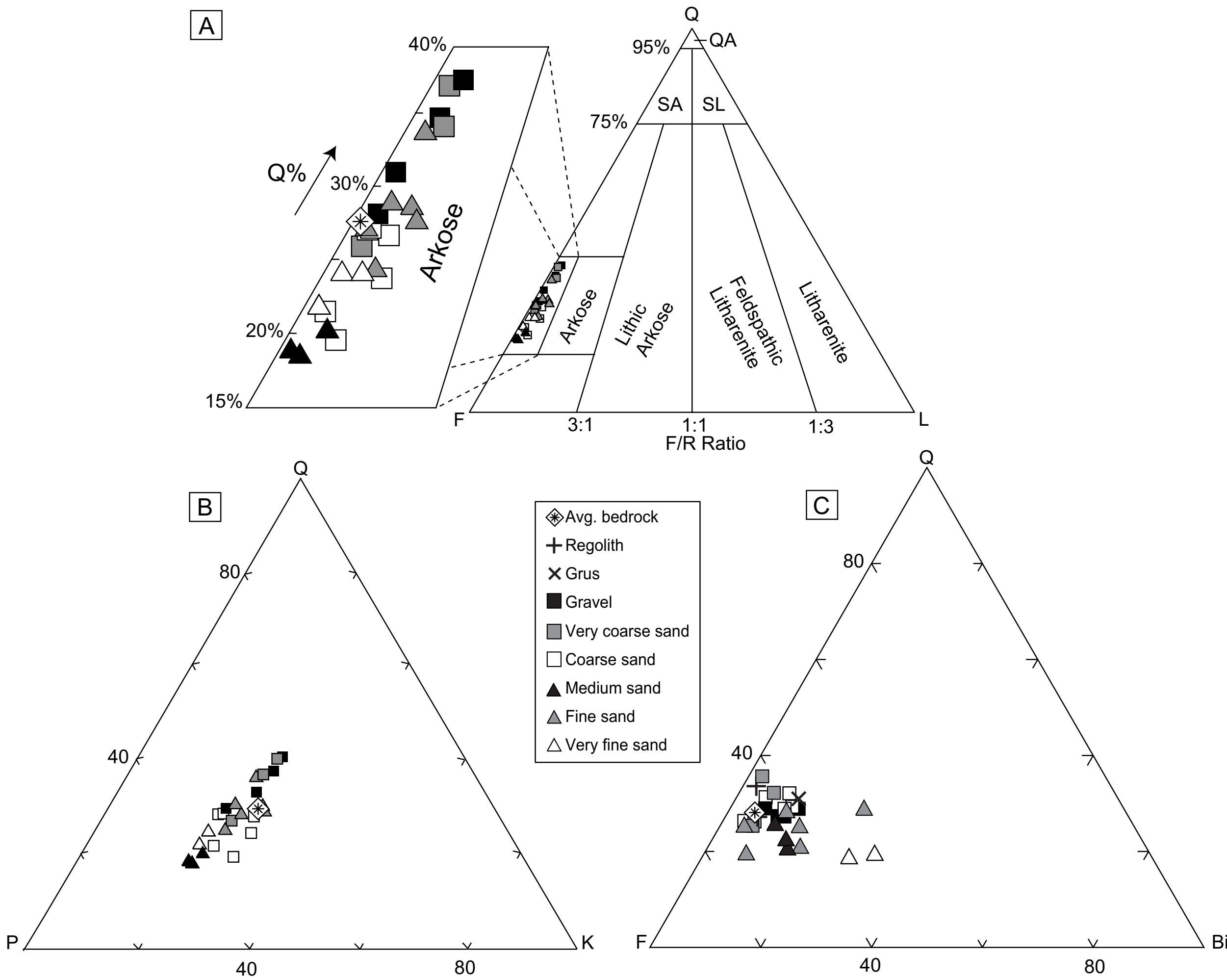

Figure 9. QFL, QPK, and QFB plots of Stepladder sediments grouped by grain size. Note data were collected according to the Gazzi-Dickinson point-counting method, where Q = total quartz; P = total plagioclase; K = total K-feldspar; F = total plagioclase + K-feldspar; L = volcanic rock fragments; Bi = biotite. (A) QFL rock classification; all data plot within the arkose field. Abbreviations: QA, quartz arenite; SA, subarkose; and SL, sublithic arenite. (B) QPK plot of sediments and average bedrock. (C) QFB plot of sediments and average bedrock. Note the finer sediments are the most enriched in biotite.

bedrock. From a plate tectonics perspective (e.g., Dickinson and Suczek, 1979), the sediments all lie in the basement uplift field (Appendix A2, Fig. A2.1).

Separation of the feldspars on a quartz – plagioclase – K-feldspar plot (QPK; Nesbitt et al., 1997; Fig. 9B) reveals that the feldspar enrichment in some grain sizes (group *VF, M,* and select *M* sediments) in QFL space results largely because of plagioclase, which undergoes an approximately 20 % increase relative to average bedrock, with essentially no change in K-feldspar. Consequently, the data scatter along a trajectory subparallel to plagioclase – quartz join. The Stepladder data trend contrasts with the prediction for a trajectory of sediments derived from physical processes, which was considered to be directed straight towards the Q-apex from the bedrock composition (Nesbitt et al., 1997). The original premise for that trajectory was based on the notion that because of the similar mechanical properties of plagioclase and K-feldspar there should not be any change in their proportions from abrasion, although this study indicates that even under the slightest amount of chemical weathering coupled with very little transport, plagioclase mechanically breaks down ahead of K-feldspar. Because of this, the Stepladder data form a trend much more akin to one associated with more extensive chemical weathering (Nesbitt et al., 1997), even though such effects are very minor in this study.

Modal mineralogy data are also projected in quartz – total feldspar – biotite space (Fig. 9C) because of the variation in amount of biotite in the sediments. While coarser deposits (groups *G*, *VC* and *C*), closely resemble bedrock, the finer deposits (particularly groups *F* and *VF*) show a clear preferential concentration of biotite, a phenomenon recognized by Young and Nesbitt (1998). One consequence of this is that elemental oxides concentrated in biotite, such as FeO and MgO, that carry provenance information may show considerable departure from the bedrock. In all three modal mineralogy projections, therefore, potentially considerable variation occurs in sediment mineralogy with respect to bedrock.

7.4 Geochemistry

7.4.1. Major elements

Major-element oxide abundances (Table 3) of the 24 sediment samples, as projected in A–CN–K space, are relatively similar to that of average bedrock (Fig. 4). Samples within the same grain-size group, have major oxide abundances that differ less than 0.60 wt. %. All sediments have low CIA values (ranging from 50-53), indicating that, like fresh and decomposed bedrock, are not significantly weathered (Fig. 4; Table 3). There is a concomitant decrease in wt. % SiO_2 with decreasing grain size. All sediments are enriched in FeO + MgO (Fig. 5D) relative to bedrock, except for those of group *C,* which are slightly depleted in FeO + MgO. Groups *G* and *VC* are slightly depleted in Al_2O_3 and CaO* + Na_2O, while those in groups *C*, *M*, *F*, and *VF* are depleted in K_2O and slightly enriched in Al_2O_3 and CaO* + Na_2O (Fig. 4E).

7.4.2. Rare earth and trace elements

Because sediment REE patterns within each group are similar in shape, averages for the groups were calculated (Fig. 8E). Average chondrite-normalized REE patterns for each group, as well as the pattern for average bedrock, are shown in Figure 8E. All groups show an overall concentration of LREE relative to HREE (La_{CN}/Yb_{CN} = 12.49 - 21.56; Table 5), with the LREE more fractionated (La_{CN}/Sm_{CN} = 3.81-4.85; Table 5) than the HREE (Gd_{CN}/Yb_{CN} = 1.79-2.44; Table 5). As grain size decreases, slope of the HREE slightly decreases, although the LREE are consistent across grain sizes (Fig. 8E). Negative europium anomalies characterize all the sediment groups (Eu/Eu* = 0.56-0.83; Table 5), which stands in contrast to average bedrock that has no anomaly (Eu/Eu* = 0.99; Table 5). As is common, total REE increases considerably as grain size and wt. % SiO_2 decreases (∑REE = 59.23-193.92 ppm; Table 5). While the broad REE patterns of the sediments and average bedrock show commonalities, clear differences between them indicate that loss of provenance information begins early in the sediment production process.

Understanding these differences requires a closer examination of sediment geochemistry relative to the bedrock (Fig. 10). In Figure 10A, the average REE pattern of each group shows that, relative to bedrock, most sediments are enriched in HREE relative to LREE (La_{BR}/Yb_{BR} = 0.39-0.67; Table 6). Although generally flat, there is a systematic increase across the LREE (La_{BR}/Sm_{BR} = 0.79-1.01; Table 6), and HREE (Gd_{BR}/Yb_{BR} = 0.59-0.81; Table 6). The average of each group also shows the development of prominent negative Eu anomalies (Eu/Eu* = 0.57-0.85; Fig. 10A; Table 6), with the most prominent anomalies in the finer grain sizes (groups *VF*, *F*, and *M*) and small, but persistent, positive Ce anomalies that are larger in coarser grain sizes (groups *C*, *VC*, *G*; Ce/Ce* = 1.01-1.32), but particularly in group *C* (Fig. 10A; Table 6). Individual sample patterns of each group are shown in Figure 10B-G. LREE fractionation is nearly absent in groups *G*, *VC*, and *M* (Fig. 10B, C, E), but slightly more apparent in groups *C*, *F*, and *VF* (Fig. 10D, F, G). Positive HREE fractionation is present in all groups. While some samples from each group display some anomalous Ce behavior, every sample in group *C* (Fig. 10D) retains a positive Ce anomaly.

Regardless of grain size, all sediment trace element abundances (Fig. 8F; Table 4) differ significantly from the average bedrock trace element composition. Concentrations of K, Rb, Ba, Sr, and Pb fractionate the least from average bedrock composition, while concentrations of Co,

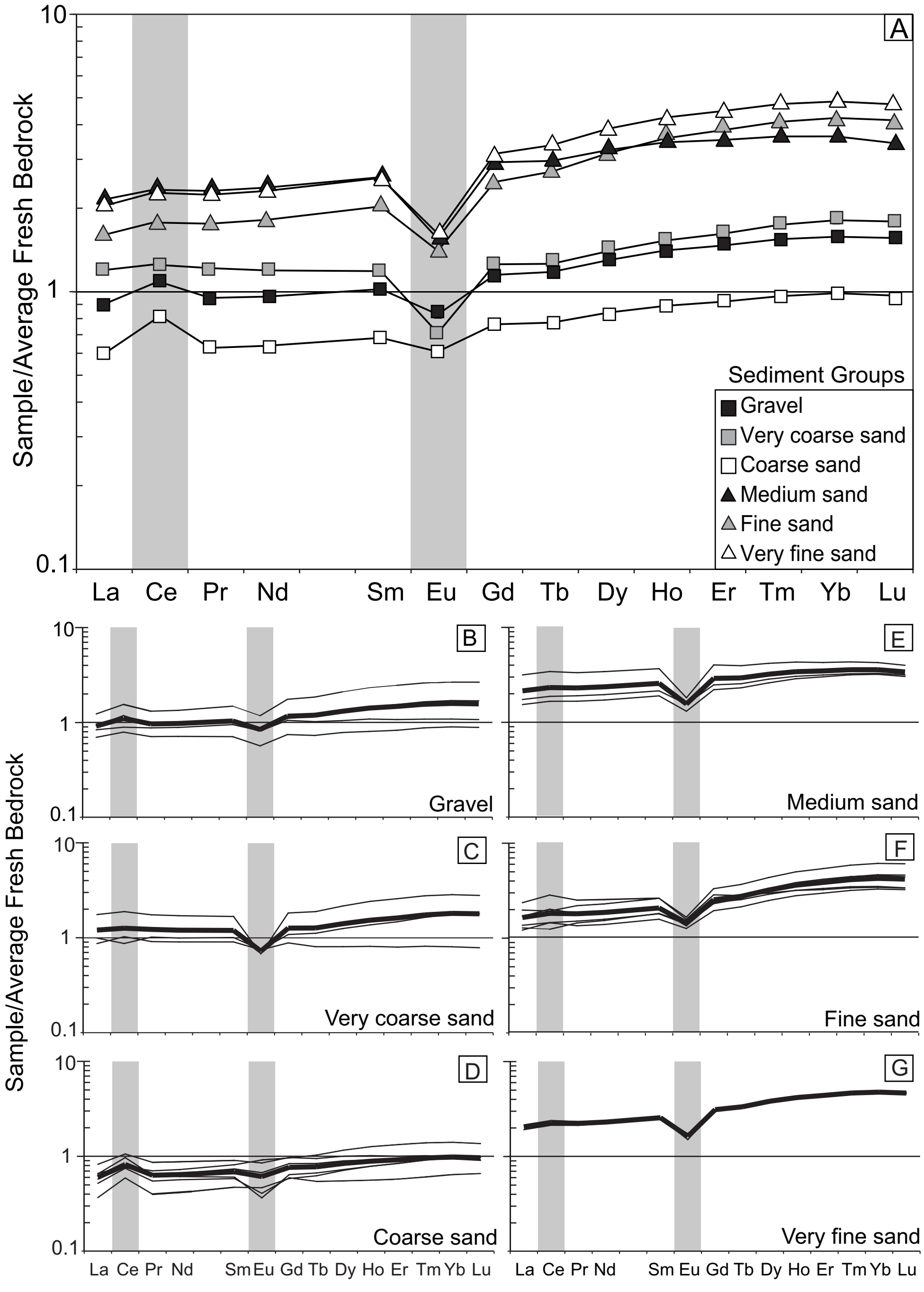

Figure 10. Average bedrock-normalized REE plots of sediment grain-size groups. (A) Average REE concentrations of the sediment grain-size groups. REE concentrations of individual sediment samples are plot in: (B) gravel group, (C) very coarse sand group, (D) coarse sand group, (E) medium sand group, (F) fine sand group, and (G) very fine sand group. Thin black lines represent individual samples; bold black lines represent average REE patterns seen in plot (A); gray boxes highlight Ce and Eu anomalies. Note the groups *G, VC*, and *C* best reflect the REE signature of average fresh bedrock. Group *C* sediments are characterized by positive bedrock-normalized Ce anomalies; fine sediments (groups *F* and *VF*) are characterized by greater HREE fractionation and diverge the most from the average fresh bedrock REE pattern.

Ni, Cr, Sc, and U fractionate the most. All sediments have similar LILE concentrations as average bedrock, except for group *M*, which is slightly depleted in Rb, and groups *F* and *VF*, which are slightly enriched in Cs. With the exception of group *C*, which has sediments slightly depleted in Y, Th, Zr, and Hf, all groups are enriched in HFSE (Fig. 8F). Of particular note is the significant enrichment of transition metals relative to bedrock, regardless of grain size.

8. Provenance reconstruction

This study accounts for a number of variables in order to test provenance indicators. Eliminating concerns related to mixing of source compositions and recycling, the project focuses on first-cycle sediment derived from a single pluton that has little petrologic variation. Sediments, thus, have a unique source whose composition is well understood. By selecting to examine sediments actively being deposited in an increasingly arid climate, chemical weathering plays a nearly negligible influence on sediment composition. Lastly, sediments used in this study span a wide range of naturally sorted grain sizes, and so any compositional effects related to sorting can be determined. In this context, if sediments are likely to directly identify provenance, this study should reveal it. Below, a variety of traditional geochemical provenance indicators are examined using the suite of bedrock and sediment geochemical data to determine how accurately source composition can be identified.

8.1. A–CN–K and A–CNK–FM plots

Compositional differences between average fresh bedrock and regolith are dominantly attributed to chemical weathering because regolith is generated from *in situ* weathering (Fig. 6; Taylor and Eggleton, 2001). In A–CN–K compositional space (Fig. 4B), regolith plots within the field of bedrock compositions indicating that, in this example of regolith formation, essentially no significant mineralogical changes have occurred, even though in outcrop the rock is very poorly indurated. By contrast, grus, decomposed material that essentially represents crumbled bedrock, does show initial signs of compositional departure from bedrock and more closely resembles transported sediments.

Stepladder sediments deviate from bedrock in A–CN–K (Fig. 4) and A–CNK–FM (Fig. 5) space, but not along the predicted weathering trends also shown on the diagrams. Although the data show a minor enrichment of CIA relative to bedrock (Fig. 4A), sediments scatter along either the plagioclase–K-feldspar join (Fig. 4) or feldspar–FM join (Fig. 5), which is more consistent with changes in provenance. In fact, the scatter in the data spans the equivalent compositional range between granite and granodiorite or granodiorite and diorite (Fig. 4A), even though all the sediments were derived from the same source. Figure 4E illustrates that grain size, and therefore sorting, clearly controls the where data plot: finer sediments, on average, appear as if they derive from a more mafic provenance, and coarser from a more felsic provenance. In the Stepladder system, only group *C* sediments closely resemble bedrock, although the average of most samples would likely as well. Because these plots have been used to determine provenance in ancient sediments (e.g., Fedo et al., 1995; Schoenborn and Fedo, 2011) based on systematic compositional changes developed during soil formation (e.g., Nesbitt and Markovics, 1997), caution is urged for using them for interpreting provenance in sandstones, particularly where sorting has eliminated a wide range of grain sizes.

8.2. Rare earth element plots

Sedimentary provenance studies have focused on the use and limitations of rare earth elements as provenance indicators for more than thirty years (Cullers et al., 1979; McLennan et al., 1979; Gromet and Silver, 1983; Taylor et al., 1986; Price et al., 1991; Condie et al., 1991; Singh and Rajamani, 2001; Lawrence and Kamber, 2006). Bedrock-normalized REE of the

Stepladder sediments (Fig. 10; Table 6) exhibit variable REE fractionation and negative Eu anomaly development with decreasing grain size. In general, total REE and HREE fractionation decreases with decreasing grain size (Gd_{BR}/Yb_{BR} = 0.73 for group *G* and Gd_{BR}/Yb_{BR} = 0.59 for group *F*; Fig. 11B). Light REE fractionation is the least variable (La_{BR}/Sm_{BR} ranges from 0.79 for group F to 1.01 for group *VC*) and also decreases with decreasing grain size. The strong correlation between HREE, Zr, and Hf (Table 4) suggests that these elements are hosted by zircon. Therefore, it is likely that HREE fractionation is attributed to zircon accumulation in group *M*, *F*, and *VF* sediments. This is also supported by the elevated concentrations of Zr and Hf in group *M*, *F*, and *VF* sediments relative to average bedrock (Zr ranges from 214.52 - 572.18 ppm; avg. bedrock = 170.20 ppm; Hf ranges from 6.01 - 14.31 ppm; avg. bedrock = 4.72 ppm; Table 4).

8.2.1. Eu and Ce anomalies

Typically, the REE are trivalent, and thus behave similarly. Cerium and Eu differ from other REE because they can exist in the tetravalent and divalent oxidation states, respectively. Although REE mobilization can occur during chemical weathering of bedrock, source bedrock REE signatures are preserved in the weathering profile because there is no net loss of REE abundance (Condie et al., 1991; Cullers, 1995; Compton et al., 2003; Kütterolf et al., 2008). Because of this, REE ratios (e.g. La_{CN}/Yb_{CN}, Gd_{CN}/Yb_{CN}, La_{CN}/Sm_{CN}, Eu/Eu*) of sediments are considered to resemble provenance and are commonly used to determine bulk source composition (Taylor and McLennan, 1985; Cullers, 1988; Fedo et al., 1996; Singh and Rajamani, 2001; Kütterolf et al., 2008). However, the variance among the Stepladder sediment and average bedrock REE ratios reveals that, despite the having the same source, REE compositions can

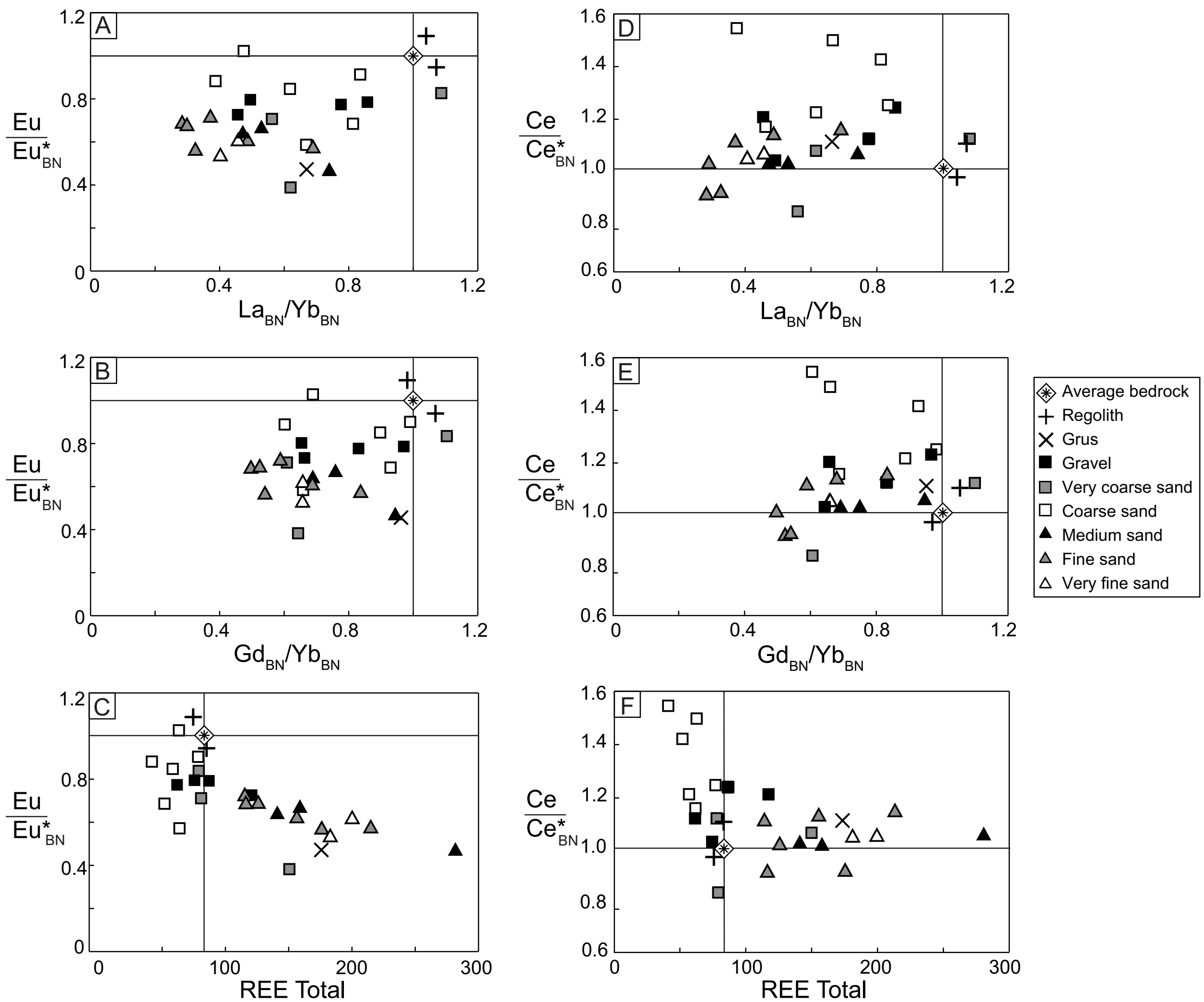

Figure 11. Bedrock-normalized Eu* and Ce* plots. Bedrock-normalized plots of Eu anomalies vs. (A) La_{BN}/Yb_{BN} (B) Gd_{BN}/Yb_{BN} and (C) REE Total. Bedrock-normalized plots of Ce anomalies vs. (D) La_{BN}/Yb_{BN} (E) Gd_{BN}/Yb_{BN} and (F) REE Total.

fluctuate during sediment production and transport. Furthermore, the reasons for REE compositional variability, most notably the development of Eu and Ce anomalies, is not always clear.

Customarily, sediment Eu/Eu* values are thought to be inherited directly from the source rock (Taylor and McLennan, 1985; Roddaz et al., 2008; Borges et al., 2008; Singh, 2010); however, in this study, the Eu/Eu* values (Fig. 11A-C) of Stepladder sediment vary considerably from bedrock (Fig. 10). Sediments have bedrock-normalized Eu/Eu* values ranging from just above 1 to as low as 0.39 (Tables 5, 6). Total REE content (Fig. 11C) and mean grain size appear to have more influence on Eu/Eu* than total percent plagioclase (Appendix 2, Fig. A2.6). The covariation between negative Eu anomalies, a decrease in grain size, and an increase in total REE (Fig. 11C) suggests the Eu-anomaly could be controlled by the accessory phases in the Stepladder sediment. Considering individual sediment samples, Eu/Eu* values differ from average parent bedrock up to a factor of 1.7 (Fig. 11A-C, Table 6). If the negative Eu-anomalies are the result of accessory mineral concentration, the Stepladder sediments indicate that hydrologic sorting, even over short transport distances, is capable of concentrating enough accessory phases to influence REE compositions and to develop negative Eu anomalies that are typically interpreted to represent more felsic, granitic rocks.

Positive bedrock-normalized Ce anomalies (Figs. 10D, 11D-F) are characteristic of group *C* sediments. While Ce anomalies are present in other samples, they are random and essentially negligible (Fig. 10; Table 6). Fractionation of Ce is known to occur during weathering and sedimentary processes (Borges, 2008). Most commonly, positive Ce anomalies develop where soluble Ce^{3+} oxidizes to the insoluble and stable Ce^{4+} (Braun et al., 1990; Pan and Stauffer, 2000). It is unlikely that redox processes, however, caused the positive Ce anomalies in the

Stepladder sediments, because other redox–sensitive elements do not show similar changes and there is no reason to restrict Ce oxidation to group *C* sediments. Conversely, the strong correlation between Ce anomalies, total REE, and grain size (Fig. 11C, F) suggest that the anomalies developed due to sorting, and therefore during transport, where hydraulic sorting concentrated Ce-rich mineral phases among the coarse-grained sediment fractions.

8.3. Trace element plots

Taylor and McLennan (1985) and Condie and Wronkiewicz (1990) stated the elemental ratios Th/Sc, Cr/Th, Th/Co and La/Sc are ideal to represent overall bulk provenance composition because, in the absence of sedimentary recycling, they are sensitive to igneous chemical differentiation processes and undergo little fractionation throughout weathering. More specifically, where hydraulic sorting of various grain sizes influences sediment composition, the ratios La/Sc and Th/Sc are useful to minimize the effect of mineral fraction (Taylor and McLennan 1985; Condie and Wronkiewicz, 1990). From the variation in elemental ratios Th/Sc, Cr/Th, Th/Co and La/Sc, studies have determined the bulk composition of the source rock (Condie et al., 1991; Fedo et al., 1996) and distinguished the provenance compositions of sediments that were derived from the mixing of multiple sources (Singh, 2010; Ghosh and Sarkar, 2010).

While previous research assumes these compatible/incompatible ratios are sensitive to average source composition, the Th/Sc vs. Sc, Cr/Th vs. Th/Sc, and Th/Co vs. La/Sc diagrams (Fig. 12) of the Stepladder sediments show these elemental ratios differ (up to a factor of 10) from their average parent bedrock composition. The extensive scatter seen in these plots is predominantly due to Th and Sc variability (Table 4). Sediment Th/Sc ratios decrease relative to average fresh bedrock because there is up to a fourfold increase in Th and tenfold increase in Sc (Fig. 12A; Table 4) with decreasing grain size.

8.3.1. Th/Sc vs. Sc (ppm)

Because Th is incompatible and Sc is relatively compatible, the elemental ratio Th/Sc is thought to be sensitive to average provenance composition (Taylor and McLennan, 1985). Figure 12A shows Th/Sc ratio plotted against concentration of Sc for all Stepladder samples. Average bedrock has a Th/Sc value of ~10 and while the Th/Sc ratios of regolith and grus are not identical to average bedrock, they plot within the Th/Sc bedrock compositional range. Within Figure 12A, however, grus does not plot near average bedrock or regolith because it is enriched in Sc. Instead, grus looks more like transported sediments, plotting near group *F* and *VF* samples (Fig. 12A).

Nearly all Stepladder sediments have Th/Sc values similar to or less than that of average bedrock. In Th/Sc vs. Sc space (Fig. 12A), data scatter away from bedrock with Th/Sc values that differ by nearly a factor of 10. Despite the sediment sourcing from the same pluton, the scatter in the data spans a compositional range greater than that between granite and TTG (Fig. 12A), and is consistent with the mixing of up to ~10 % basalt. This result challenges the traditional thought that Th/Sc ratios remain constant despite the effects of weathering and sorting. Figure 12A shows that sediment sorting has influenced the Stepladder sediments, making the finer sediment fractions, especially those of group *F* and *VF*, appear to derive from a more mafic provenance than the Stepladder granodiorite. While similar studies have reported that the Th/Sc ratio differs in bedrock and sediment that was generated in an arid climate (Cullers

Figure 12. Compatible vs. incompatible trace element plots. Mixing curves between the end-member pairs: average Stepladder granodiorite and Mesozoic-Cenozoic basalt (Condie, 1993) are plot on top of data to show compositional variation in the sediments. (A) Th/Sc vs. Sc (ppm) plot; (B) Cr/Th vs. Th/Sc plot; and (C) Th/Co vs. La/Sc plot (Gu et al., 2002). All plots include average bedrock and samples: Stepladder bedrock (2), regolith, grus, and sediment. Average Mesozoic-Cenozoic Granite and TTG (Condie, 1993) plot for reference. Percentages identify the amount of basalt in mixing model. Note that all three plots show that sediment composition is consistent with the Stepladder sediments being mixed with 10-20 % basalt.

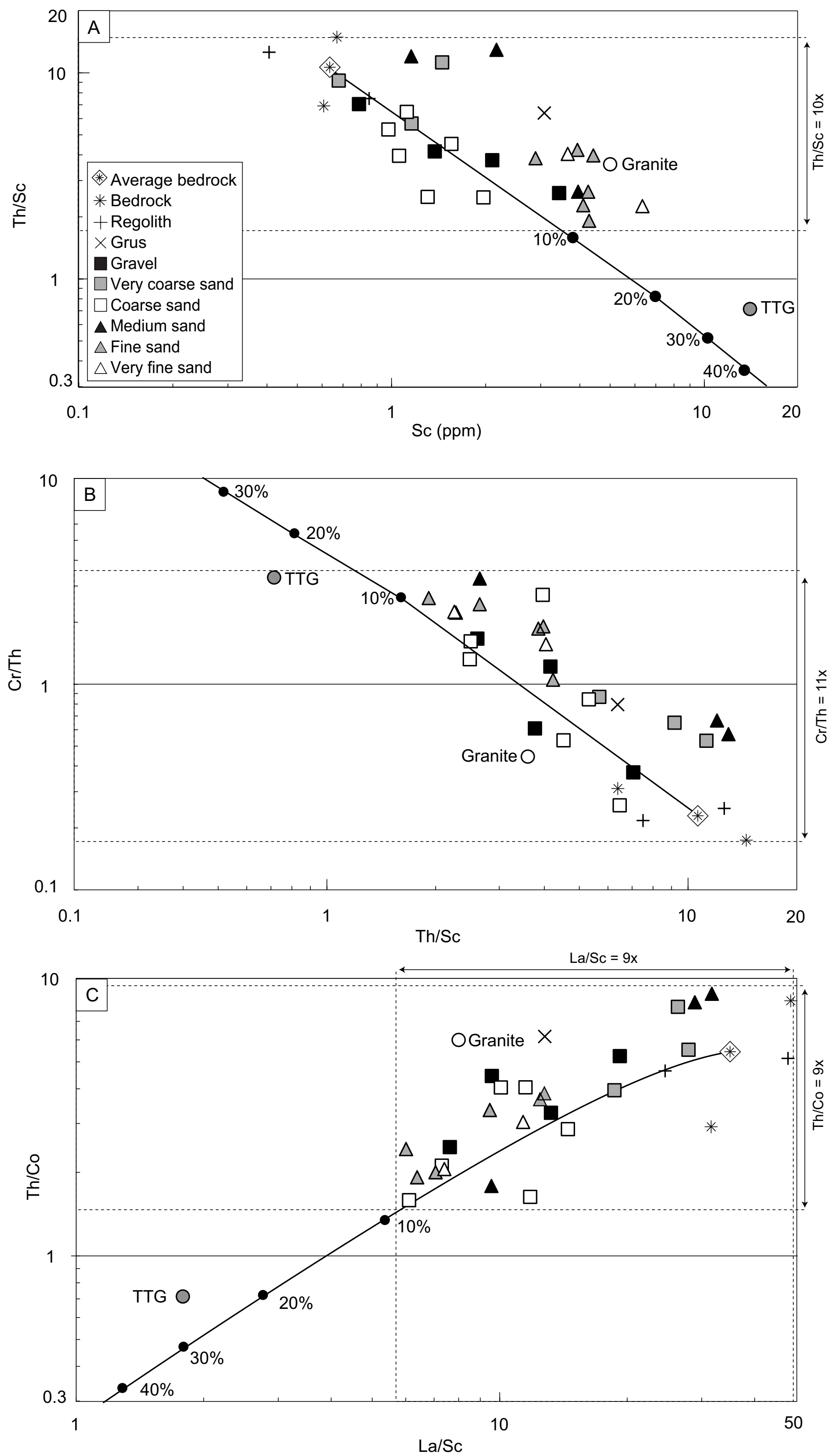

A
Th/Sc
Sc (ppm)
Average bedrock
Bedrock
Regolith
Grus
Gravel
Very coarse sand
Coarse sand
Medium sand
Fine sand
Very fine sand
Granite
TTG
10%
20%
30%
40%
Th/Sc = 10x
B
Cr/Th
Th/Sc
Cr/Th = 11x
C
Th/Co
La/Sc
La/Sc = 9x
Th/Co = 9x

et al., 1988), the Th/Sc ratio is frequently used in provenance studies to determine the provenance of various siliciclastic rocks (Fedo et al, 1996; Asiedu et al., 2004; Gonzolez-Alvarez et al., 2006; Spalletti et al., 2008). In fact, most of these studies focus on rocks that are better sorted, and therefore have experienced greater mineral fractionation, than the Stepladder sediments. The Th/Sc ratio may still provide crucial information on provenance bulk composition, but it must be known that moderate variations in the Th/Sc ratio may be due to sorting and do not necessarily indicate mixing between sources of similar composition (e.g., granite and granodiorite).

8.3.2. Cr/Th vs. Th/Sc

The scatter seen in the Cr/Th vs. Th/Sc plot (Fig. 12B) is not exclusively from the wide ranging concentrations of Th and Sc, but is also from the enrichment of Cr (up to 25x) in the fine-grained sediment fractions (especially groups *F* and *VF*). Stepladder Cr/Th ratios also show large variations, as sediment and average bedrock values differ by a factor of 10. The Cr/Th values of regolith, however, are similar to average bedrock, while the Cr/Th value of grus is slightly larger (Fig. 12B) and, again, appears more like transported sediment.

Most Stepladder sediments also have Cr/Th values that are greater than that of average bedrock and, thus, deviate from average bedrock in Cr/Th vs. Th/Sc space (Fig. 12B). With the exception of group *M* sediments, the finer grained samples (groups *F* and *VF*) have the largest Cr/Th values and are more mafic in composition than average Stepladder bedrock. Although there is some overlap with the finer sediments, the coarser grained samples (groups *G, VC,* and *C*) have lower Cr/Th values and are more similar to average bedrock. Group *M* sediments show unique characteristics in Cr/Th vs. Th/Sc space because they enclose all of the Stepladder data. As seen in the upper left quadrant of Figure 12B, one sample in group *M* plots above all data (high Cr/Th and low Th/Sc values); in the lower right quadrant of Figure 12B, the remaining two samples in group *M* plot to the right of average bedrock (low Cr/Th and high Th/Sc values). The scatter in the data is equivalent to the Stepladder sediment being mixed with up to 10 % basalt (Fig. 12B), where group *F* and *VF* sediments appear to contain more mafic components than group *VC* and select group *VC, C,* and *M* sediments, which more closely resemble average bedrock. Irregular variations in Cr distribution can be attributed to redox processes (Lopez et al., 2005), where suboxic conditions drive the oxidation of Cr(III) to Cr(VI), subsequently increasing its mobility (Middleburg et al., 1988). However, in an arid environment without persistent precipitation -- like that of the Stepladder region -- or another way to oxidize Cr, it remains locked in the solid mineral phase. Assuming redox processes are not prevalent in the arid Stepladder climate due to the lack of oxidizing agents, Cr abundances must be modified during transport and hydraulic sorting. A recent study by McGlynn et al. (in preparation), which examined trace element fractionation in physically crushed basalts, recognized the same transition metal enrichment trends identified in the Stepladder sediments (e.g., Fig. 8F), specifically the progressive enrichment of Cr and other HFSE in sediments with decreasing grain size. This supports the interpretation that Cr (and other redox-sensitive HFSE) in Stepladder sediment was influenced during transport, albeit over short distances, and sorting into various grain size fractions.

8.3.3. Th/Co vs. La/Sc

Variations in the elemental ratios Th/Co and La/Sc of Stepladder materials are also apparent through the scatter seen in Figure 12C. Similar to elemental trends described above (e.g. Fig. 12A, B), the incompatible-compatible elemental ratios Th/Co and La/Sc of regolith plot within the bedrock compositional range (Fig. 12C), while corresponding values of grus plot outside this range (Fig. 12C). Grus has a Th/Co value comparable to average bedrock and regolith, but a La/Sc value that is lower and more similar to transported sediment and the granite reference composition (Fig. 12C).

The average Th/Co and La/Sc values of each sediment grain-size group decrease relative to average bedrock, generating the majority of the scatter seen in Figure 12C. Here, the distribution of samples is similar to the distribution identified in Figure 12B where the finer grained samples plot the farthest from average bedrock and appear more mafic in composition, and the coarser grained samples plot closest to average bedrock, even though they do overlap a few fine grained samples (Fig. 12C). The scatter in the data are also equivalent to the compositional changes resulting from the mixing of Stepladder bedrock with ~10 % basalt, with group F and VF sediments being the most mafic. Like Cr, redox processes can influence the distribution of Co, but because Co is systematically enriched in the fine-grained sediment fractions, it is likely that redox is not a dominant influence on Stepladder sediment composition. The distribution of La is similar, as it is also enriched in the fine-grained sediments (e.g. Fig. 8E). Despite the increase in La abundances in fining sediment, the La/Sc ratios decrease relative to bedrock because the enrichment in Sc is significantly greater than the enrichment of La (Table 4).

It is important to identify the potential influences sorting can have on sediment compositions, most notably elemental ratios that are traditionally used to interpret provenance. Previous provenance studies (e.g., Singh, 2010) have interpreted data that show less scatter than Stepladder sediments in Th/Co vs. La/Sc space to represent the mixing of granitic and granodioritic sources. Variability in Stepladder Th/Sc, Cr/Th, Th/Co, and La/Sc ratios cannot be attributed to chemical weathering as they are in other studies (Nesbitt and Markovics, 1997;

Spalletti et al., 2008), nor can they be attributed to contributions from additional sources (Spalletti et al., 2008) because the Stepladder sediments are known to source from a single pluton from an arid environment.

8.3.4. Cr (ppm) vs. Ni (ppm)

Bolhar et al. (2005) interpreted the large ranges in transition metal abundances and strong correlation between Cr and Ni in Archean metasedimentary rocks from Greenland to represent mixing between two sources. Similar Cr - Ni relationships are seen among the Stepladder sediments (Fig. 13A). A two-component mixing-model with end-members of Stepladder granodiorite and basalt are consistent with up to ~20 % basalt being mixed with the Stepladder source. Despite the strong covariation and large range in Cr and Ni abundances, the compositional variations within the Stepladder sediments cannot be attributed to source mixing.

8.3.5. Cr/V vs. Y/Ni

Diskin et al. (2010) investigated mudstones and siltstones from a passive margin setting to see if sediments with subtly different provenances could be recognized. They ascribed the variations in Cr/V and Y/Ni to provenance variations and the mixing of felsic and mafic sources. Stepladder Cr/V ratios (Fig. 13B) are fairly restricted (range from 0.1 - 0.7; Table 8), indicating Cr is not enriched over other ferromagnesian trace elements. However, the Y/Ni values are more variable (range from ~1 - 7.5; Fig. 13B; Table 8), showing the enrichment of Y (proxy for HREEs; Diskin et al., 2010; McLennan et al., 1993) over Ni, another ferromagnesian trace element. Sediments do not fall on the mixing curve (Fig. 13B) as well as they do in the previous plots, however they do scatter along a roughly similar trend, consistent with mixing of a mafic end member.

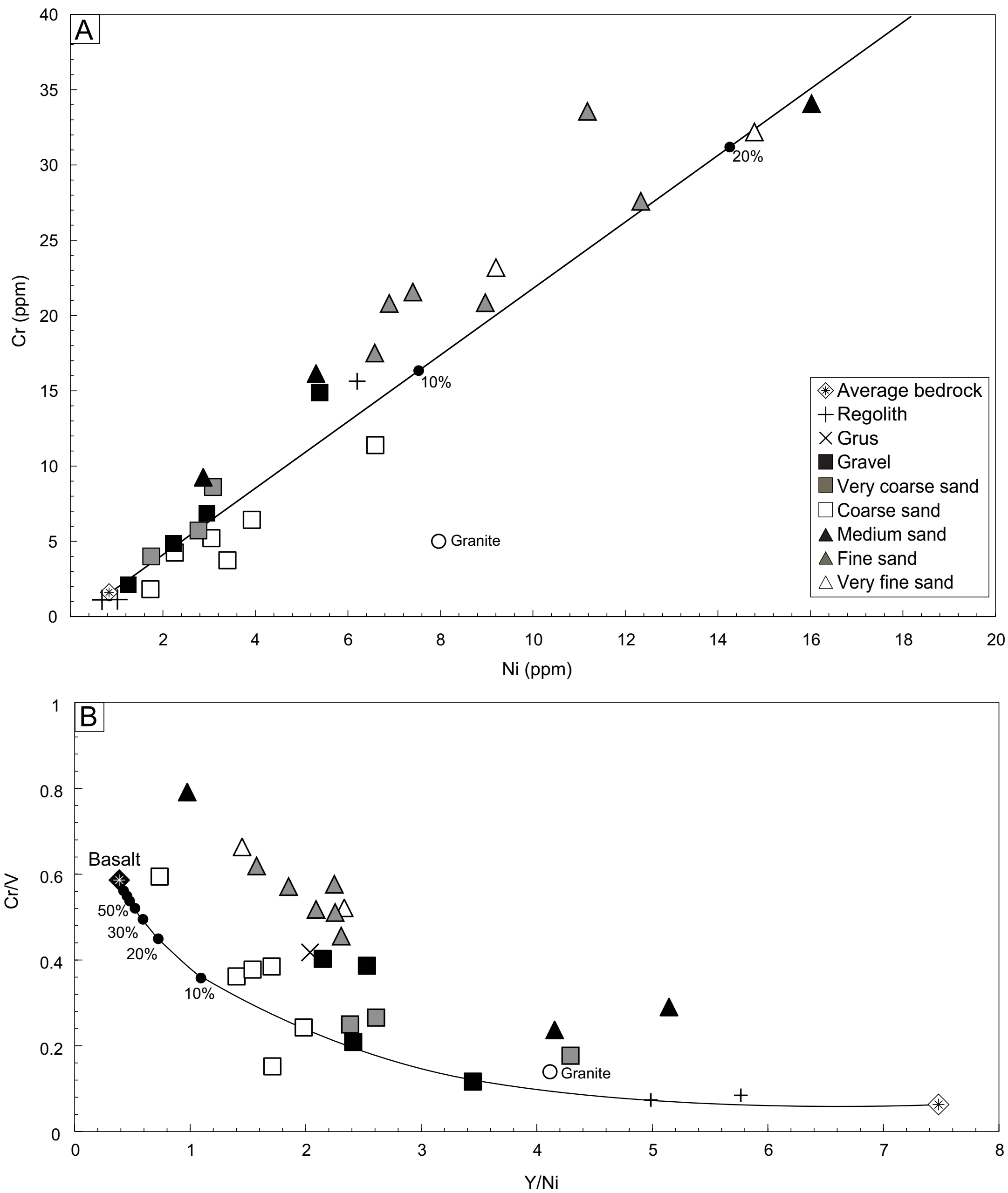

Figure 13. High field strength element plots and mixing curves between end-member pairs of average Stepladder granodiorite and Mesozoic-Cenozoic basalt (Condie, 1993). Plots of (A) Cr (ppm) vs. Ni (ppm) (after Taylor and McLennan, 1985), and (B) Cr/V vs. Y/Ni (after McLennan et al., 1993). Plots include average Stepladder bedrock, regolith, grus, and sediments. Average Mesozoic-Cenozoic Granite and TTG (Condie, 1993) plot for reference.

8.4. Utility of diagrams and indicators

The ability for provenance-seeking indicators to accurately identify provenance source and sedimentary processes that influence sediment composition, such as weathering and sorting, are paramount to provenance research. Plots using the major elements to measure the degree of chemical weathering are able to illustrate the lack of chemical weathering, and when the ferromagnesian components are considered, are able to distinguish the importance of sorting. In the most general terms, most of the elemental ratio plots correctly distinguished the Stepladder source composition as a felsic to intermediate rock, but they do not identify the known bedrock composition. Variations in REE and other elemental ratios, however, are large considering the sediments have been transported less than 7 km and are derived from a single source. While the ranges of the ratios may not suggest these sediments are extremely well sorted or have been recycled, they do indicate that only a minor degree of sorting is capable of modifying sediment compositions considerably from that of its source. It should also be noted that the large range in the REE and elemental ratios is not indicative of multiple sources and sediment mixing.

9. Factors influencing compositional changes

9.1. Chemical and physical weathering

Clastic sediment derived from the Stepladder granodiorite is generated through both chemical and physical weathering processes. A minimal amount of chemical weathering produced regolith and grus. Subsequent physical disaggregation, mostly from high-energy rain events, removed rock fragments and individual mineral grains from the bedrock surface and dispersed the material down slope. How a mineral is mechanically broken down is greatly influenced by its stability and crystal structure. Albeit minor, plagioclase is the most readily weathered phase (Nesbitt et al., 1980) in the Stepladder sediments, allowing larger portions of these grains to be converted to clays (along cleavage planes and Ca-rich zones; Fig. 6) than in K-feldspar. Even though the Stepladder granodiorite has experienced a minimal degree of chemical weathering, it is significant enough to promote grain disintegration along cleavage planes as indicated by the enrichment in plagioclase with decrease in grain size (Table 2). Quartz and K-feldspar, which are less readily weathered (Nesbitt and Young, 1984), do not break down to fine sizes as easily as plagioclase, and as a result, they tend to concentrate in the larger grain-size fractions (Fig. 9). Conversely, biotite preferentially breaks down into smaller grains, not only because it is readily weathered (Nesbitt et al., 1980), but also because of its cleavable crystal structure (Cullers et al., 1988; Nesbitt et al., 1996).

Because the climate limits the intensity of chemical weathering, the tendency for a mineral to be weathered and broken into fragments greatly influences the composition of sediment. However, specific climate settings under which sediments formed may not be identifiable from geochemistry alone. Both the Stepladder sediments and the Guys Bight sediments (Nesbitt and Markovics, 1996) exhibit similar trends in A–CN–K and A–CNK–FM composition space (Figs. 5, 6), even though one formed in an arid environment and the other in a glacial setting.

9.2. Sediment transport and sorting

Because sediment compositions do not represent chemical weathering or source mixing, sorting processes are likely responsible for the major compositional fractionations among the Stepladder samples. During transport, hydrodynamic sorting physically fractionates detritus based on shape, size, and density, and generating very poorly sorted sediment, with distinct grain size groupings. Even though the distance of sediment transport is short (maximum 10 km), it is far enough for sorting to influence the modal mineralogy and the chemical composition of the Stepladder sediments, as has been demonstrated as far back as at least the 1950s (McEwen et al., 1959).

Not only did sediment sorting have a significant effect on trace element abundances, it also generated variable elemental ratios. Individual analysis of the three samples with Th/Co > 7 (Fig. 12C) revealed that they are anomalously enriched in Th and La relative to Co and Sc (Table 4). Petrographic inspection of these sediment samples shows they are significantly concentrated in apatite, titanite, and opaques oxides, suggesting these accessory phases are preferentially concentrated during hydraulic sorting (Cullers, 1988; Condie and Wronkiewicz, 1990; Singh and Rajamani, 2001), and likely account for the Th and La enrichment. Much like the compositional fractionation seen among the major oxides, the elemental ratios (thought to be source-rock indicators) Th/Sc, Cr/Th, Th/Co, and La/Sc, instead prove to be sensitive to sediment sorting that occurs during transportation, even over short distances (< 10 km).

Discrimination diagrams designed to identify sorting, as well as sedimentary recycling and mineral enrichment, were used to further explore the compositional effects sorting had on the Stepladder sediments. These diagrams focus on a few select elements (Al, Ti, Zr, Hf, Th, Sc, and La) because of their low solubility in liquid water and their tendency to be relatively immobile elements (Cullers, 1988; Condie and Wronkiewicz, 1990). Elemental ratios, including Ti:Al, can be a useful signature to identify provenance, but because of their durability (Young and Nesbitt, 1998; McLennan, 2001), Ti:Al ratios are sensitive to sedimentary fractionations (Garcia et al., 1994; Bonjour and Dabard, 1991). Because TiO_2 predominately resides in biotite and ilmenite and Al_2O_3 in feldspars and biotite, the effects of sorting will modify the Ti:Al ratio as the fine, mafic-enriched sediments are concentrated (Johnsson, 1993; Young and Nesbitt, 1998). Stepladder sediments do not maintain a constant Ti:Al ratio and vary from the Ti:Al of average bedrock. The variable ratios suggest that physical weathering and subsequent sorting are likely the dominant processes modifying sediment composition. While the values are variable, there is no apparent concentration of TiO_2 (or Al_2O_3) in any particular grain-size fraction. The lack of correlation of Ti with grain size may be a result of the poorly sorted sediments and the inclusion of Ti-rich phases (ilmenite, biotite, and titanite) in rock fragments and coarse sediments.

Similar to Al and Ti, the elements Zr and Hf, which are preferentially hosted by zircon, are inert, making them immobile during weathering and able to withstand multiple sedimentary rock cycles. Garcia et al. (1994) suggested the Al–Ti–Zr ternary diagram (Fig. 14A) could identify the influence of sediment recycling and sorting processes assuming a wide range of TiO_2–Zr is indicative of extensive sorting and high compositional maturity. According to the extensive scatter in Figure 14A, the Stepladder sediments appear to be well sorted and compositionally mature. The reasons for the wide range in Stepladder TiO_2–Zr are not entirely clear. One explanation for the fractionation between Ti and Zr may be from the concentration of zircon in the finer grain-size fractions (groups *VF* and *F*) and Ti-rich phases in the coarser grain-size fractions (groups *G, VC,* and *C)*. While petrographic observations revealed the presence of zircon and ilmenite in the sediments, the fine-grained texture of the phases prevented meaningful modal estimates.

The plot Th/Sc versus Zr/Sc (Fig. 14B) is another common indicator that is used to identify sediment recycling as well as zircon concentration (Willan, 2003; Rahman and Suzuki, 2007; Kutterolf et al., 2008; Spalletti, 2008; Diskin et al., 2010; Hossain et al., 2010). Both Th/Sc and Zr/Sc ratios increase proportionately with enhanced igneous differentiation (ratios are greater in increasingly more felsic rocks). Because Th/Sc is assumed to remain constant throughout weathering, sorting, and diagenesis, its value is considered to represent original igneous/source composition. As a result, an increase in Zr/Sc with little to no change in Th/Sc (i.e., the increase in Zr/Sc is not the result of igneous fractionation because Th/Sc remains constant) occurs from the enrichment and accumulation of zircon, presumably through sediment recycling and sorting. Figure 14C details two trends that may be interpreted in the Stepladder data. Because the Zr/Sc ratios increase, as the Th/Sc ratios remain relatively constant, group *C* sediments form a near-horizontal trend that is typically indicative of sediment recycling. The group *C* sediments are cut by a more steeply dipping line, which represents the remaining sediment groups. Without knowing provenance Th/Sc and Zr/Sc values, Stepladder sediments appear to represent the mixing of two sources, where one source appears to have concentrated zircon through sediment recycling. Knowledge of source rock composition, however, challenges this interpretation. Sediment Th/Sc and Zr/Sc values decrease relative to those of average bedrock, indicating either the loss of Th and Zr or the accumulation of Sc. For the Stepladder sediment, it is apparent there is no removal of Th nor Zr, in fact, both become enriched (up to three times bedrock) with the production and sorting of sediment. On the other hand, Sc is significantly depleted in fresh bedrock, in turn, increasing the provenance Th/Sc and Zr/Sc values. The concentration of ferromagnesian minerals, such as biotite, results from the hydraulic sorting or sediments. Because Sc is a trace element in biotite, it accumulates in the fine sediments (group *M*, *F*, and *VF*) (along with Ti and Zr) resulting in increased concentrations of Sc in the samples.

The plot La/Th versus Hf (Fig. 14D) may be used as a provenance plot to distinguish bulk source rock, but it also recognizes increasingly older, or recycled, sources (Kütterolf et al., 2008). All three elements La, Th, and Hf are incompatible elements, ultimately concentrating in the residual melt after magma differentiation/fractionation. Because Th is slightly more compatible (and as a result, generally more abundant than La) a felsic source is characterized by low La/Th values (i.e. ~2-4). Comparatively, moderate to high values (> 6) denote a mixed or

Figure 14. . Discrimination diagrams typically used to recognize sorting and sediment recycling. (A) Zr – Al_2O_3 (x15) – TiO_2 (x300) ternary diagram used to measure the degree of sorting and compositional maturity of sediments (Garcia et al., 1994). Data that spreads over the full length of the arrow suggests sediment has been sorted and is compositionally mature. (B) Plot of Th/Sc vs. Zr/Sc used to recognize recycled sedimentary sources and zircon concentration (after McLennan et al., 1993). (C) Detail of gray box in (B); note the near-horizontal trend of group *C* sediments consistent with sediment recycling. (D) Plot of La/Th vs. Hf (ppm) used to identify source areas of clastic sediments and increasing older (or recycled) components (Floyd and Leveridge, 1987). All plots include average Stepladder bedrock, regolith, grus, and sediment compositions. Average Mesozoic-Cenozoic Granite and TTG (Condie, 1993) plot for reference.

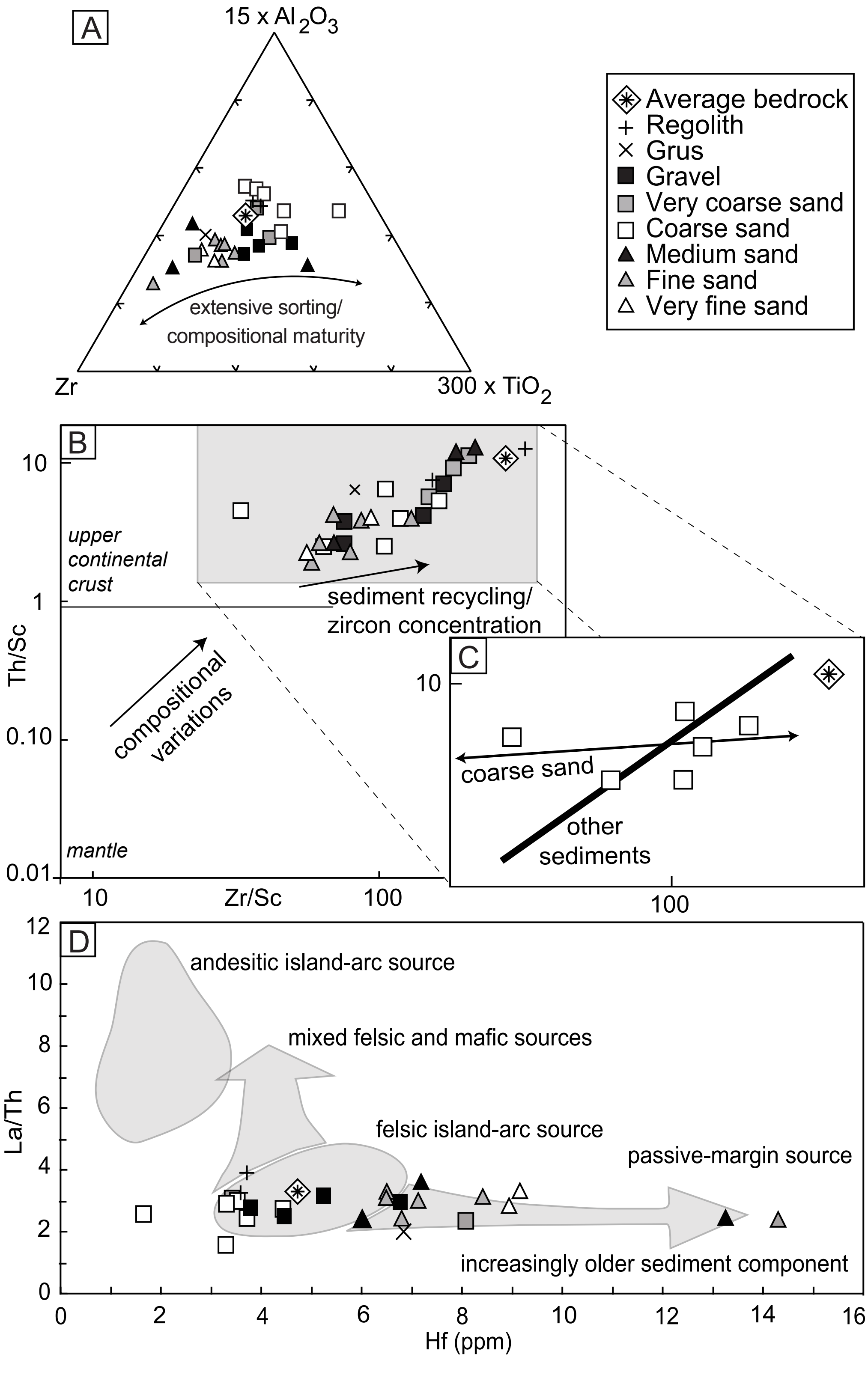
A
15 x Al2O3
Zr
300 x TiO2
extensive sorting/
compositional maturity
Average bedrock
Regolith
Grus
Gravel
Very coarse sand
Coarse sand
Medium sand
Fine sand
Very fine sand
B
10
1
0.10
0.01
Th/Sc
upper
continental
crust
mantle
compositional
variations
sediment recycling/
zircon concentration
10
Zr/Sc
100
C
10
coarse sand
other
sediments
100
D
12
10
8
6
4
2
0
La/Th
andesitic island-arc source
mixed felsic and mafic sources
felsic island-arc source
passive-margin source
increasingly older sediment component
0
2
4
6
8
10
12
14
16
Hf (ppm)

mafic source. Here, Hf acts as an indicator for sorting and/or sediment recycling as it is assumed that elevated concentrations (> 8 ppm) arise from multiple successions of sediment recycling and the fractionation of sediments through hydraulic sorting. The low La/Th values of Stepladder materials accurately identify a felsic source; however the discrimination zones based on Hf concentrations incorrectly identify about 1/4 of the sediments to represent increasingly older sediment components.

10. Conclusions

First-cycle clastic sediment sourced from the granodioritic Stepladder pluton is generated in an arid environment. The degree of chemical weathering influencing compositional changes in Stepladder samples is negligible and is supported by low CIA values (< 53). Any significant compositional differences that exist among the sediments and average bedrock, therefore, resulted during sediment transport.

Each sediment sample fell into one of six groups as determined by mean grain size distribution. Every sediment sample, despite mean grain size, comprised the same mineralogy as average bedrock, which consists of plagioclase, K-feldspar, quartz, and biotite. Modal mineralogy of the samples did vary. Regolith and group *C* sediments have a modal mineralogy comparable to fresh bedrock, where as group *G* and *VC* sediments are relatively enriched in quartz, and group *M* to *VF* sediments are relatively enriched in plagioclase and biotite.

Major element composition of fresh bedrock and regolith are similar, but, in A–CN–K space, grus and the sediments scatter throughout the granite-granodiorite-diorite composition zone. Fractionation of FeO and MgO from the major oxides Al_2O_3, CaO, Na_2O, and K_2O occurs during sediment transport as hydrodynamic sorting of the sediment concentrates biotite and heavy accessory minerals in group *M* to *VF* sediments. Rare earth elements patterns of the samples are roughly similar in shape and total REE increases with decreasing grain-size. The development of negative Eu anomalies and positive Ce anomalies are notable, although not easily explained.

Samples in group *M* best represent fresh Stepladder bedrock compared to other grain size fractions. Despite the similarity between sediments in group *C* and the bedrock source, they are the only group that appears to have experienced sedimentary recycling and extreme sorting.

Trace element ratios commonly used to distinguish source bedrock, are able to distinguish the evolved nature of the granodiorite source; however, sediments ratios differ from bedrock by a factor of 10. This noticeable variation in elemental ratios is significant because it is the result of sediment sorting. While large variations in elemental ratios have previously been interpreted to represent the mixing of multiple sources, all sediments examined here are derived from one source. Thus, any compositional modifications observed among the bedrock and sediments are the result of weathering and sorting and cannot be attributed to sediment mixing.

Geochemical signatures from the elements Al, Ti, Zr, and Hf, indicate that select sediment samples follow trends that are traditionally interpreted to represent extensive sorting and the recycling of sediment. The major factor modifying sediment composition is sorting associated with the transport and deposition of the sediment. This research indicates that the minor amounts of chemical weathering and the process of transporting and sorting sediments, even less than 10 km, has the ability to modify the geochemistry of sediments enough to where they no longer retain their original provenance signatures.

References

Anderson, J.L., Cullers, R.L., 1990. Middle to upper crustal plutonic construction of a magmatic arc; An example from the Whipple Mountains metamorphic core complex, In: Anderson, J. (Ed.), The nature and origin of Cordilleran magmatism: Boulder, Colorado, Geological Society of America Memoir 174, pp. 47–69.

Armstrong-Altrin, J.S., Verma, S.P., 2005. Critical evaluation of six tectonic setting discrimination diagrams using geochemical data of Neogene sediments from known tectonic settings. Sedimentary Geology 177, 115–129.

Basu, A.R., 1976. Petrology of Holocene fluvial sand derived from plutonic source rocks; implications to paleoclimatic interpretation. Journal of Sedimentary Research 46, 694–709.

Basu, A., Blanchard, D.P., Brannon, J.C., 1982. Rare earth elements in the sedimentary cycle: a pilot study of the first leg. Sedimentology 29, 737-742.

Basu, A.R., Sharma, M., DeCelles, P.G., 1990. Nd, Sr-isotopic provenance and trace element geo- chemistry of Amazonian foreland basin fluvial sands, Bolivia and Peru: Implications for ensialic Andean orogeny. Earth and Planetary Science Letters 100, 1–17.

Basu, A.R., Young, S.W., Suttner, L.J., James, W.C., Mack, G.H., 1975. Re-evaluation of the use of undulatory extinction and polycrystallinity in detrital quartz for provenance interpretation. Journal of Sedimentary Research 45, 873–882.

Bolhar, R., Kamber, B.S., Moorbath, S., Whitehouse, M.J., Collerson, K.D., 2005. Chemical characterization of earth’s most ancient clastic metasediments from the Isua greenstone belt, southern West Greenland. Geochimica et Cosmochimica Acta 69, 1555–1573.

Bonjour, J.L., Dabard, M.P., 1991. Ti/Nb ratios of clastic terrigenous sediments used as an indicator of provenance. Chemical Geology 91, 257–267.

Borges, J.B., Huh, Y., Moon, S., Noh, H., 2008. Provenance and weathering control on river bed sediments of the eastern Tibetan plateau and the Russian far east. Chemical Geology 254, 52–72.

Braun, J.J., Pagel, M., Muller, J.P., Bilong, P., Michard, A. Guillet, B., 1990. Cerium anomalies in lateritic profiles. Geochimica et Cosmochimica Acta, 54: 781-795.

Buss, H.l., Sak, P.B., Webb, S.M., Brantley, S.L., 2008. Weathering of the Rio Blanco quartz diorite, Luquillo Mountains, Puerto Rico: Coupling oxidation, dissolution, and fracturing. Geochimica et Cosmochimica Acta 72, 4488–4507.

Compton, J.S., White, R.A., Smith, M., 2003. Rare earth element behavior in soils and salt pan sediments of a semi-arid granitic terrain in the Western Cape, South Africa. Chemical Geology 201, 239–255.

Condie, K.C., 1993. Chemical composition and evolution of the upper continental crust: Contrasting results from surface samples and shales. Chemical Geology 104, 1–37.

Condie, K.C., Wilks, M., Rosen, D.,M. Zlobin, V.L., 1991. Geochemistry of metasediments from the Precambrian Hapschan series, eastern Anabar Shield, Siberia. Precambrian Research 50, 37– 47.

Condie, K.C., Wronkiewicz, D.J., 1990. The Cr/Th ratio in Precambrian pelites from the Kaapvaal Craton as an index of craton evolution. Earth and Planetary Science Letters 97, 256–267.

Cullers, R.L., 1988. Mineralogical and chemical changes of soil and stream sediment formed by intense weathering of the Danburg granite, Georgia, U.S.A. Lithos 21, 301–314.

Cullers, R.L., Basu, A., Suttner, L.J., 1988. Geochemical signature of provenance in sand-size material in soils and stream sediments near the Tobacco Root Batholith, Montana, U.S.A. Chemical Geology 70, 335-348.

Cullers, R.L., 1995. The controls on the major- and trace-element evolution of shales, siltstones and sandstones of Ordovician to Tertiary age in the Wet Mountains region, Colorado, U.S.A. Chemical Geology 123, 107–134.

Cullers, R.L., 2002. Implications of elemental concentrations for provenance, redox conditions, and metamorphic studies of shales and limestones near Pueblo, CO, USA. Chemical Geology 191, 305–327.

Cullers, R.L., Chaudhuri, S., Kilbane, N., Koch, R., 1979. Rare-earths in size fractions and sedimentary rocks of Pennsylvanian-Permian age from the mid-continent of the U.S.A. Geochimica et Cosmochimica Acta 43, 1285–1301.

Delvigne, J., 1998, Atlas of Micromorphology of Mineral Alteration and Weathering, Mineralogical Association of Canada.

Dickinson, W.R., 1970. Interpreting detrital modes of graywacke and arkose. Journal of Sedimentary Petrology 40, 695–707.

Dickinson, W.R., Beard, L.S., Brakenridge, G.R., Erjavec, J.L., Ferguson, R.C., Inman, K.F., Knepp, R.A., Lindberg, F.A., Ryberg, P.T., 1983. Provenance of North American Phanerozoic sandstones in relation to tectonic setting. Geological Society of American Bulletin 94, 222–235.

Dickinson, W.R., Suczek, C.A., 1979. Plate tectonics and sandstone compositions. The American Association of Petroleum Geologists Bulletin 63, 2164–2182.

Dinelli, E., Lucchini, F., Mordenti, A., Paganelli, L., 1999. Geochemistry of Oligocene - Miocene sandstones of the northern Apennines (Italy) and evolution of chemical features in relation to provenance changes. Sedimentary Geology 127, 193-207.

Diskin, S., Evans, J., Fowler, M.B., Guion, P.D., 2010. Recognizing different sediment provenances within a passive margin setting: Towards characterizing a sediment source to the west of the British Upper Carboniferous sedimentary basins. Chemical Geology doi: 10.1016/j.chemgeo.2010.10.007.

Dokuz, A., Tanyolu, E., 2006. Geochemical constraints on the provenance, mineral sorting, and subaerial weathering of lower Jurassic and upper Cretaceous clastic rocks of the eastern Pontides, Yusufeli (Artvin), NE Turkey. Turkish Journal of Earth Sciences 15, 181–209.

Dorozhkin, S.V., 2002. A review on the dissolution models of calcium apatites. Progress in Crystal Growth and Characterization of Materials 44, 45-61.

Eggins, S.M., Woodhead, J.D., Kinsley, L.P.J., Mortimer, G.E., Sylvester, P., McCulloch, M.T., Hergt, J.M., Handler, M.R., 1997. A simple method for the precise determination of >40 trace elements in geological samples by ICPMS using enriched isotope internal standardization. Chemical Geology 134, 311–326.

Fedo, C.M., Eriksson, K.A., Krogstad, E.J., 1996. Geochemistry of shales from the Archean (~3.0 Ga) Buhwa greenstone belt, Zimbabwe: Implications for provenance and source-area weathering. Geochimica et Cosmochimica Acta 60, 1751–1763.

Fedo, C.M., Nesbitt, W.H., Young, G.M., 1995. Unraveling the effects of potassium metasomatism in sedimentary rocks and paleosols, with implications for paleoweathering conditions and provenance. Geology 23, 921–924.

Fedo, C.M., Young, C.M., Nesbitt, H.W., Hanchar, J.M., 1997. Potassic and sodic metasomatism in the Southern Province of the Canadian Shield: Evidence from the Paleoproterozoic Serpent Formation, Huronian Supergroup, Canada. Precambrian Research 84, 17-36.

Fletcher, J.M., Karlstrom, K.E., 1990. Late Cretaceous Ductile Deformation, Metamorphism, and Plutonism in the Piute Mountains, Eastern Mojave Desert. Journal of Geophysical Research 95, 487–500.

Floyd, P.A., Leveridge, B.E., 1987. Tectonic environment of the Devonian Gramscatho Basin, South Cornwall; framework mode and geochemical evidence from turbitic sandstones. Journal of the Geological Society of London 144, 531-542.

Folk, R.L., 1955. Student operator error in determination of roundness, sphericity, and grain size. Journal of Sedimentary Petrology 25, 297–301.

Folk, R.L., 1974. Petrology of sedimentary rocks. Austin TX: Hemphill's.

Foster, D.A., Harrison, T.M., Miller, C.F., Howard, K.A., 1990. The 40Ar/39Ar Thermochronology of the Eastern Mojave Desert, California, and Adjacent Western Arizona with Implications for the Evolution of Metamorphic Core Complexes. Journal of Geophysical Research 95, 20005– 20024.

Fralick, P.W., 2003. Geochemistry of clastic sedimentary rocks: ratio techniques, In Lentz, D. (Ed.), Geochemistry of Sediments and Sedimentary Rocks: Evolutionary Considerations to Mineral Deposit-Forming Environments, pp. 85–103.

Fralick, P.W., Kronberg, B.I., 1997. Geochemical discrimination of clastic sedimentary rock sources. Sedimentary Geology 113, 111-124.

Fuenlabrada, J.M., Arenas, R., Martinez, S.S., Garcia, F.D., Castineiras, P., 2010. A peri-Gondwanan arc in NW Iberia I: Isotopic and geochemical constraints on the origin of the arc - A sedimentary approach. Gondwana Research 17, 338-351.

Garcia, D., Fonteilles, M., Moutte, J., 1994. Sedimentary fractionation between Al, Ti, and Zr and the genesis of strongly peraluminous granites. Journal of Geology 102, 411–422.

Ghosh, S., Sarkar, S., 2010. Geochemistry of Permo-Triassic mudstone of the Satpura Gondwana basin, central India: Clues for provenance. Chemical Geology 277, 78 – 100.

Girty, G.H., March, J., Meltzner, A., McConnell, J.R., Nygren, D., Nygren, J., Prince, G.M., Randall, K., Johnson, D., Heitman, B., Nielsen, J., 2003. Assessing changes in elemental mass as a result of chemical weathering of granodiorite in a Mediterranean (hot summer) climate. Journal of Sedimentary Research 73, 424-443.

Gonzolez-Alvarez, I., Kusiak, M. A., Kerrich, R., 2006. A trace element and chemical Th-U total Pb dating study in the lower Belt-Purcell Supergroup, Western North America: Provenance and diagenetic implications. Chemical Geology 230, 140-160.

Graham, R., Rossi, A., Hubbert, K., 2010. Rock to regolith conversion: Producing hospitable substrates for terrestrial ecosystems. GSA Today 20, 4-9.

Gromet, L.P., Silver, L.T., 1983. Rare earth element distributions among minerals in a granodiorite and their petrogenetic implications. Geochimica et Cosmochimica Acta 47, 925–939.

Gu, X.X., Liu, J.M., Zheng, M.H., Tang, J.X., Qi, L., 2002. Provenance and tectonic setting of the Proterozoic turbidites in Hunan, South China: Geochemical evidence. Journal of Sedimentary Research 72, 393–407.

Gupta, K.D., Pickering, K.T., 2008. Petrography and temporal changes in petrofacies of deep-marine Ainsa-Jaca basin sandstone systems, Early and Middle Eocene, Spanish Pyrenees. Sedimentology 55, 1083–1114.

Haughton, P.D.W., Todd, S.P., Morton, A.C., 1991. Sedimentary provenance studies. Geological Society, London, Special Publications 57, 1–11.

Hessler, A.M., 2001. Evidence for climate and weathering in siliciclastic sedimentary rocks of the 3.2 Ga Moodies Group, Baberton greenstone belt, South Africa. Ph.D. dissertation. Stanford University.

Hileman, G.E., Miller, C.F., Knoll, M.A., 1990. Mid-Tertiary Structural Evolution of the Old Woman Mountains Area: Implications for Crustal Extension Across Southeastern California. Journal of Geophysical Research 95, 581–597.

Hossain, H.M.Z., Roser, B.P., Kimura, J.I., 2010. Petrography and whole-rock geochemistry of the Tertiary Sylhet succession, northeastern Bengal Basin, Bangladesh: Provenance and source area weathering. Sedimentary Geology 228, 171-183.

Huffman, E.W., Stuber, H.A., 1985. Analytical methodology for elemental analysis of humic substances. In Humic substances in soil, sediment, and water: geochemistry, isolation, and characterization. John Wiley & Sons, New York, NY, United States. . p. 433.

Ingersoll, R.V., Bullard, T.F., Ford, R.L., Grimm, J.P., Pickle, J.D., Sares, S.W., 1984. The effect of grain size on detrital modes: a test of the Gazzi-Dickinson point-counting method. Journal of Sedimentary Petrology 54, 0103–0116.

John, B.E., Foster, D.A., 1993. Structural and thermal constraints on the initiation angle of detachment faulting in the southern Basin and Range: The Chemehuevi Mountains case study. Geological Society of American Bulletin 105, 1091–1108.

John, B.E., Wooden, J., 1990. Petrology and geochemistry of the metaluminous to peraluminous Chemehuevi Mountains Plutonic Suite, southeastern California, In: Anderson, J. (Ed.), The nature and origin of Cordilleran magmatism: Boulder, Colorado, Geological Society of America Memoir 174, pp. 71–98.

Johnsson, M.J., 1993. The system controlling the composition of clastic sediments, In: Johnsson, M., Basu, A. (Eds.), Processes Controlling the Composition of Clastic Sediments: Boulder, Colorado. Geological Society of America Special Paper 284, p. 1-19.

Kamber, B.S., 2009. Geochemical fingerprinting: 40 years of analytical development and real world applications. Applied Geochemistry 24, 1074–1086.

Kamber, B.S., Greig, A., Schoenberg, R., Collerson, K.D., 2003. A refined solution to Earth's hidden niobium: implications for evolution of continental crust and depth of core formation. Precambrian Research 126, 289–308.

Karlstrom, K.E., Miller, C.F., Kingsbury, J.A., Wooden, J.L., 1993. Pluton emplacement along an active ductile thrust zone, Piute Mountains, southeastern California: Interaction between deformational and solidification process. Geological Society of American Bulletin 105, 213–230.

Kingsbury, J.A., Miller, C.F., Wooden, J.L., Harrison, T.M., 1993. Monazite paragenesis and U-Pb systematics in rocks of the eastern Mojave Desert, California, U.S.A.: implications for thermochronometry. Chemical Geology 110, 147–167.

Kütterolf, S., Diener, R., Schacht, U., Krawinkel, H., 2008. Provenance of the Carboniferous Hochwipfel Formation (Karawanken Mountains, Austria/Slovenia) - Geochemistry versus petrography. Sedimentary Geology 203, 246–266.

Lawrence, M.G., Kamber, B.S., 2006. The behavior of the rare earth elements during estuarine mixing – revisited. Marine Chemistry 100, 147–161.

Lopez, J.M.G., Bauluz, B., Fernandez-Nieto, C., Oliete, A.Y., 2005. Factors controlling the trace-element distribution in fine-grained rocks: the Albian kaolinite-rich deposits of the Oliete Basin (NE Spain). Chemical Geology 214, 1-19.

Mack, G.H., 1984. Exceptions to the relationship between plate tectonics and sandstone composition. Journal of Sedimentary Petrology 54, 212-220.

McCaffrey, K.J.W., Miller, C.F., Karlstrom, K.E., Simpson, C., 1999. Synmagmatic deformation patterns in the Old Woman Mountains, SE California. Journal of Structural Geology 21, 335–349.

McDonough, W.F., Sun, S.S., 1995. The composition of the Earth. Chemical Geology 120, 223–253.

McEwen, M.C., Fessenden, F.W., Rogers, J.J.W., 1959. Texture and composition of some weathered granites and slightly transported arkosic sands: Texas and Colorado. Journal of Sedimentary Petrology 29, 477–492.

McLennan, S.M., 1989. Rare earth elements in sedimentary rocks: Influence of provenance and sedimentary processes. Mineralogical Society of America Reviews in Mineralogy 21, 169–200.

McLennan, S.M., Taylor, S.R., McCulloch, M.T., Maynard, J., 1990. Geochemical and Nd- Sr-Isotopic composition of deep sea turbidites: Crustal evolution and plate tectonics association. Geochimica et Cosmochimica Acta 54, 2015-2050.

McLennan, S.M., 2001. Relationship between the trace element composition of sedimentary rocks and upper continental crust. Geochemistry, Geophysics, Geosystems 2.

McLennan, S.M., Fryer, B.J., Young, G.M., 1979. Rare earth elements in Huronian (Lower Proterozoic) sedimentary rocks: composition and evolution of the post-Kenoran upper crust. Geochimica et Cosmochimica Acta 43, 375–388.

McLennan, S.M., Hemming, S., McDaniel, D.K., Hanson, G.N., 1993. Geochemical approaches to sedimentation, provenance, and tectonics, In: Johnsson, M., Basu, A. (Eds.), Processes Controlling the Composition of Clastic Sediments: Boulder, Colorado, pp. 621–624.

McLennan, S.M., Taylor, S.R., 1991. Sedimentary rocks and crustal evolution: tectonic setting and secular trends. Journal of Geology 99, 1–21.

McLennan, S.M., Taylor, S.R. and Hemming, S.R., 2006. Composition, differentiation, and evolution of continental crust: Constraints from sedimentary rocks and heat flow. In: M. Brown and T. Rushmer, (Eds.) Evolution and Differentiation of the Continental Crust. Cambridge University Press, pp. 92-134.

Middleburg, J., Weijden, C. van der, Woittiez, J., 1988. Chemical processes affecting the mobility of major, minor, and trace elements during weathering of granitic rocks, Chemical Geology 68, 253–273.

Miller, C.F., Wooden, J.L., Bennett, V.C., Wright, J.E., Solomon, G.C., Hurst, R.W., 1990. Petrogenesis of the composite peraluminous-metaluminous Old Woman-Piute Range batholith, southeastern California; Isotopic constraints, in: Anderson, J. (Ed.), The nature and origin of Cordilleran magmatism: Boulder, Colorado, Geological Society of America Memoir 174, 99–109.

Miller, C.F., Wooden, J.L., 1994. Anatexis, hybridization and the modification of ancient crust: Mesozoic plutonism in the Old Woman Mountains area, California. Lithos 32, 111–133.

Miller, J.S., Glazner, A.F., Farmer, G.L., Suayah, I.B., Keith, L.A., 2000. A Sr, Nd, and Pb isotopic study of mantle domains and crustal structure from Miocene volcanic rocks in the Mojave Desert, California. Geological Society of American Bulletin 112, 1264–1279.

Miller, J.S., Miller, C.F., 1991. Tertiary Extension-Related Volcanism, Old Woman Mountains Area Eastern Mojave Desert, California. Journal of Geophysical Research 96, 13,629–13,643.

Modi, A.L., Fedo, C.M., Young, G.M., Wayne, N.H., 2009. Exploring weathering and alteration trends in A-CN-K-FM three-dimensional space. Geological Society of America Abstracts with Programs 41, p. 428.

Nesbitt, H.W., 1979. Mobility and fractionation of rare earth elements during weathering of a granodiorite. Nature 279, 206–210.

Nesbitt, H.W., Fedo, C.M., Young, G.M., 1997. Quartz and feldspar stability, steady and non-steady state weathering, and petrogenesis of siliciclastic sands and muds. Journal of Geology 105, 173-191.

Nesbitt, H.W., Markovics, G., 1997. Weathering of granodioritic crust, long-term storage of elements in weathering profiles, and petrogenesis of siliciclastic sediment. Geochimica et Cosmochimica Acta 61, 1653–1670.

Nesbitt, H.W., Markovics, G., Price, R.C., 1980. Chemical processes affecting alkalis and alkaline earths during continental weathering. Geochimica et Cosmochimica Acta 44, 1659–1666.

Nesbitt, H.W., Young, G.M., 1982. Early Proterozoic climates and plate motions inferred from major element chemistry of lutites. Nature 299, 715–717.

Nesbitt, H.W., Young, G.M., 1984. Prediction of some weathering trends of plutonic and volcanic rocks based on thermodynamic and kinetic considerations. Geochimica et Cosmochimica Acta 28, 1523–1534.

Nesbitt, H.W., Young, G.M., 1989. Formation and diagenesis of weathering profiles. The Journal of Geology 97, 129–147.

Nesbitt, H.W., Young, G.M., 1996. Petrogenesis of sediments in the absence of chemical weathering: effects of abrasion and sorting on bulk composition and mineralogy. Sedimentology 43, 341– 358.

Nesbitt, H.W., Young, G.M., McLennan, S.M., Keays, R.R., 1996. Effects of chemical weathering and sorting on the petrogenesis of siliciclastic sediments, with implications for provenance studies. Journal of Geology 104, 525–542.

Nichols, K.K., Bierman, P.R., Eppes, M.C., Caffee, M., Finkel, R., Larsen, J., 2005. Late Quaternary history of the Chemehuevi Mountain piedmont, Mojave Desert, deciphered using ^{10}Be and ^{26}Al. American Journal of Science 305, 345–368.

Nichols, K.K., Bierman, P.R., Eppes, M.C., Caffee, M., Finkel, R., Larsen, J., 2007. Timing of surficial process changes down a Mojave Desert piedmont. Quaternary Research 68, 151–161.

Nichols, K.K., Bierman, P.R., Hooke, R.L., Clapp, E.M., Caffee, M., 2002. Quantifying sediment transport on desert piedmonts using ^{10}Be and ^{26}Al. Geomorphology 45, 105-125.

NOAA, 2010. California, U.S. National Oceanic and Atmospheric Administration (NOAA), Western Regional Climate Center, Reno, NV.

Pan,Y., Stauffer, M.R., 2004. Cerium anomaly and Th/U fractionation in the 1.85 Ga Flin Flon Paleosol: Clues from REE- and U-rich accessory minerals and implications for paleoatmospheric reconstruction. American Mineralogist 85, 898-911.

Parsons, I., Thompson, P., Lee, M.R., Cayzer, N., 2005. Alkali feldspar microtextures as provenance indicators in siliciclastic rocks and their role in feldspar dissolution during transport and diagenesis. Journal of Sedimentary Research 75, 921–942.

Pe-Piper, G., Triantafyllidis, S., Piper, D.W., 2008. Geochemical identification of clastic sediment provenance from known sources of similar geology: the Cretaceous Scotian Basin, Canada Basin, Canada. Journal of Sedimentary Research 78, 595–607.

Powers, M.C., 1953. A new roundness scale for sedimentary particles. Journal of Sedimentary Petrology 23, 117–119.

Price, R.C., Gray, C.M., Wilson, R.E., Frey, F.A., Taylor, S.R., 1991. The effects of weathering on rare earth element, Y and Ba abundances in Tertiary basalts from southeastern Australia. Chemical Geology 93, 245–265.

Rahman, M.J.J., Suzuki, S., 2007. Geochemistry of sandstones from the Miocene Surma Group, Bengal Basin, Bangladesh: Implications for Provenance, tectonic setting and weathering. Geochemical Journal 41, 415-428.

Roddaz, M., Viers, J., Brusset, S., Baby, P., Boucayand, C., Herail, G., 2006. Controls on weathering and provenance in the Amazonian foreland basin: Insights from major and trace element geochemistry of Neogene Amazonian sediments. Chemical Geology 226, 31-65.

Rollinson, H., 1993. Using geochemical data: evaluation, presentation, interpretation. Prentice Hall.

Roser, B.P., Korsch, R.J., 1988. Provenance signatures of sandstone-mudstone suites determined using discriminant function analysis of major-element data. Chemical Geology 67, 119–139.

Ryan, K.M., Williams, D.M., 2007. Testing the reliability of discrimination diagrams for determining the tectonic depositional environment of ancient sedimentary basins. Chemical Geology 242, 103–125.

Schoenborn, W.A., and Fedo, C.M., 2011, Provenance and paleoweathering reconstruction of the Neoproterozoic Johnnie Formation, southeastern California. Chemical Geology 285, 231-255.

Singh, P., 2010. Geochemistry and provenance of stream sediments of the Ganga River and its major tributaries in the Himalayan region, India. Chemical Geology 269, 220-236.

Singh, P., Rajamani, V., 2001. REE geochemistry of recent clastic sediments from the Kaveri floodplains, southern India: Implication to source area weathering and sedimentary processes. Geochimica et Cosmochimica Acta 65, 3093–3108.

Spalletti, L.A., Queralt, I., Sergio, D.M., Colombo, F., Maggi, J., 2008. Sedimentary petrology and geochemistry of siliciclastic rocks from the upper Jurassic Tordillo Formation (Neuquen Basin, western Argentina): Implications for provenance and tectonic setting. South American Earth Sciences 25, 440-463.

Suttner, L.J., Basu, A., Mack, G.H., 1981. Climate and the origin of quartz arenites. Journal of Sedimentary Petrology 51, 1235–1246.

Taylor, G., Eggleton, R.A., 2001. Regolith Geology and Geomorphology. John Wiley & Sons, Ltd.

Taylor, S.R., McLennan, S.M., Armstrong, R.L., Tarney, J., 1981. The Composition and Evolution of the Continental Crust: Rare Earth Element Evidence from Sedimentary Rocks [and Discussion]. Philosophical Transactions of The Royal Society London 301, 381-399.

Taylor, S.R., McLennan, S.M., 1985. The Continental Crust: Its composition and evolution. Blackwell Scientific Publishers.

Taylor, S.R., Rudnick, R.L., McLennan, S.M., Eriksson, K.A., 1986. Rare earth element patterns in Archean high-grade metasediments and their tectonic significance. Geochimica et Cosmochimica Acta 50, 2267 – 2279.

Totten, M.W., Hanan, M.A., Weaver, B.L., 2000. Beyond whole-rock geochemistry of shales: The importance of assessing mineralogic controls for revealing tectonic discriminants of multiple sediment sources for the Ouchita Mountain flysch deposits. Geological Society of American Bulletin 122, 1012–1022.

Weltje, G.J., 2002. Quantitative analysis of detrital modes: statistically rigorous confidence regions in ternary diagrams and their use in sedimentary petrology. Earth-Science Reviews 57, 211–253.

Whitmore, G.P., Crook, K.A.W., Johnson, D.P., 2004. Grain size control of mineralogy and geochemistry in modern river sediment, New Guinea, Papua New Guinea. Sedimentary Geology 171, 129–157.

Willan, R.C.R., 2003. Provenance of Triassic-Cretaceous sandstones in the Antarctic Peninsula: Implications for terrane models during Gondwana breakup. Journal of Sedimentary Research 73, 1062–1077.

Wronkiewicz, D.J., Condie, K.C., 1987. Geochemistry of Archean shales from the Witwatersrand Supergroup, South Africa: Source-area weathering and provenance. Geochimica et Cosmochimica Acta 51, 2401–2416.

Yan, Z., Wang, Z., Wang, T., Yan, Q., Xiao, W., Li, J., 2006. Provenance and tectonic setting of clastic deposits in the Devonian Xicheng Basin, Qinling Orogen, Central China. Journal of Sedimentary Research 76, 557–574.

Young, G.M., Nesbitt, H.W., 1998. Processes controlling the distribution of Ti and Al in weathering profiles, siliciclastic sediments and sedimentary rocks. Journal of Sedimentary Research 68, 448–455.

Appendix 1:

Stepladder sample descriptions

A1.1. Caliche

CF00-01 is the representative caliche sample that was used to estimate its compositional influence on the Stepladder sediment. Collected in zone I, the caliche was an indurated crust (~3 cm thick) on the pluton and within open joints. In hand sample (Fig. A1.1), it occurs as clumped aggregates, yellow to white in color. The thin section scan (Fig. A1.2A) shows theinternal texture of the caliche, particularly the inclusions and open spaces. In plane and polarized light (Fig. A1.2B, C) the voids and included silicate grains (note the square-shaped plagioclase clast on the right) are more easily identified. Round aggregate (similar to those seen in Fig. A1.1) are found in every sediment sample and are easily identified in both hand samlple and thin section (see Appendix A1.4).

Figure A1.1. Photograph of caliche aggregates.

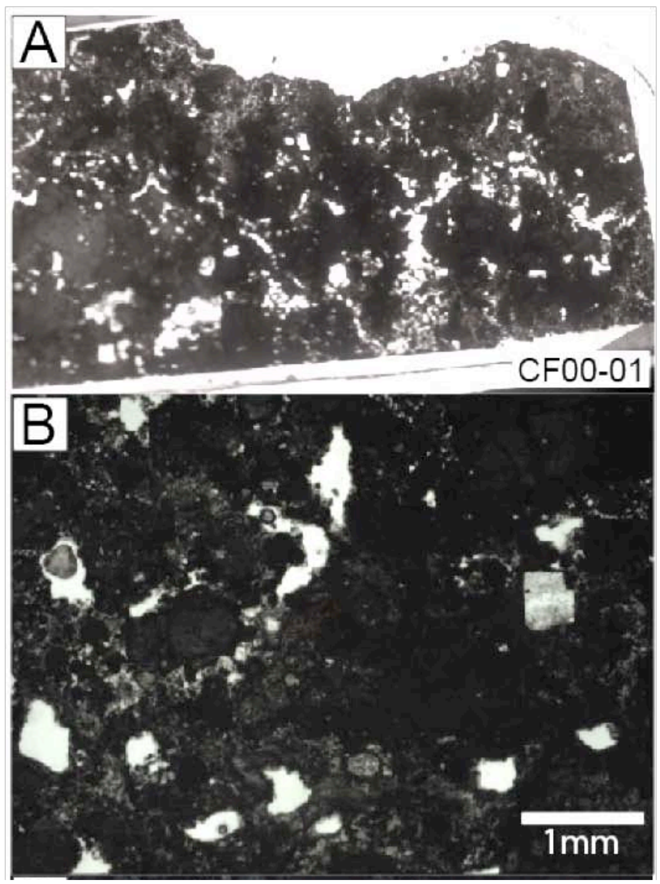

Figure A1.2. Caliche thin section. (A) Thin section scan of CF00-01. Photomicrographs of caliche in (B) Plane light.

A1.2. Fresh Stepladder granodiorite samples

Characteristics of average Stepladder bedrock were summarized from four bedrock samples: CF96-04, CF96-08, CF00-18, and ST09-02. Of the four samples, only CF00-18 and ST09-02 had high-precision trace elements compositions reported; the measured compositions of CF96-08 and CF96-17 only reported major oxides and REE contents. All four, however, were made into thin sections (Fig. A1.3) and examined petrographically. In QAP space (Fig. A1.4), three of the samples plot in the granodiorite composition field, while one plot on the boundary separating the granite from the granodiorite compostion fields.

Although the modal mineralogy of the bedrock samples varied slightly, they all contained the same primary rock forming minerals. Tabular subhedral plagioclase is the most apparent phase and tends to be < 3 cm in size. Many of the megacrysts show albite twinning (Fig. A1.5) or are concentrically zoned (Fig. A1.6) with an abundance of inclusions (Fig. A1.7), consisting of plagioclase, quartz, and euhedral accessory minerals. Anhedral, perthitic K-feldspar (Figs. A1.6, A1.8), about 0.5-1 mm in size, contribute to the interstitial quartz and plagioclase matrix, and is associated with trace amounts of myrmekite. Most quartz are unaltered (Figs. A1.5, A1.8) and occur interstitial to plagioclase, perthite, biotite and opaques. Rare grains poikilitically include smaller than average plagioclase and biotite laths. Larger quartz crystals may be composite, but they mostly exist as small anhedral blebs with undulating extinctions (Figs. A1.5, A1.9). When contiguous to plagioclase and biotite, grain contacts are irregular ragged, rutted, pitted and clouded with fine minerals and clays; occasional quartz-plagioclase margins are sharp, smooth, and cloudless. Large, euhedral to subhedral biotite (Figs. A1.5, A1.8-

9) represents the only mafic component and tend to be euhedral to subhedral booklets about 0.2-6 mm in length. They are frequently intergrown or adjacent to each other, are associated with apatite (Fig. A1.8), zircon, and opaque minerals, most likely magnetite - ilmenite, and are partially enclosed by interstitial quartz and plagioclase. Opaque phases are either poikilitically enclosed as euhedral crystals (Fig. A1.10a) or as irregular blebs rimming secondary titanite or replacing biotite (Fig. A1.10b). Other prominent accessory minerals include large euhedral titanite (< 2 mm; Fig. A1.10b), acicular zircon, and prismatic apatite (< 10 μm; Fig. A1.10c, d). Common secondary minerals include: titanite, found as a discontinuous rim around opaques (Fig. A1.10a, b) and biotite; chlorite, replacing biotite and creating a prevalent "washed-out" green pleochroism (Fig. A1.9a); hematite and rutile, less frequently replacing biotite; and sericite, causing a cloudy appearance (Figs. A1.5, A1.7, A1.8, A1.10) in the cores and Ca-rich zones of the plagioclase grains.

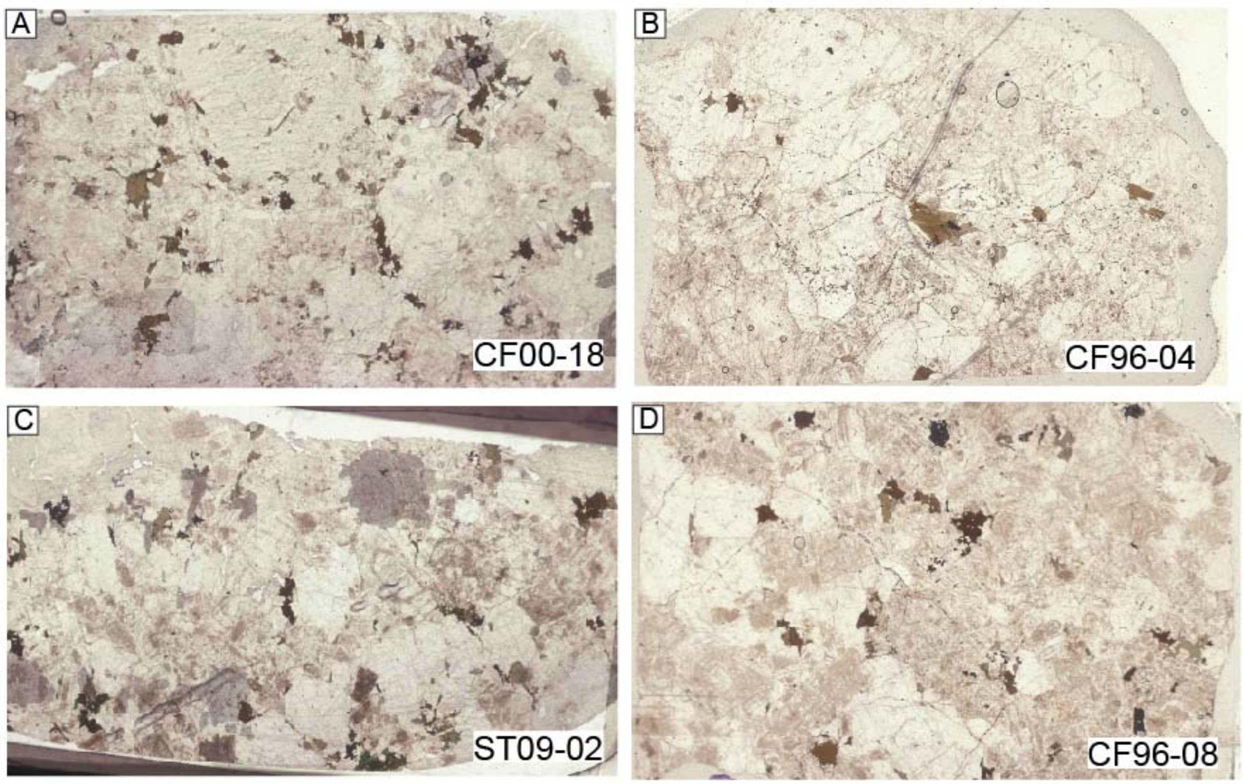

Figure A1.3. Thin section scans of the four bedrock samples. Samples include: (A) CF00-18, (B) CF96-04, (C) ST09-02, and (D) CF96-08. All four photos are at the same scale;

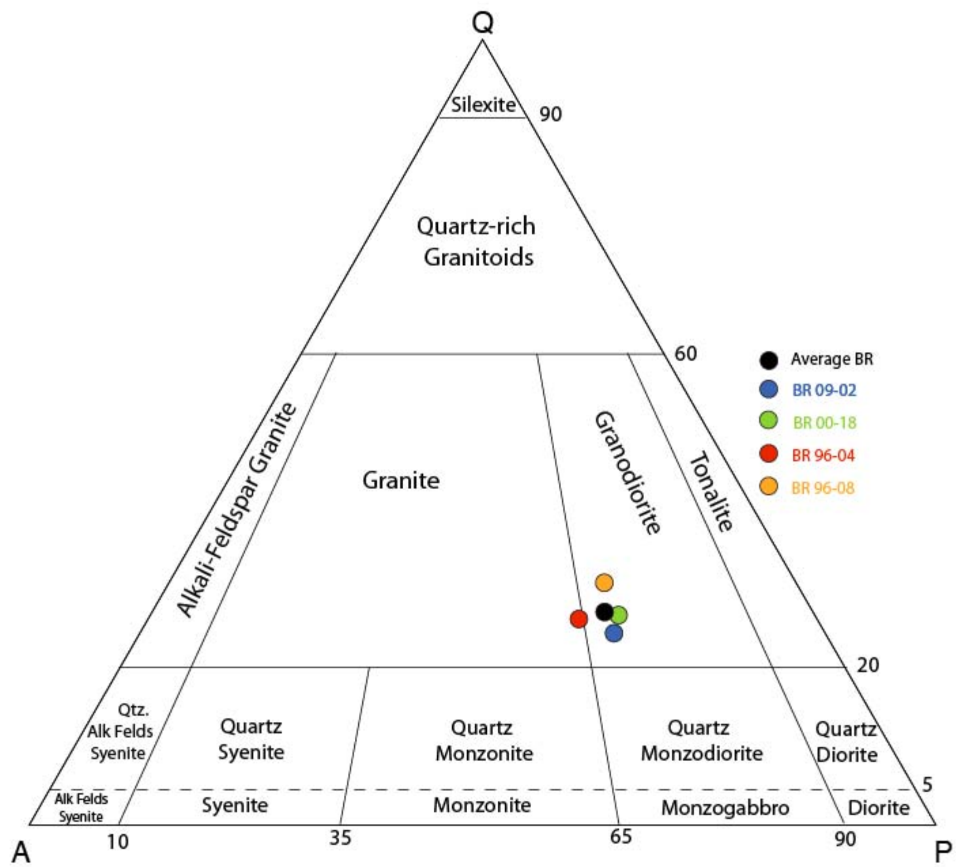

Figure A1.4. Quartz - Alkali Feldspar - Plagioclase (QAP) plot of Stepladder bedrock samples from modal mineralogy.

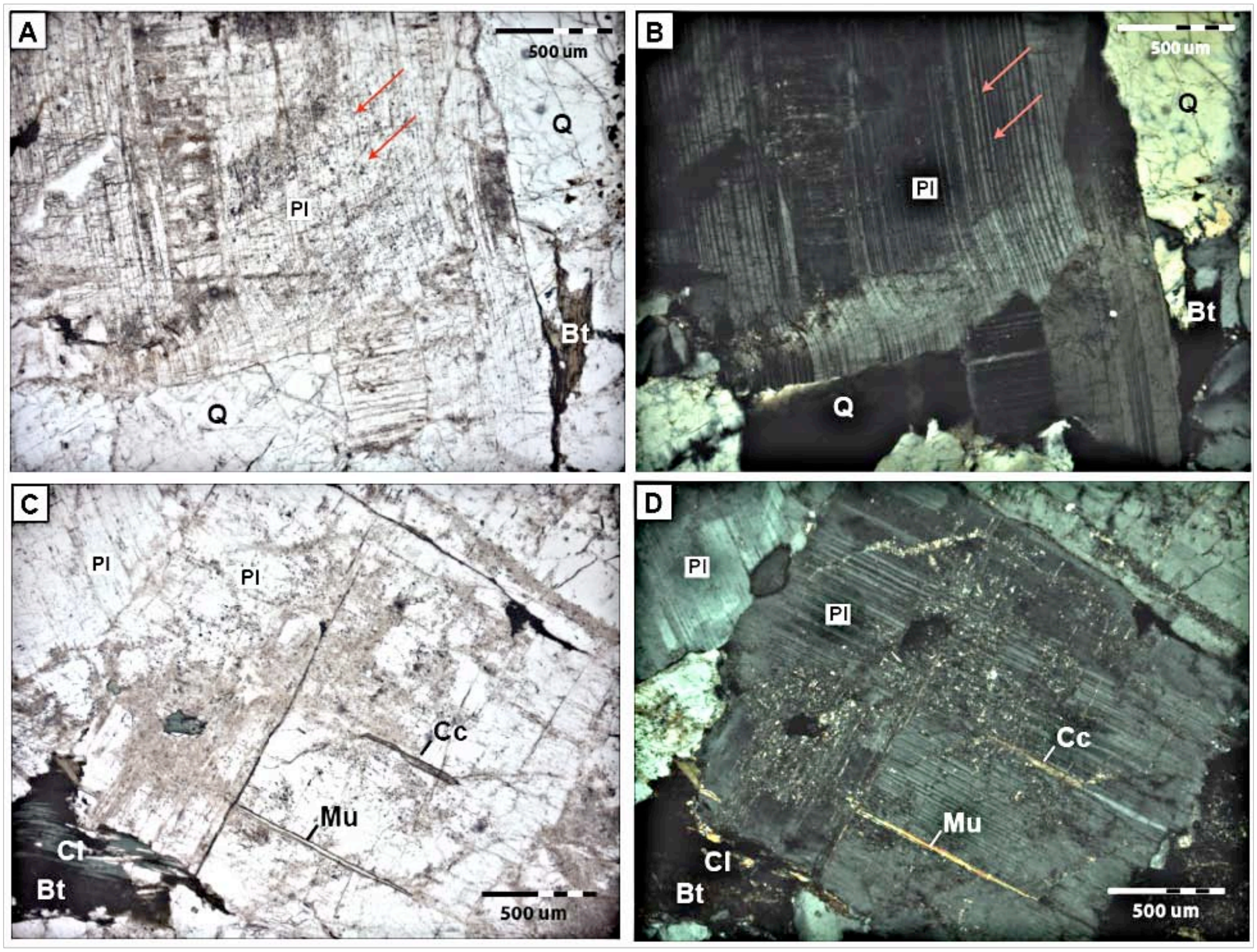

Figure A1.5. Photomicrographs of plagioclase megacryst in (A) plane light and (B) crossed polars. Red arrows point to albite twins that show slight deformation along the base of the crystal. Below and to the right of the plagioclase grain are quartz grains that show undulating extinction. Plagioclase grain in (C) Plane light photomicrograph and (D) crossed polars. Along with albite twinning, the grain includes secondary (Cc) calcite, (Mu) muscovite, and other clays. (Bt) Biotite partially replaced with (Cl) chlorite occur in lower left of (C) and (D).

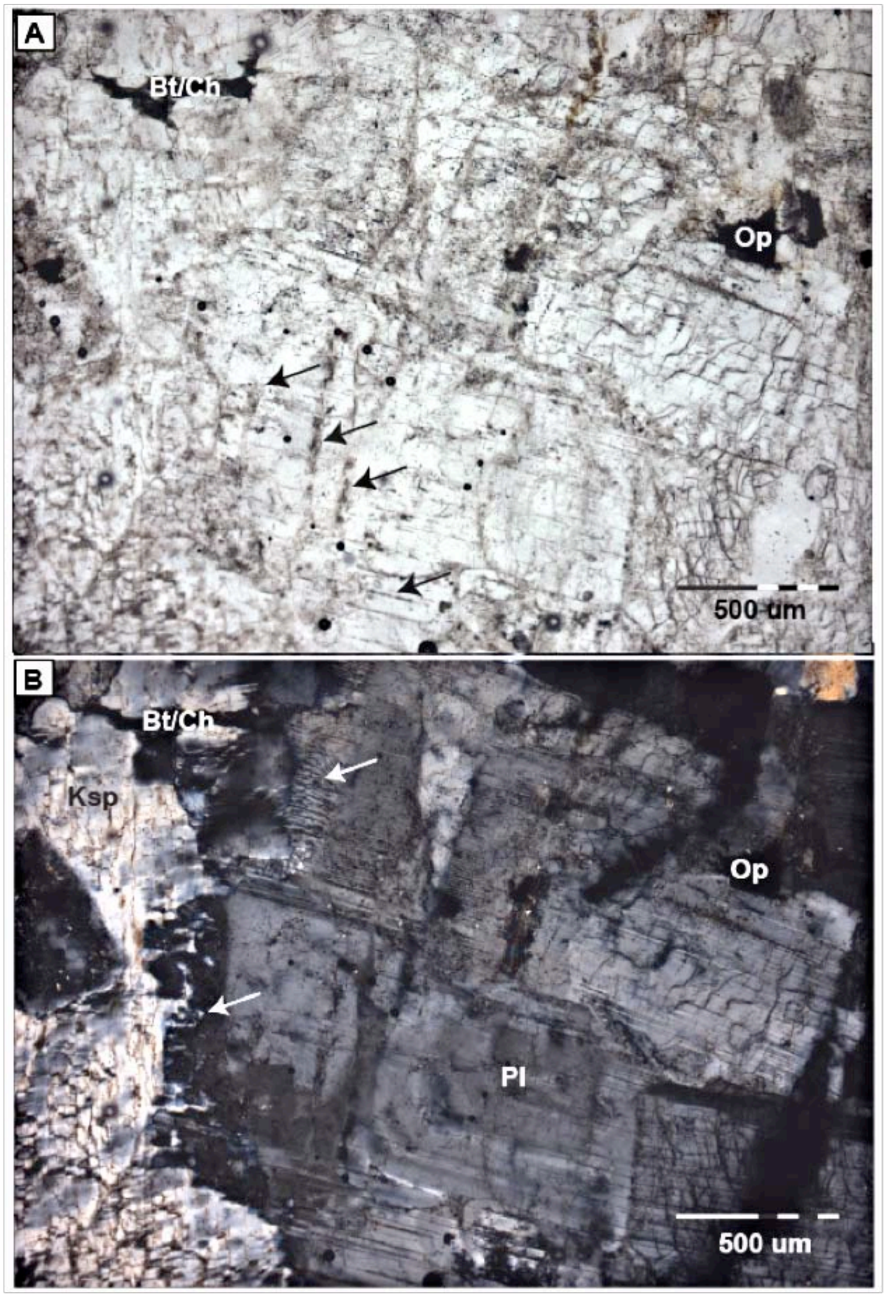

Figure A1.6. Plagioclase grains in (A) plane light and (B) crossed polars showing oscillatory zoning (black arrows). Perthitic (Ksp) K-feldspar forms an intergrown boundary with plagioclase grain.

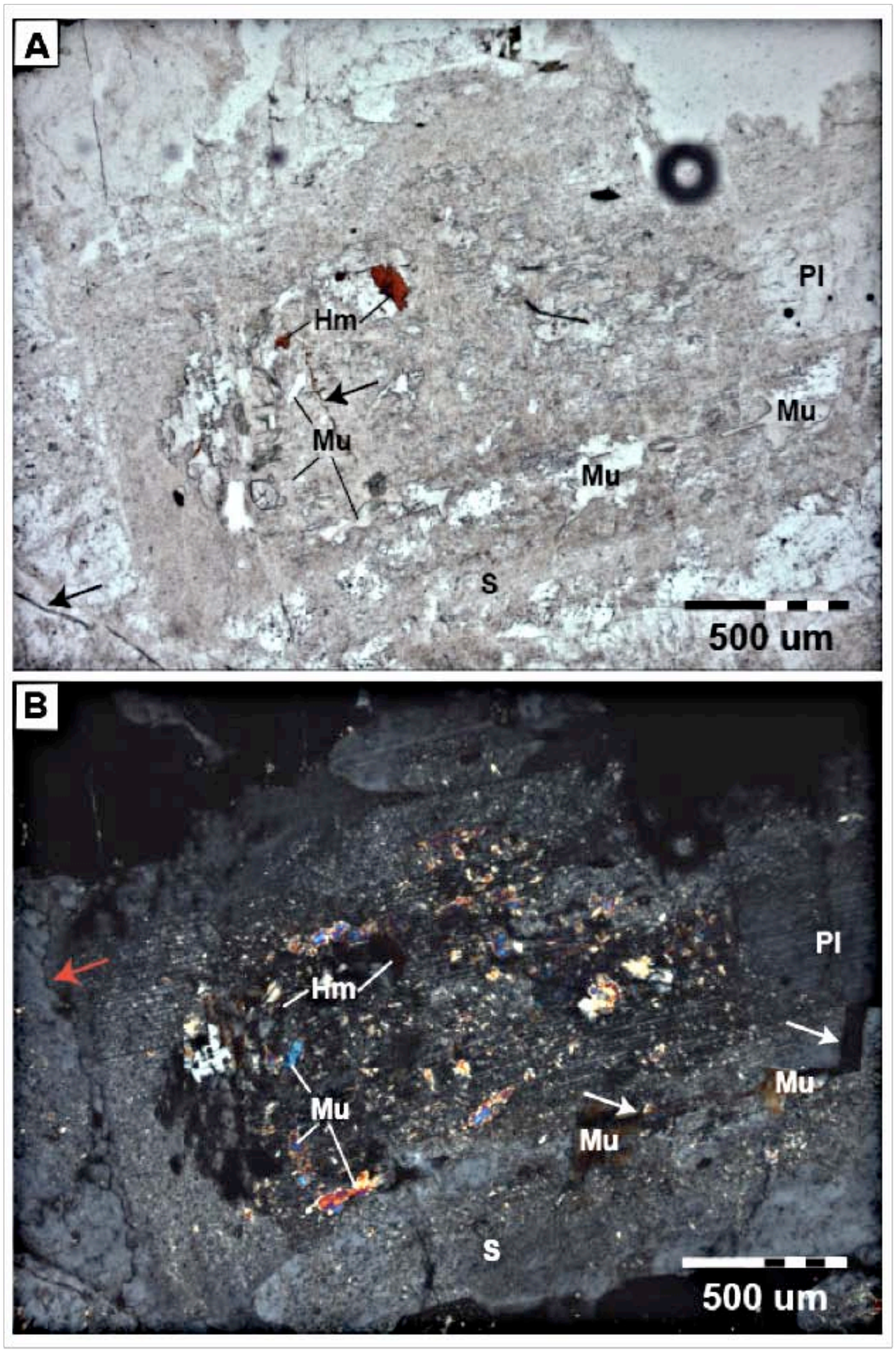

Figure A1.7. Plagioclase grain in (A) plane light and (B) crossed polars, which includes (Hm) hematite, (Mu) muscovite, and (S) sericite.

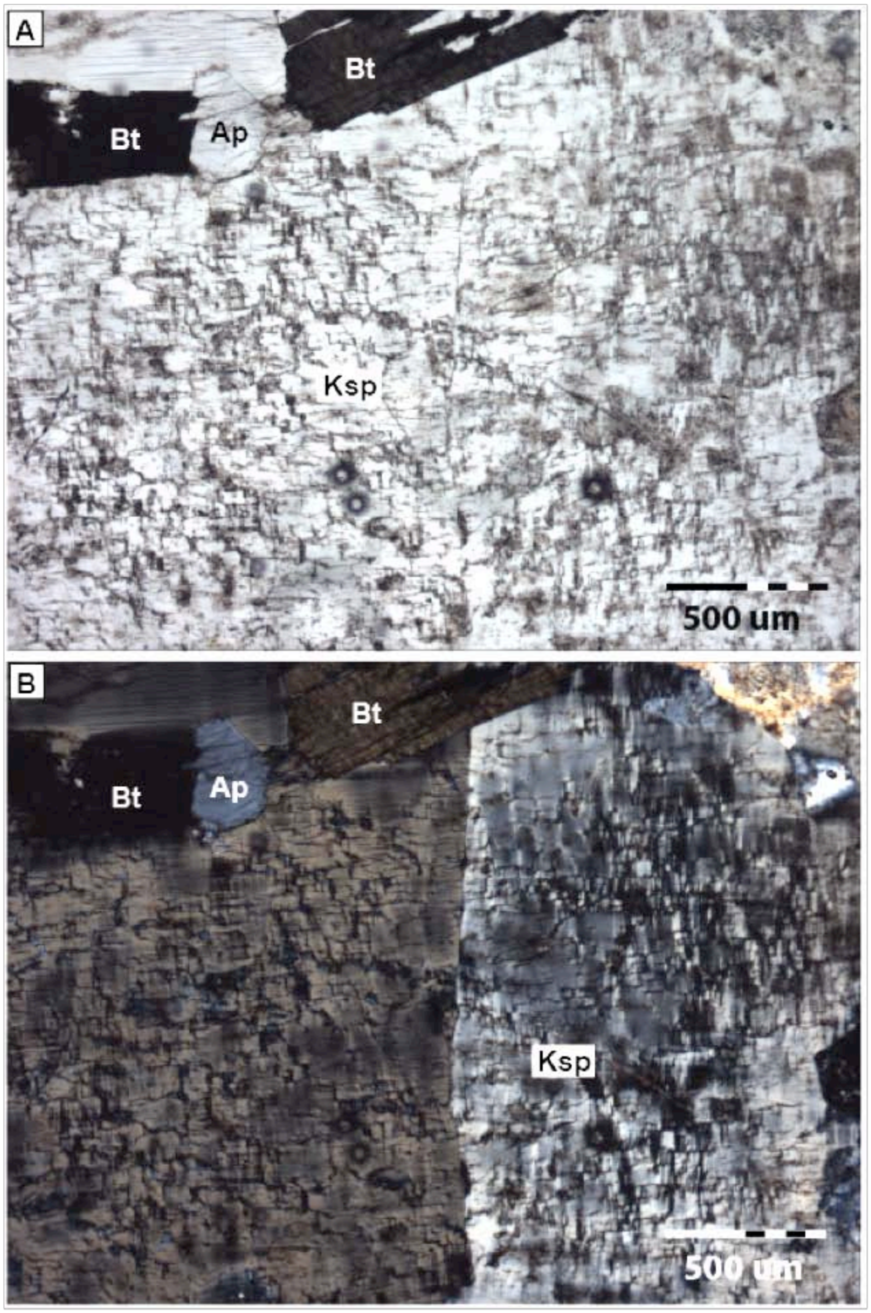

Figure A1.8. Perthitic K-feldspar in (A) plane light and (B) crossed polars that shows the typical patch-work texture. Note the (Bt) biotite and (Ap) apatite in the upper right.

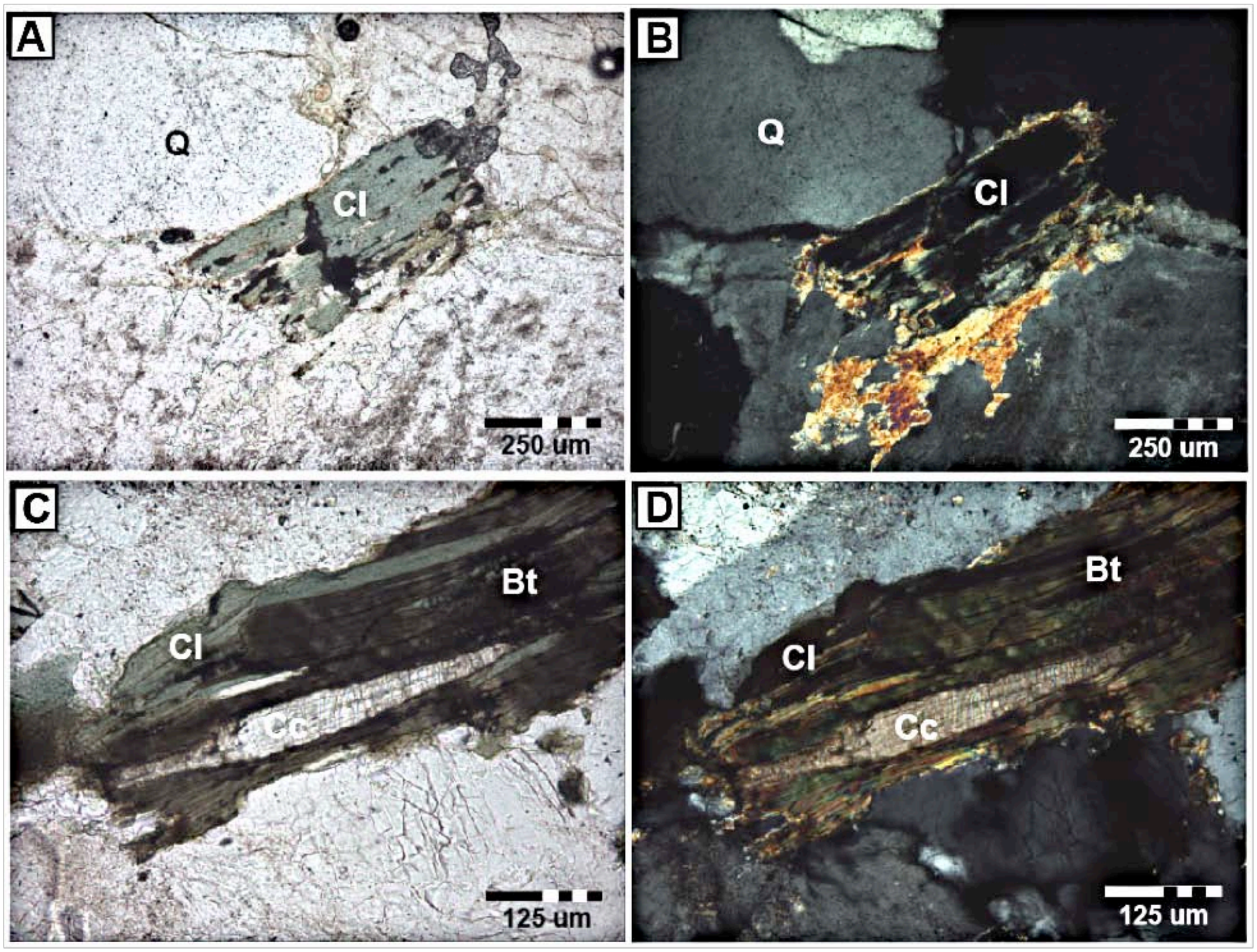

Figure A1.9. Quartz and biotite in (A) plane light and (B) crossed polars where biotite is nearly replaced by (Cl) chlorite. (Bt) Biotite is partially replaced by (Cl) chlorite and (Cc) calcite in (C) plane light and (D) crossed polars.

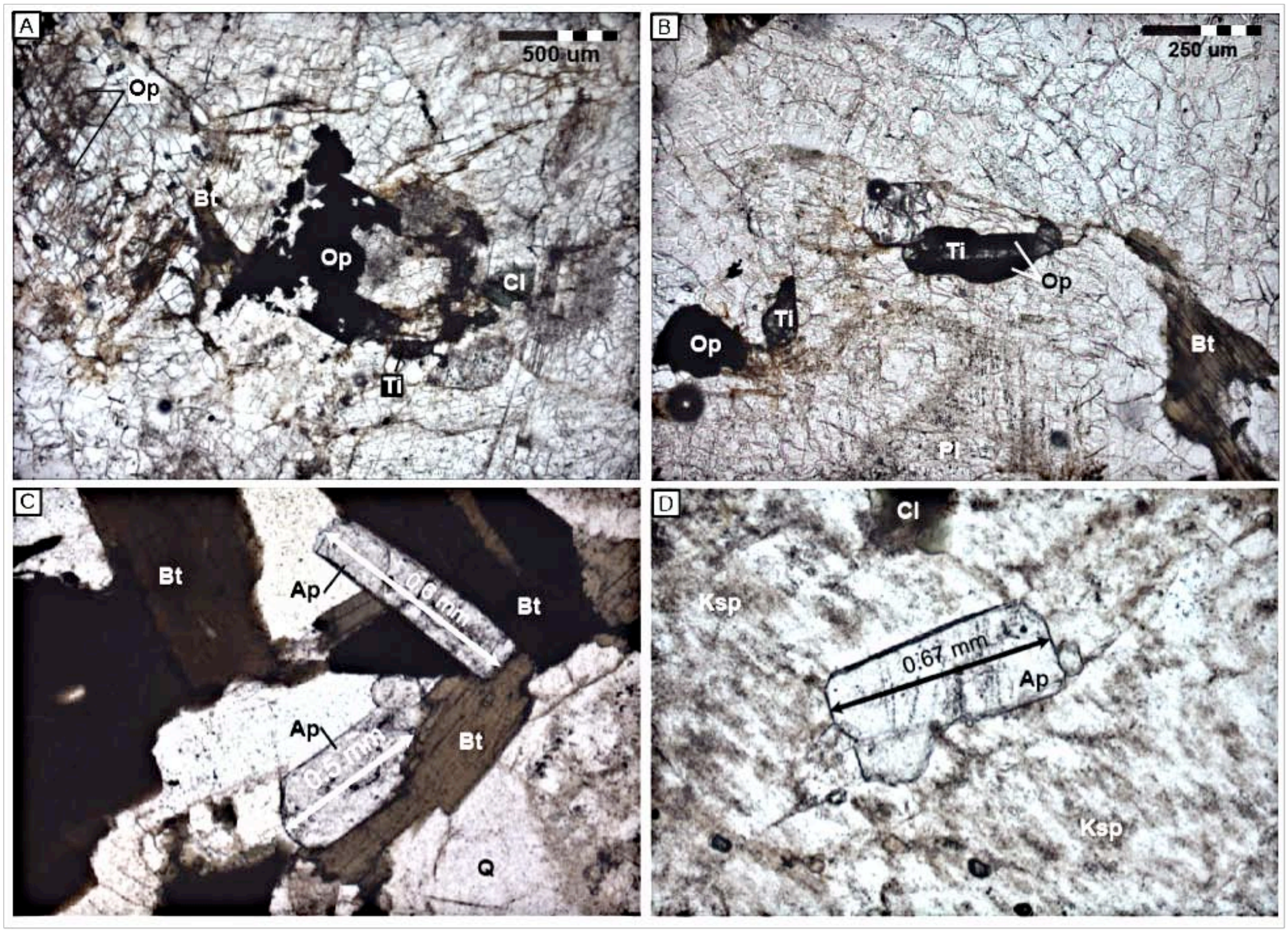

Figure A1.10. Plane light photomicrographs of (A) euhedral (to subhedral) opaque oxide phases associated with (Bt) biotite, (Ti) titanite, and (Cl) chlorite. (B) Titanite rimmed with (Op) opaque oxides and associated with (Bt) biotite. (C) Two large (Ap) apatite grains (top = 0.6 mm; bottom = 0.5 mm) associated with (Bt) biotite. (D) Large (0.67 mm) apatite grain included in (Ksp) K-feldspar.

A1.3 Weathered Stepladder bedrock: regolith and grus samples

Two regolith samples (CF00-04 and CF00-05) and one grus sample (CF96-01) were analyzed in the study (Fig. A1.11). Both regolith samples had similar petrographic characteristics and geochemical compositions (major and trace elements). Grus has similar petrographic features, but differs in composition. Modal mineralogy of the regolith and grus samples differed slightly because biotite abundance varied between the samples. Despite the minor variations in modal mineralogy, the regolith (Fig. A1.12) and grus (Fig. A1.13) samples contained the same primary mineral phases and many of the same accessory mineral phases. In general, the regolith samples are similar to the fresh bedrock samples, both mineralogically and texturally. Grus is similar mineralogically, but does not retain a primary igneous texture.

Like fresh bedrock, plagioclase is the most abundant phase and tends to be < 3 cm, tabular megacrysts (Fig. A1.14). Many of the crystals include biotite laths (Fig. A1.14) and euhedral accessory minerals (most notably apatite). K-feldspar megacrysts are mostly sub- to anhedral perthitic grains (Fig. A1.14), about 0.5-1 mm in size, that commonly show a rippled (Fig. A1.14) to patch-work texture due to the exsolved plagioclase phases. Quartz remains unaltered and retains the undulating extinction patterns apparent in fresh bedrock samples (Fig. A1.14, A1.15). In plane light, thin dusty, grey rings that border quartz crystals are visible, as well as the red iron-oxide veinlets that can intersect the grains.

The most apparent difference between the fresh bedrock and the regolith samples was the extent of fracture development (Fig. A1.14). Within regolith, transmineral fractures cut across entire thin sections, following crystal boundaries, cleavage planes, or irregular paths. Most fractures can be traced to biotite grains (Fig. A1.14) that show evidence of oxidation (from opaque oxide precipitation) and expansion (Fig. A1.14a, b). Because most grain boundaries appear to line-up across fractures (Fig. A1.14b), limited displacement is thought to have accompanied fracturing. It is also rare to identify dissolution features along fracture walls, suggesting that the fracturing of the bedrock probably did not influence major or trace element composition.

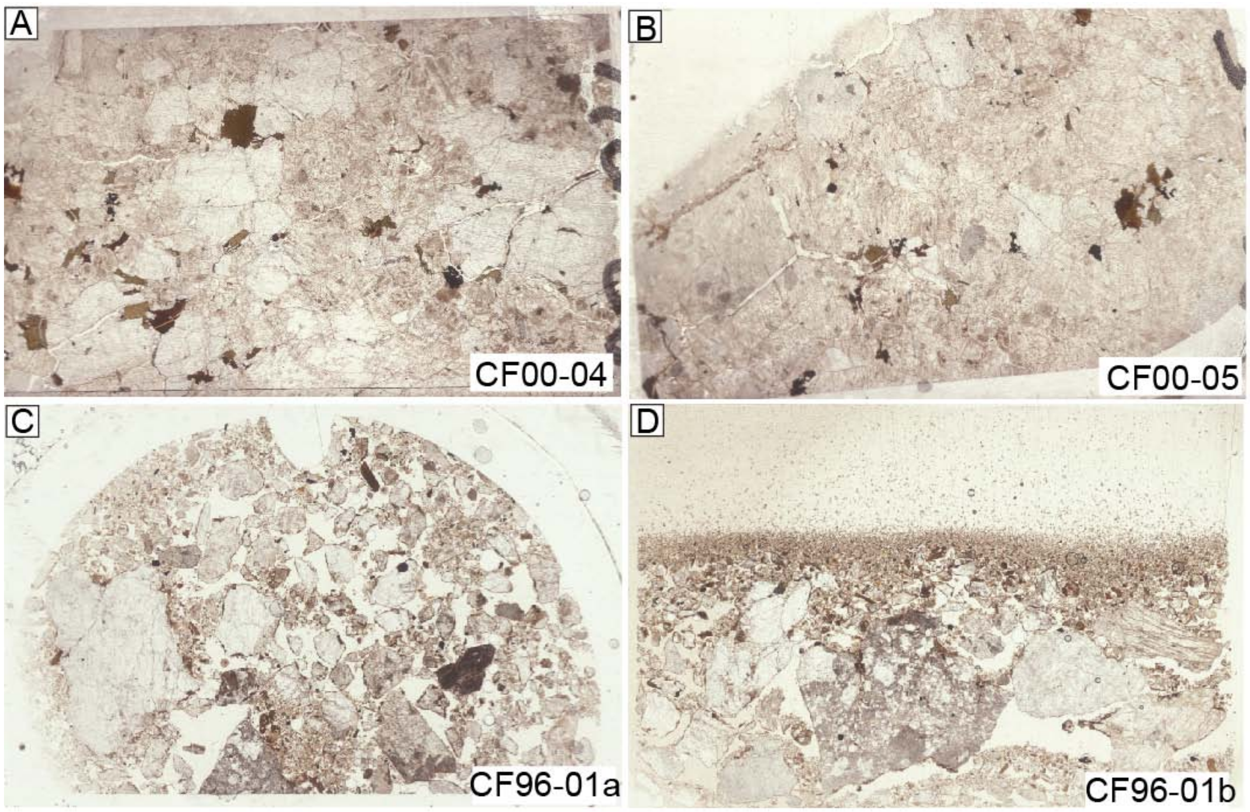

Figure A1.11. Thin section scans of regolith: (A) CF00-04 and (B) CF00-05 and grus: (C) CF96-01a and (D) CF96-01b samples. Even though grus look similar to sediment, it differs because it is non-transported.

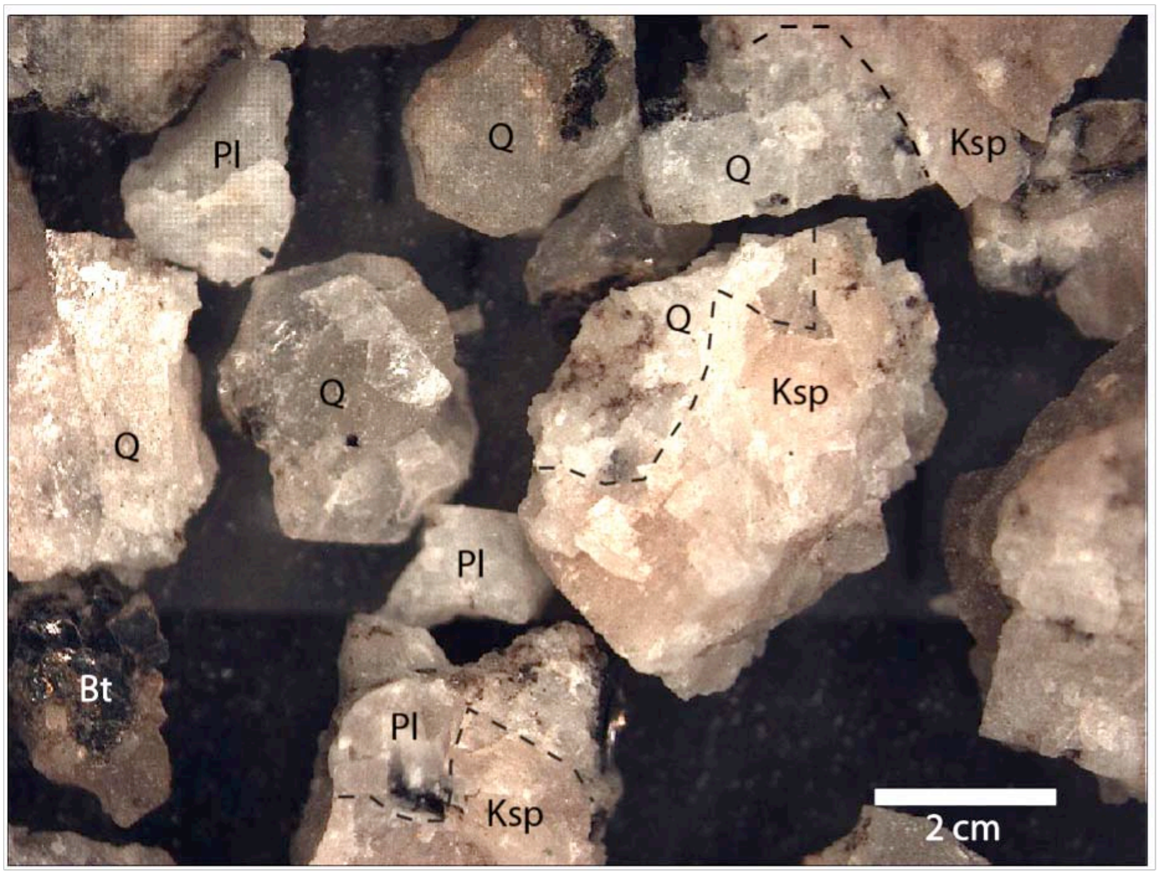

Figure A1.12. Photograph of unconsolidated regolith. Note the fresh appearance of the mineral phases.

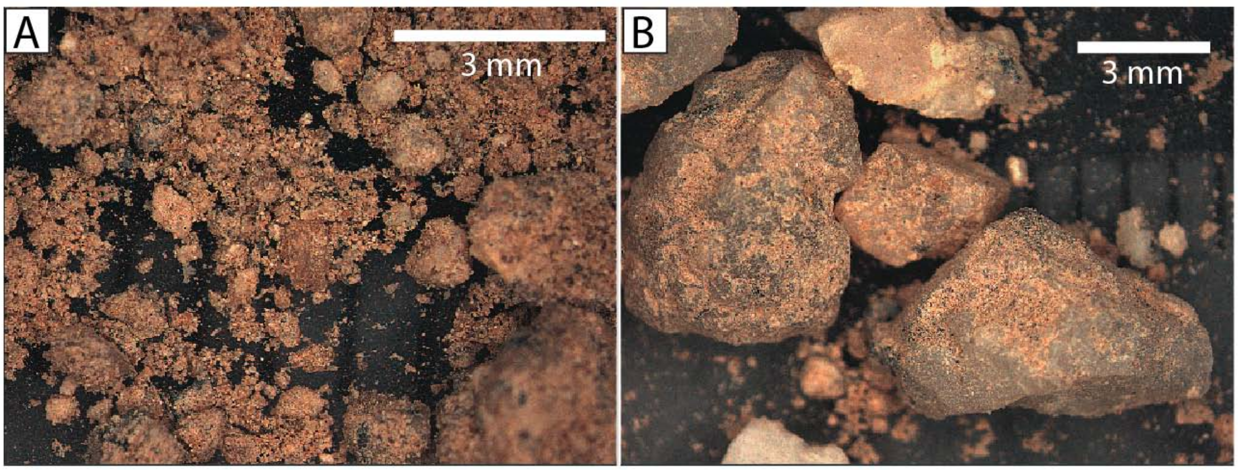

Figure A1.13. Photograph of (A) grus sample and (B) detailed shot of rock fragments in grus. Note the greater abundance of fine-grained material relative to regolith.

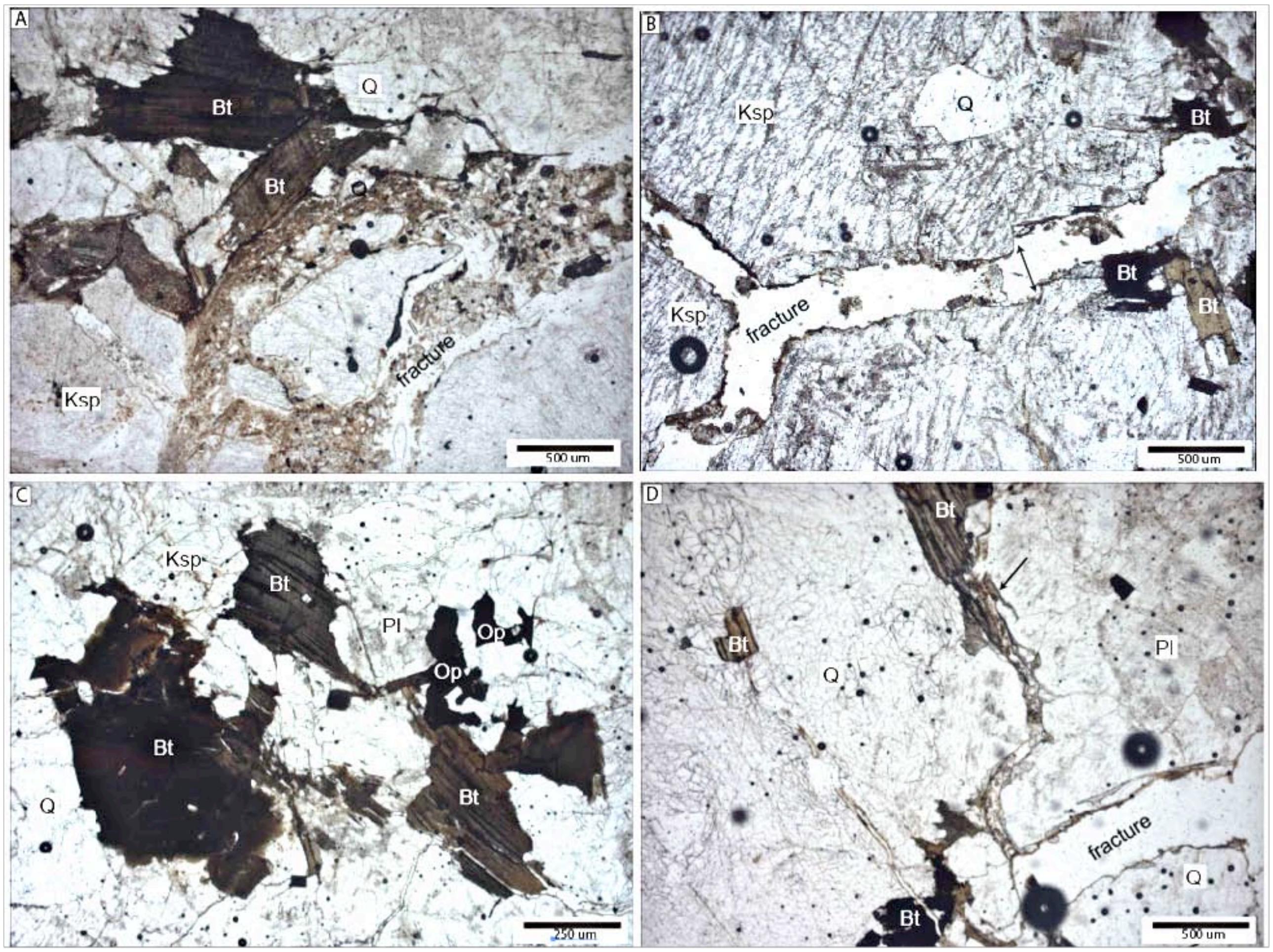

Figure A1.14. Photomicrographs of regolith samples in plane light. (A) Biotite alteration is associated with fracture development. Note the large fracture cutting through the center of the photo that is filled with red-brown material. (B) Concordant fractures cut through a ripple-textured perthitic K-feldspar. (C) Multiple biotite laths clumped together and associated with fractures development. (D) Quartz remains unaltered in regolth, despite the oxidation and expansion of biotite.

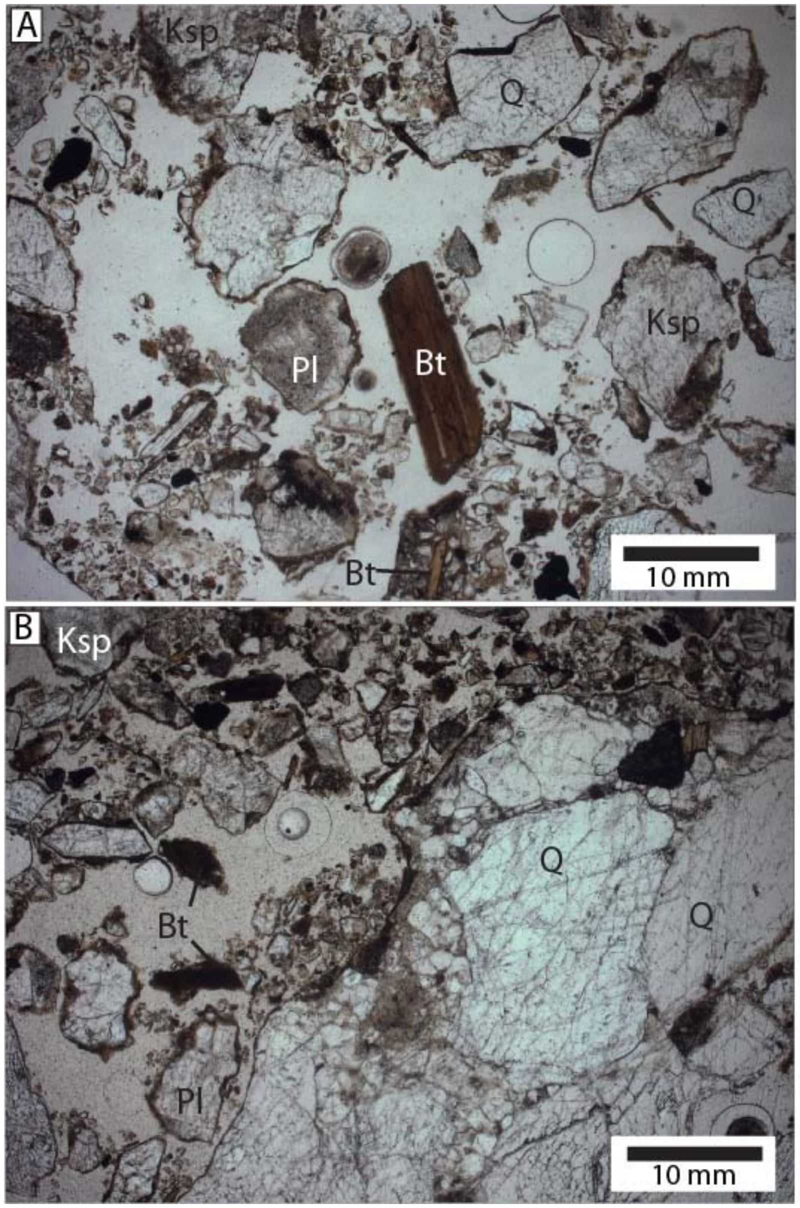

Figure A1.15. Two photomicrographs of grus in plane light. (A) Quartz, biotite, K-feldspar and plagioclase all occur and retain textures similar to bedrock and regolith. (B) Quartz remains unaltered, but there is notable enrichment in fine-grained sediments.

A1.4. Stepladder sediment samples

Stepladder sediment samples were collected along channels (Fig. A1.16) that shed clastic material from the granodioric pluton. Each sample was analyzed petrographically to identify textural and mineralogical changes, not only within individual samples but also among all 24 sediments as a whole. As explained within the main text, rock fragments are more abundant in group *G, VC,* and *C* sediments, and monomineralic fragments are more dominant in group *M, F,* and *VF* sediments. There is a slight, but noticeable, change in mineral rounding among the sediments as all phases become less angular with decreasing grain size (Table A1.1). Characterization of sediment distribution shows that samples within the same group have broadly similar textural classes, sorting, skewness, and kurtosis (Table A1.2). Because plots showing the cumulative distribution of group averages (e.g. Fig. 7) are addressed in the main text, plots showing individual cumulative distribution are included in each group description. The following sections (Appendix A1.4.1 - A1.4.6) are grouped by grain-size groupings (as discussed in the text) and include: the sediment samples making up each group, general sample descriptions, cumulative grain size distribution plots, thin section scans, and photomicrographs.

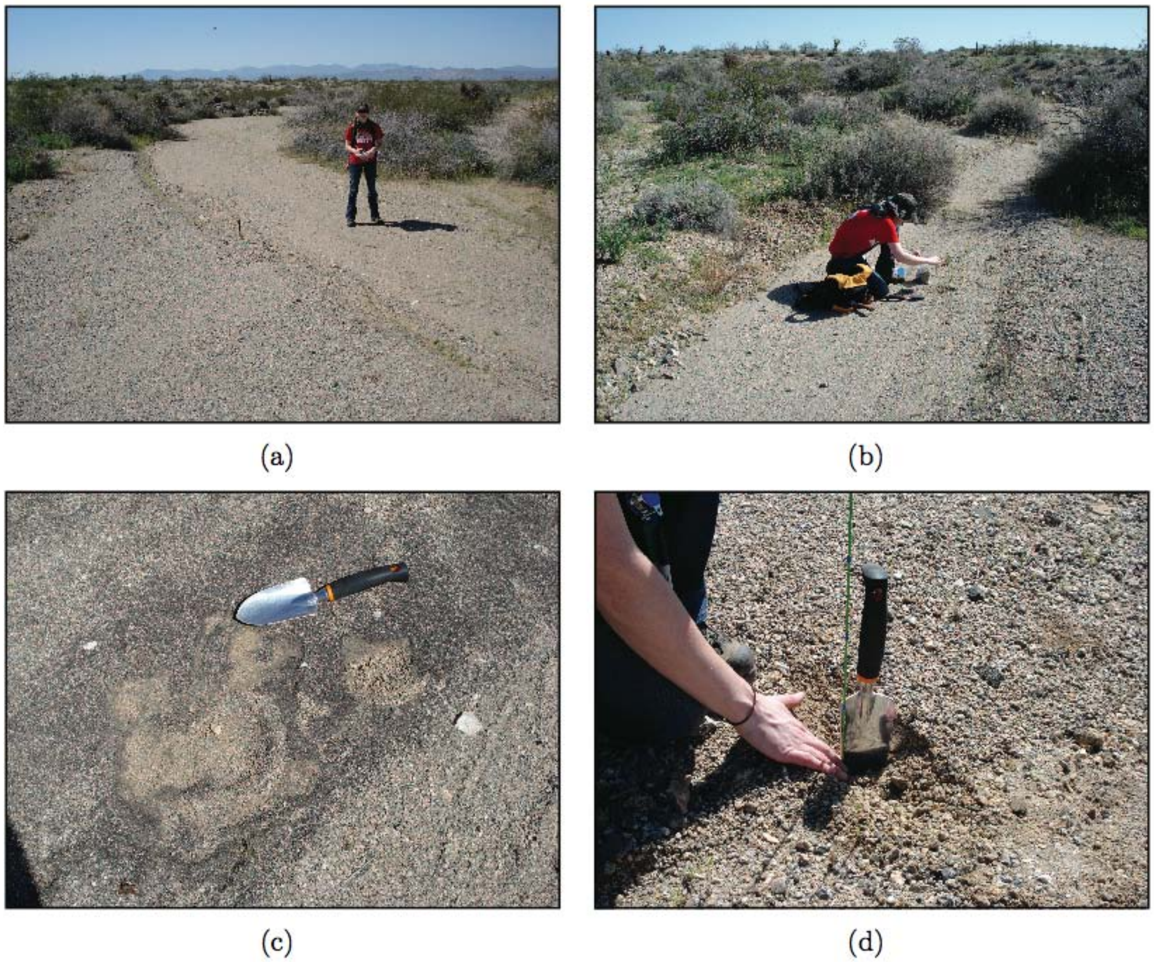

Figure A1.16. Photographs of sediment in channels draining off the Stepladder pluton. (a) Sediment channel; (b) Natural sorting of sediment within channel; (c) detail of fine-grained sediment; (d) detail of coarse-grained sediment.

Table A1.1. Mineral rounding in each sediment sample.

Sample	Quartz	Plagioclase	Alkali feldspar	Biotite
96-11	1	1	1	1
00-10	1	1	1	1
96-36	1	1	1	1
00-09	1	1 to 2	1 to 2	1
96-40	1	1 to 2	1	1
96-22	1	1 to 2	1	1
00-07	1	1 to 2	1 to 2	1
96-19	1	1 to 2	1 to 2	1
96-12	1	1 to 2	1	1
96-15	1	1 to 2	1	1
96-34	1	1 to 2	1	1
96-20	1	2 to 3	2 to 3	2
96-26	1	2	2 to 3	2
00-17	1	2 to 3	3	1
00-06	1	2	2 to 3	1
96-07	2	2 to 3	3	1
00-14	2	2	2	2
00-03	2	2	2	2
96-23	2	2	2	2
00-29	2	2	2	2
96-35	2	2	2	2
96-39	2	3	2	2
96-21	3	3	2	2
96-10	3	3	2	2

Table A1.2. Characterization of Stepladder sediment samples grouped by grain size.

Sample	Sediment Characterization			
	Textural Class	Sorting	Skewness	Kurtosis
96-11	Sandy gravel	poorly sorted	fine skewed	leptokurtic
96-36	Sandy gravel	very poorly sorted	fine skewed	platykurtic
00-10	Sandy gravel	very poorly sorted	fine skewed	mesokurtic
00-09	Muddy sandy gravel	very poorly sorted	near-symmetrical	platykurtic
00-07	Gravelly sand	poorly sorted	near-symmetrical	mesokurtic
96-22	Sandy gravel	poorly sorted	fine-skewed	platykurtic
96-40	Sandy gravel	poorly sorted	fine-skewed	mesokurtic
96-19	Gravelly sand	poorly sorted	coarse-skewed	mesokurtic
96-20	Gravelly sand	poorly sorted	coarse-skewed	mesokurtic
96-34	Gravelly sand	poorly sorted	coarse-skewed	mesokurtic
96-12	Gravelly sand	poorly sorted	coarse-skewed	mesokurtic
96-15	Slightly gravelly sand	poorly sorted	near-symmetrical	mesokurtic
96-26	Gravelly sand	poorly sorted	coarse-skewed	mesokurtic
00-17	Slightly gravelly sand	moderately well sorted	coarse-skewed	leptokurtic
00-06	Gravelly sand	moderately well sorted	strongly coarse-skewed	very leptokurtic
96-07	Gravelly muddy sand	poorly sorted	coarse-skewed	leptokurtic
00-14	Gravelly muddy sand	very poorly sorted	coarse-skewed	very platykurtic
00-03	Gravelly muddy sand	very poorly sorted	coarse-skewed	platykurtic
96-23	Gravelly muddy sand	very poorly sorted	strongly coarse-skewed	platykurtic
00-29	Gravelly muddy sand	very poorly sorted	strongly coarse-skewed	platykurtic
96-35	Gravelly muddy sand	very poorly sorted	strongly coarse-skewed	platykurtic
96-39	Gravelly muddy sand	poorly sorted	strongly coarse-skewed	platykurtic
96-21	Slightly gravelly muddy sand	poorly sorted	strongly coarse-skewed	leptokurtic
96-10	Slightly gravelly muddy sand	poorly sorted	strongly coarse-skewed	mesokurtic

A1.4.1 Group *G* sediment samples

Group *G* includes sediment samples CF96-11, CF00-10, CF96-36, and CF00-09. Samples CF96-11, CF00-10 and CF00-09 were collected in zone II, while CF96-36 was collected in zone IV (Fig. 1B). Texturally, more than 45 % of sediments in each group *G* sample are grains larger than -1 Φ in size (Fig. A1.17). Sample CF00-09 is unique, however, because 11 % of the sample consists of grains smaller than 5 Φ. The dominance of large grains is apparent in sample thin sections (Figs. A1.18) and loose sediment (Figs. A1.19).

Mineral phases present (Fig. A1.20): plagioclase (oligoclase), K-feldspar (perthite), quartz, biotite, apatite, zircon, chlorite, opaque oxides (magnetite-ilmenite), titantie, allanite, hematite, and calcite (present as caliche and as a secondary phase).

Rock fragments present (primary rock-forming mineral phases only): plagioclase-K-feldspar-quartz, plagioclase-K-feldspar-quartz-biotite, plagioclase-K-feldspar-biotite, plagioclase-quartz, plagioclase-K-feldspar, plagioclase-biotite, K-feldspar-quartz-biotite, and K-feldspar-biotite.

Associated/host-minerals for accessory phases (most common): zircon = plagioclase and biotite; apatite = biotite; chlorite = biotite; titanite = plagioclase, K-feldspar, quartz, biotite; and allanite = plagioclase.

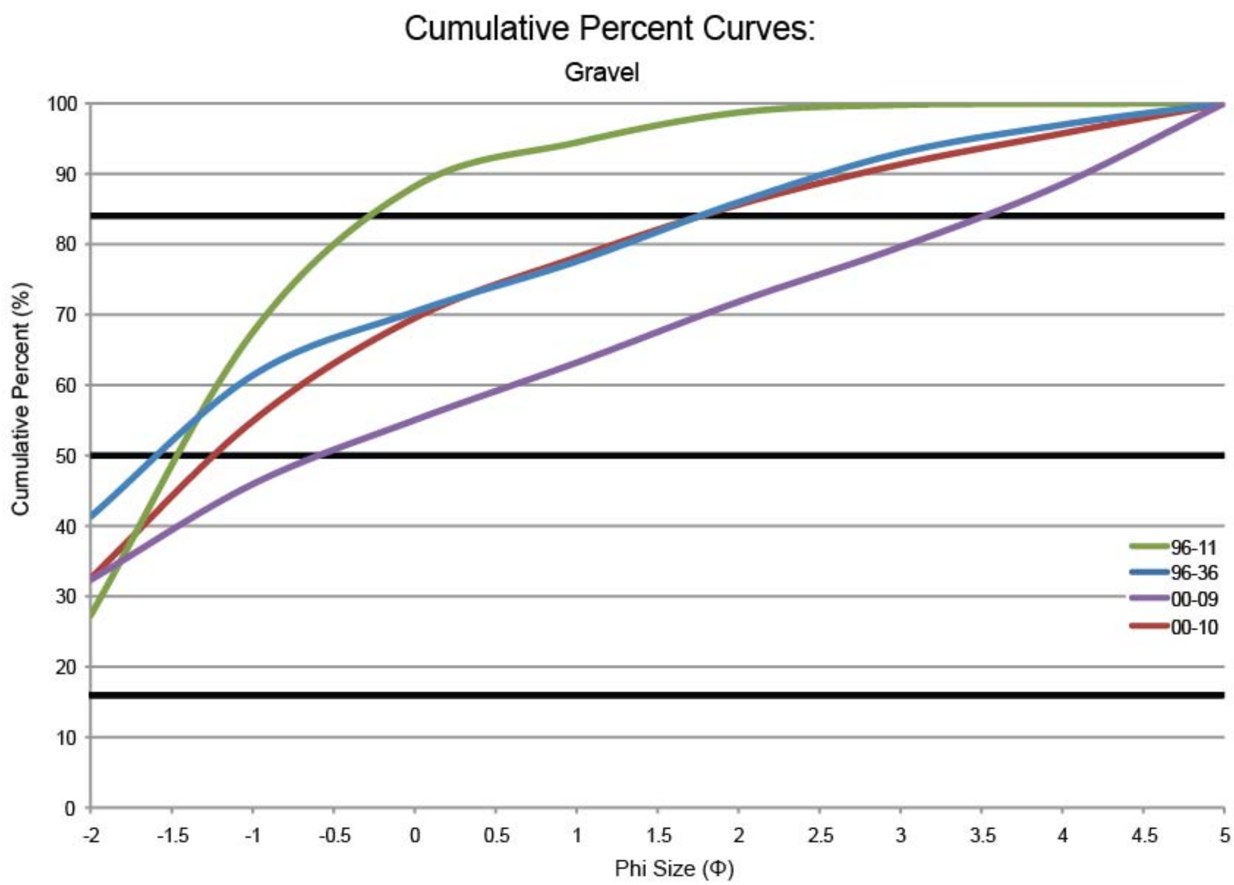

Figure A1.17. Cumulative percent grain-size distribution of individual samples in group *G*.

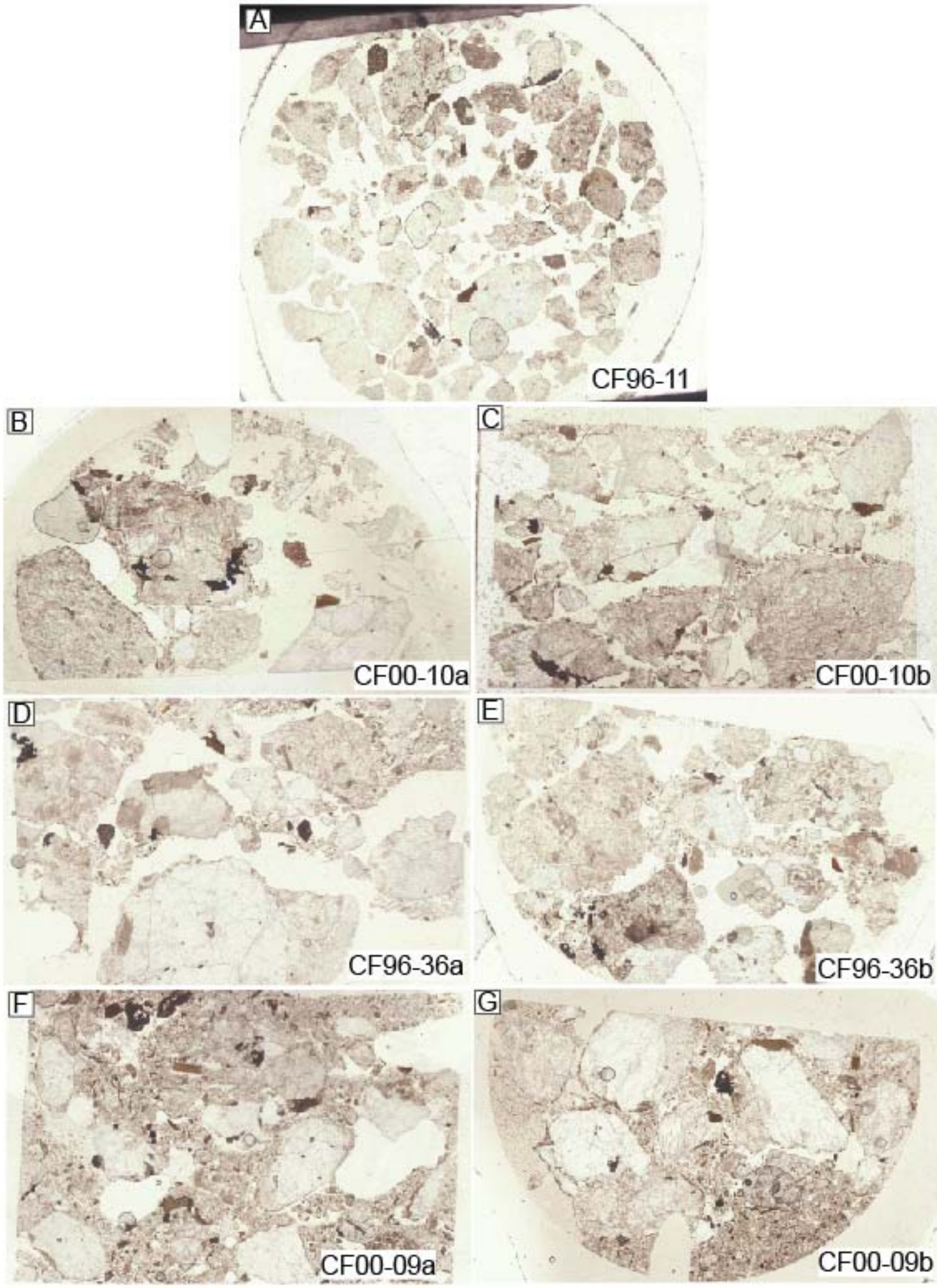

Figure A1.18. Thin section scans of the four samples in group *G*: (A) CF96-11 (B) CF00-10a (C) CF00-10b (D) CF96-36a (E) CF96-36b (F) CF00-09b (G) CF00-09b. Pucks = 2.5 cm.

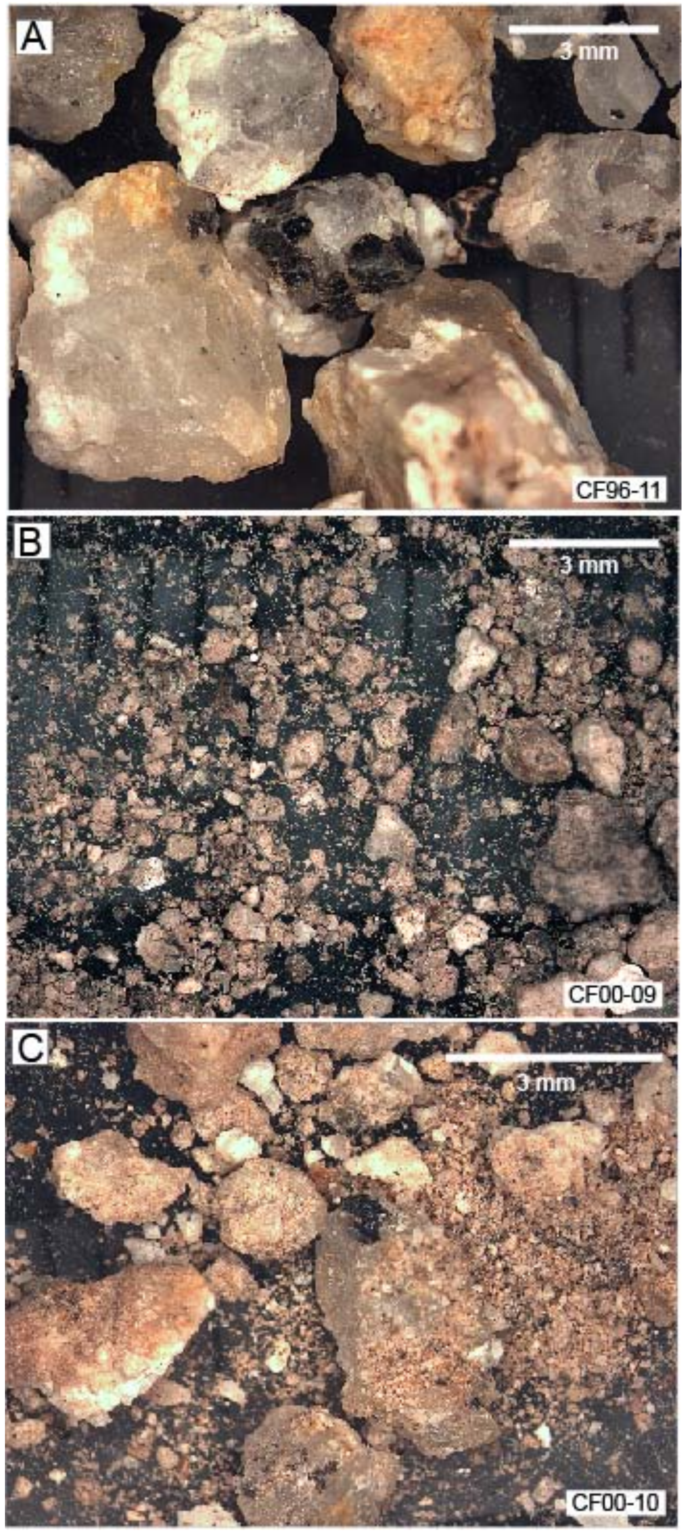

Figure A1.19. Loose sediment in group *G*. (A) CF96-36 (B) CF00-10 (C) CF00-09.

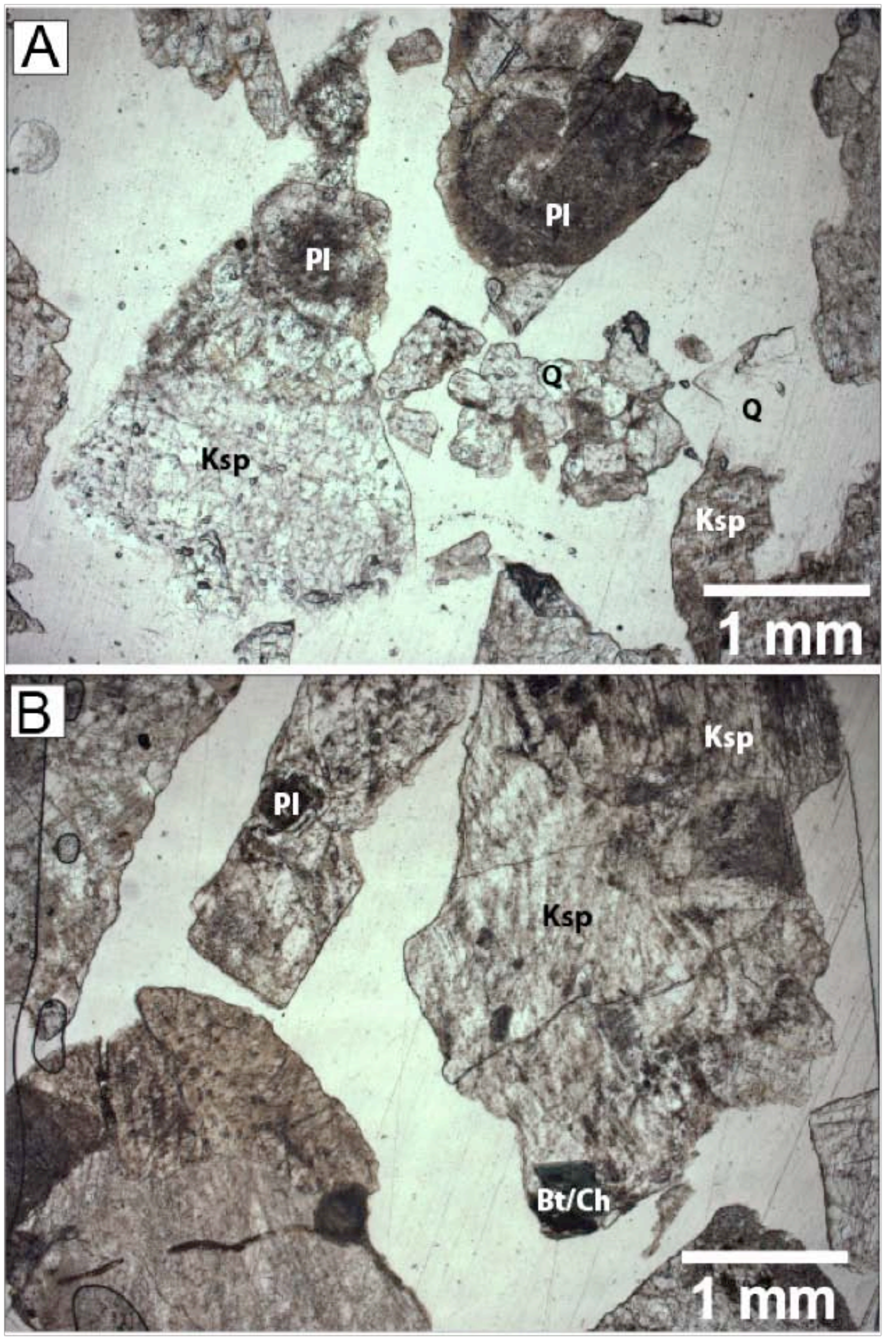

Figure A1.20. Plane light photomicrographs of group *G* sediment.

A1.4.2. Group VC sediment samples

Group *VC* includes sediment samples CF96-40, CF96-22, and CF00-07. Sample CF00-07 was collected in geomorphic zone II, while CF96-22 and CF96-40 were collected in zone IV (Fig. 1B). Texturally, about 60 % of sediments in each group *VC* sample are between -1 and 1 Φ (Fig. A1.21). All three samples relatively similar grain size distributions, and are apparent in thin section (Fig. A1.22) and loose sediment (Fig. A1.23).

Mineral phases present (Fig. A1.24): plagioclase (oligoclase), K-feldspar (perthite), quartz, biotite, apatite, zircon, chlorite, opaque oxides (magnetite-ilmenite), titantie, allanite, hematite, and calcite (present as caliche and as a secondary phase).

Rock fragments present (primary rock-forming mineral phases only): plagioclase-K-feldspar-quartz, plagioclase-K-feldspar-quartz-biotite, plagioclase-K-feldspar-biotite, plagioclase-quartz, plagioclase-K-feldspar, plagioclase-biotite, K-feldspar-quartz-biotite, and K-feldspar-biotite.

Associated/host-minerals for accessory phases (most common): zircon = plagioclase and biotite; apatite = biotite; chlorite = biotite; titanite = plagioclase, K-feldspar, quartz, biotite; and allanite = plagioclase.

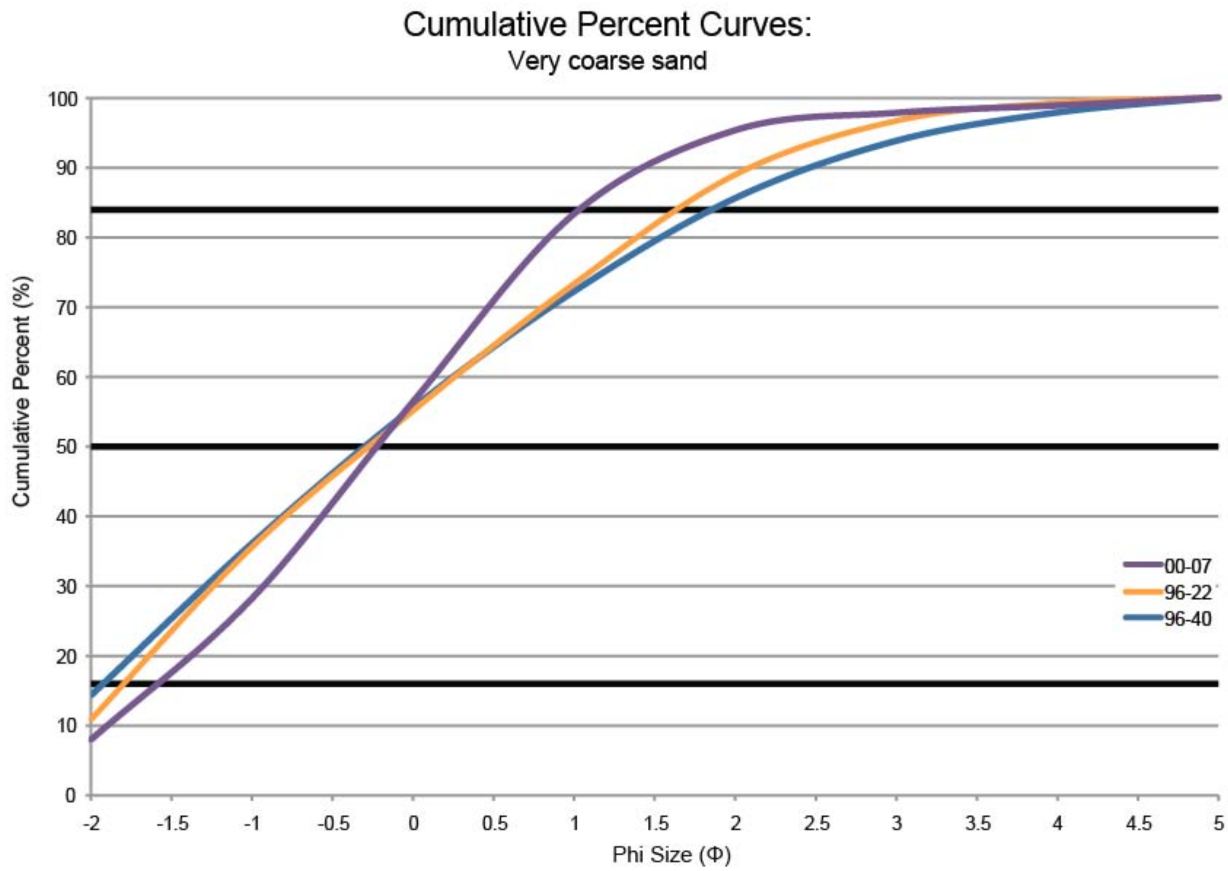

Figure A1.21. Cumulative percent grain-size distribution for group *VC* sediments.

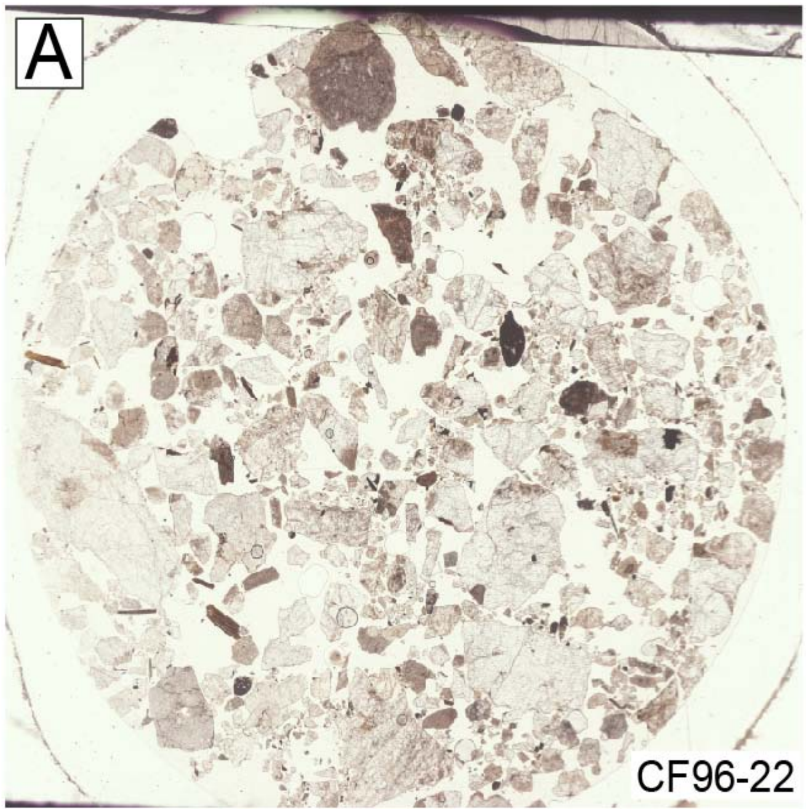

Figure A1.22. Thin section scans of the four samples in group *VC*: (A) CF96-22 {there are no thin section scans of CF96-40 not CF00-07). Puck = 2.5 cm.

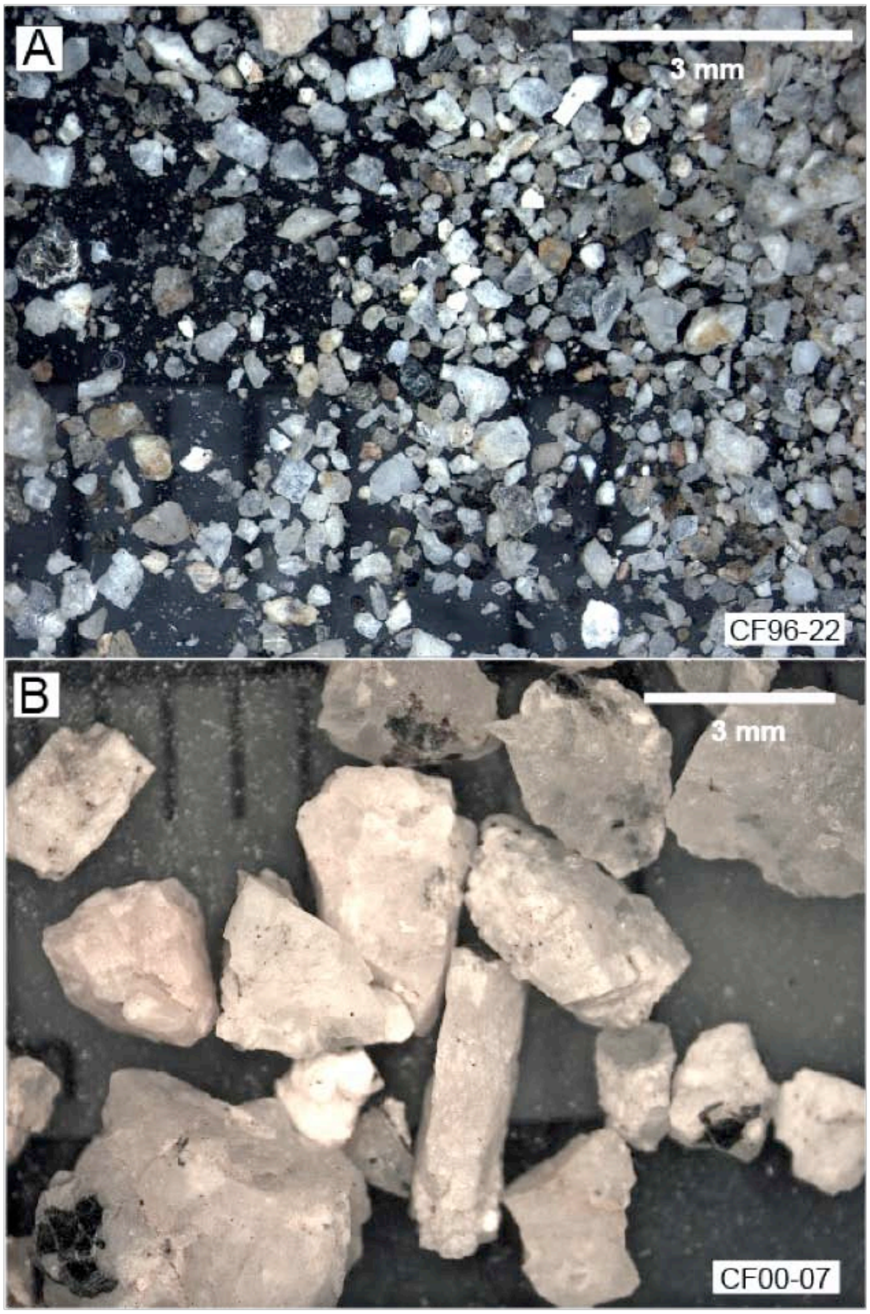

Figure A1.23. Loose sediment in group *VC*. (A) CF96-22 (B) CF00-07.

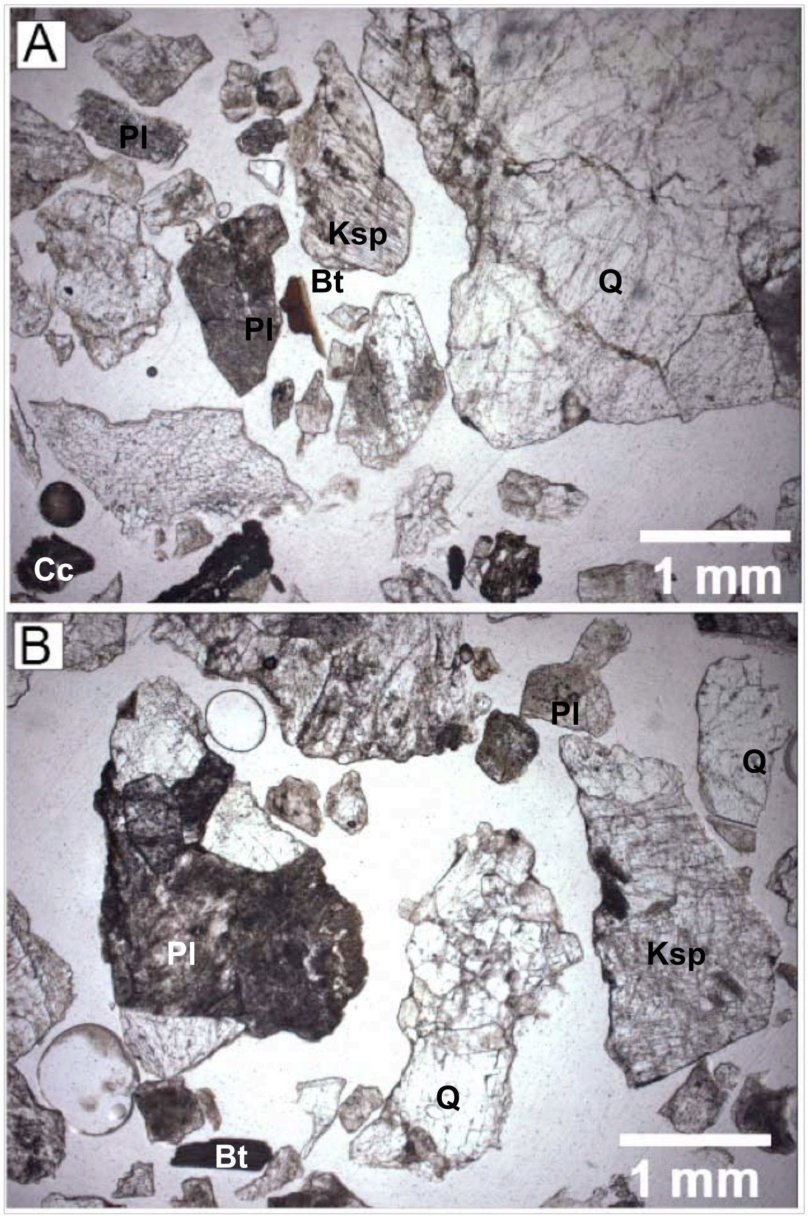

Figure A1.24. Plane light photomicrographs of group *VC* sediment.

A1.4.3. Group *C* sediment samples

Group *C* includes sediment samples CF96-12, CF96-15, CF96-19, CF96-20, CF96-26, and CF96-34. Sample CF96-12 was collected from geomorphic zone II; CF96-15, CF96-19, and CF96-20 were collected in zone III; CF96-34 was collected in zone IV (Fig. 1B). Texturally, more than 60 % of sediments in each group *C* sample are between -0 and 2 Φ (Fig. A1.25). All three samples have relatively similar grain size distributions, which are apparent in thin section (Fig. A1.26) and loose sediment (Fig. A1.27).

Mineral phases present (Fig. A1.28): plagioclase (oligoclase), K-feldspar (perthite), quartz, biotite, apatite, zircon, chlorite, opaque oxides (magnetite-ilmenite), titantie, allanite, hematite, and calcite (present as caliche and as a secondary phase).

Rock fragments present (primary rock-forming mineral phases only): plagioclase-K-feldspar-quartz, plagioclase-K-feldspar-quartz-biotite, plagioclase-K-feldspar-biotite, plagioclase-quartz, plagioclase-K-feldspar, plagioclase-biotite, K-feldspar-quartz-biotite, and K-feldspar-biotite.

Associated/host-minerals for accessory phases (most common): zircon = plagioclase and biotite; apatite = biotite; chlorite = biotite; titanite = plagioclase, K-feldspar, quartz, biotite; and allanite = plagioclase.

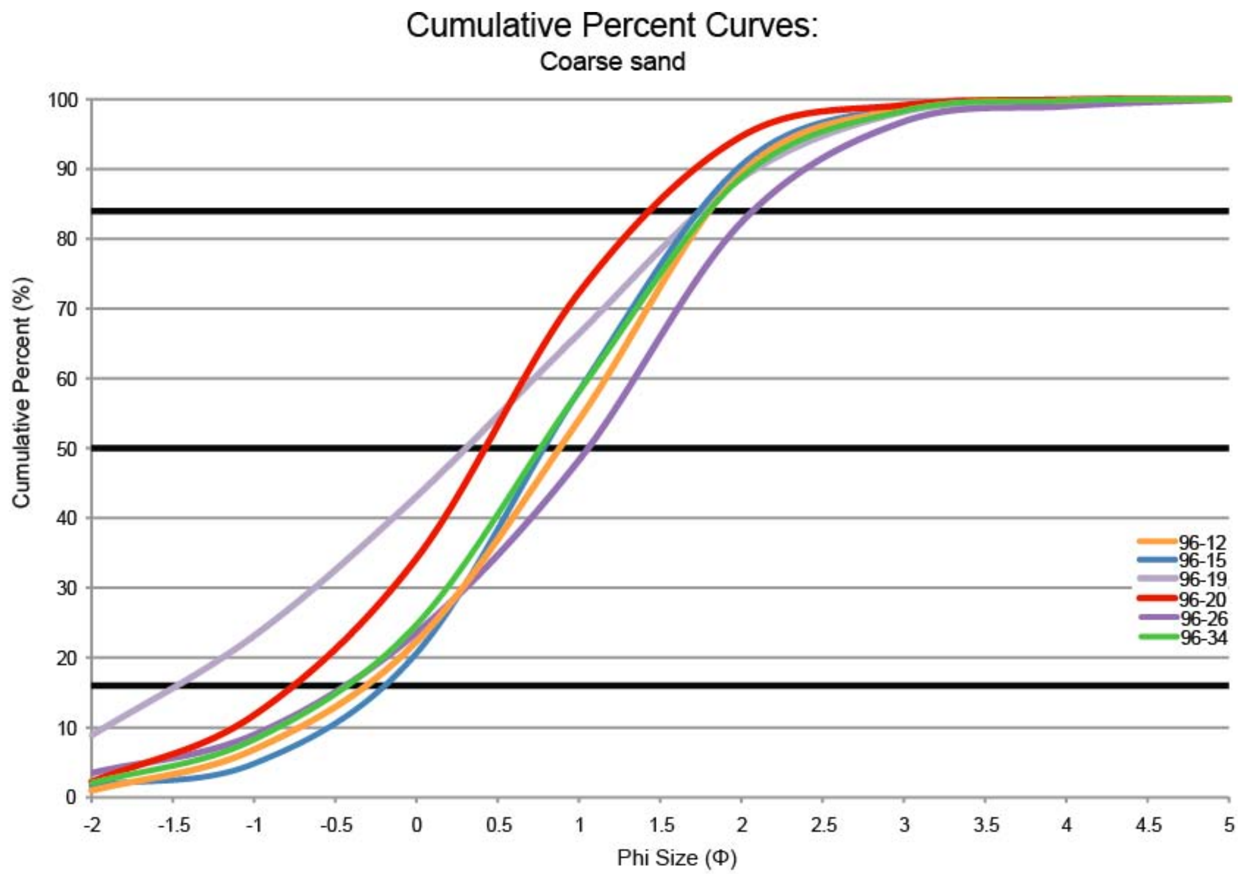

Figure A1.25. . Cumulative percent grain-size distribution for group *C* sediments.

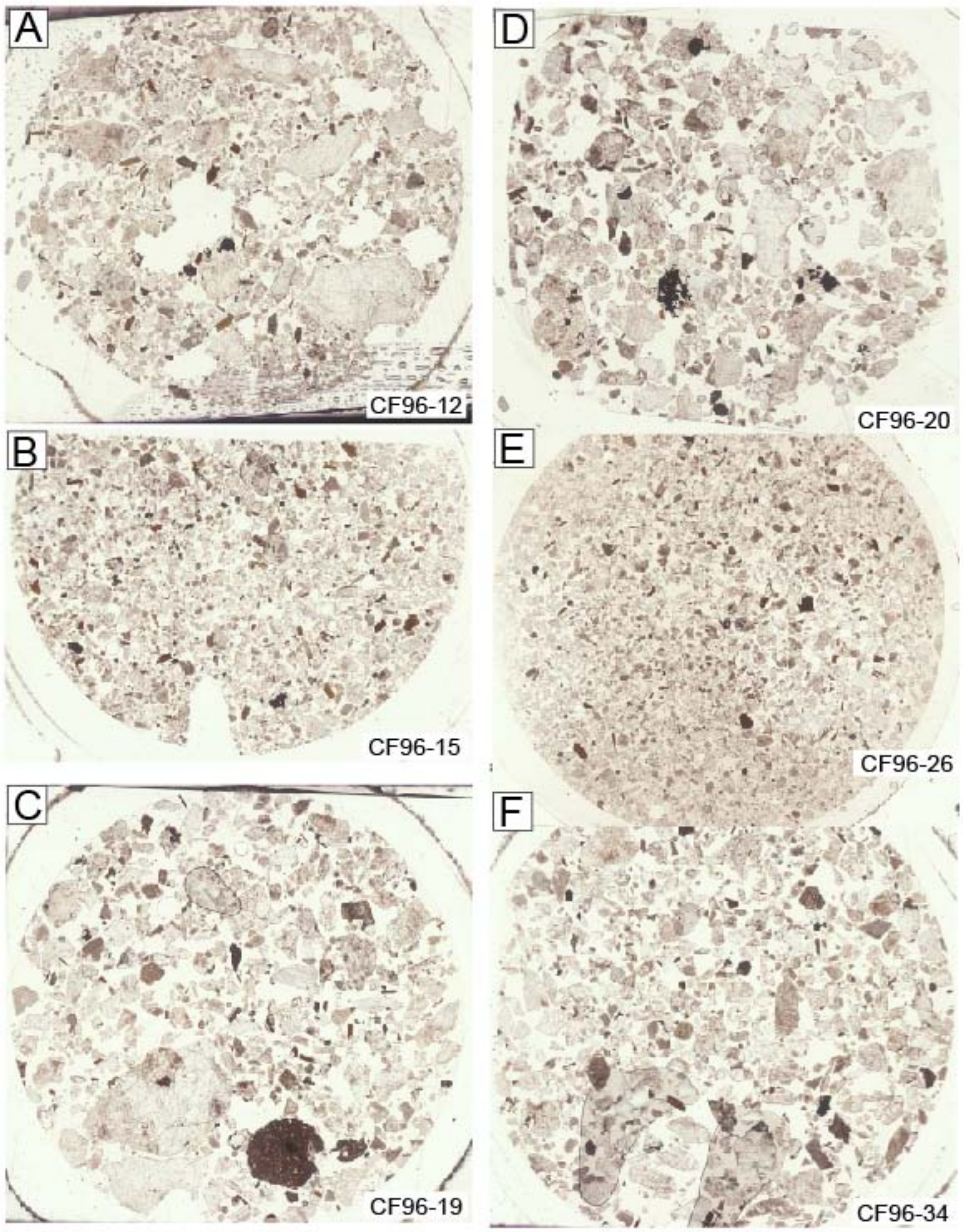

Figure A1.26. Thin section scans of the four samples in group *C*: (A) CF96-12 (B) CF96-15 (C) CF96-19 (D) CF96-20 (E) CF96-26 (F) CF96-34. Pucks = 2.5 cm.

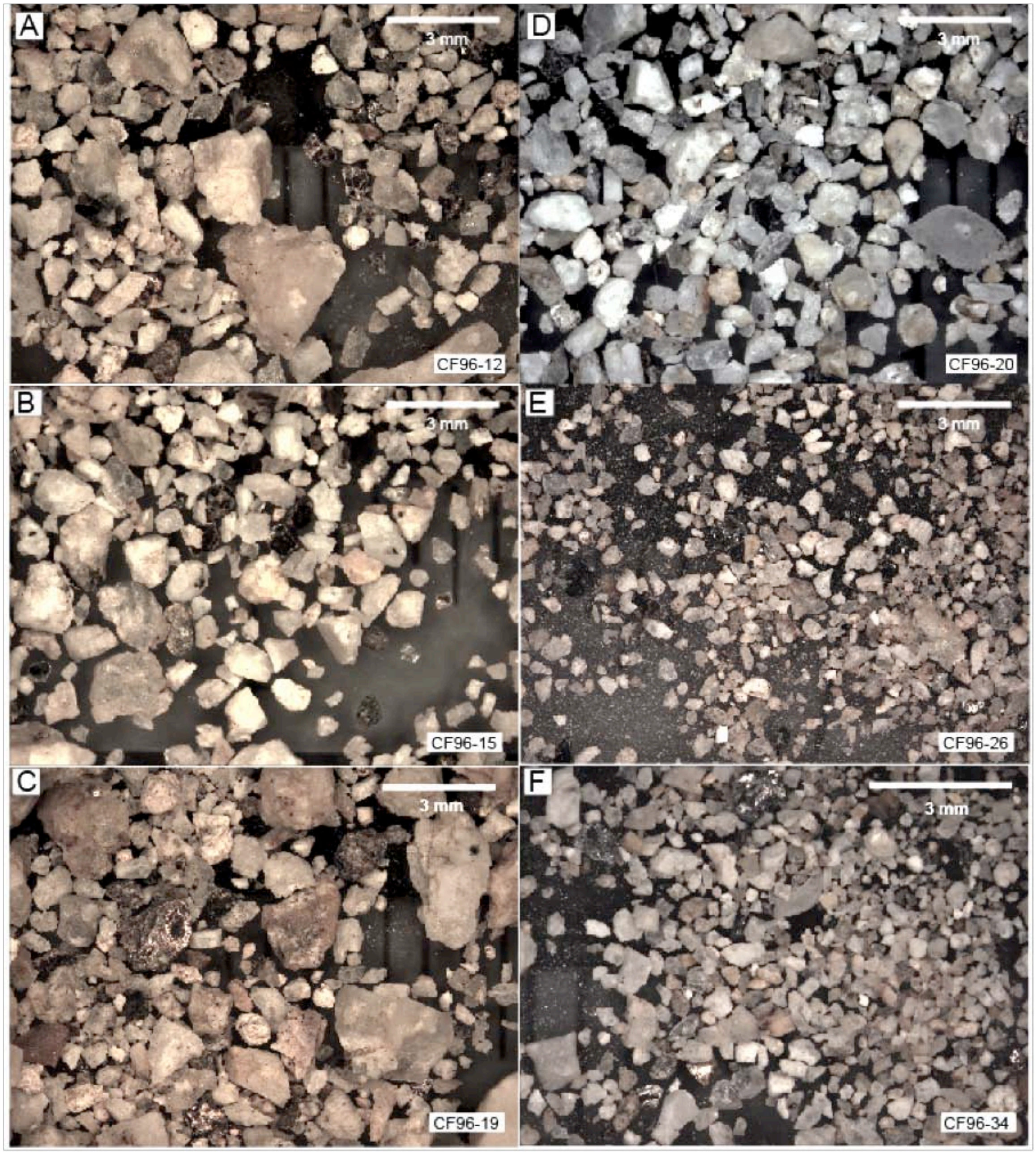

Figure A1.27. Loose sediment in group *C*. (A) CF96-12 (B) CF96-15 (C) CF96-19 (D) CF96-20 (E) CF96-26 (F) CF96-34.

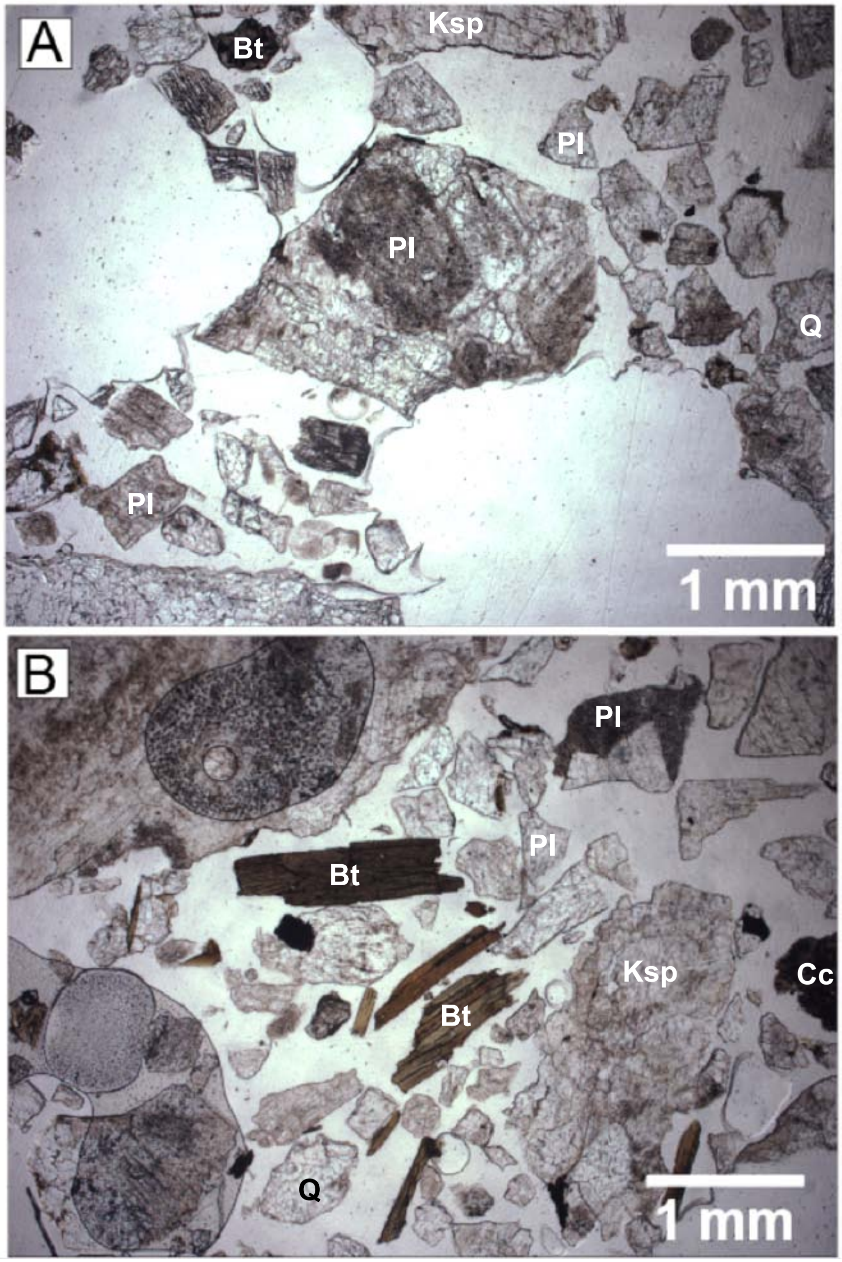

Figure A1.28. Plane light photomicrographs of group *C* sediment.

A1.4.4. Group *M* sediment samples

Group *M* includes sediment samples CF96-07, CF00-06, and CF00-17. Samples CF96-07 and CF00-06 were collected in zone II, while CF00-17 was collected in zone III (Fig. 1B). Texturally, at least 50 % (and up to ~80 %) of sediments in each group *M* sample are between 2 and 3 Φ (Fig. A1.29). All three samples relatively similar grain size distributions, and are apparent in thin section (Fig. A1.30) and loose sediment (Fig. A1.31).

Mineral phases present (Fig. A1.32): plagioclase (oligoclase), K-feldspar (perthite), quartz, biotite, apatite, zircon, chlorite, opaque oxides (magnetite-ilmenite), titantie, allanite, hematite, and calcite (present as caliche and as a secondary phase).

Rock fragments present (primary rock-forming mineral phases only): plagioclase-K-feldspar-quartz, plagioclase-K-feldspar-quartz-biotite, plagioclase-K-feldspar-biotite, plagioclase-quartz, plagioclase-K-feldspar, plagioclase-biotite, K-feldspar-quartz-biotite, and K-feldspar-biotite.

Associated/host-minerals for accessory phases (most common): zircon = plagioclase and biotite; apatite = biotite; chlorite = biotite; titanite = plagioclase, K-feldspar, quartz, biotite; and allanite = plagioclase.

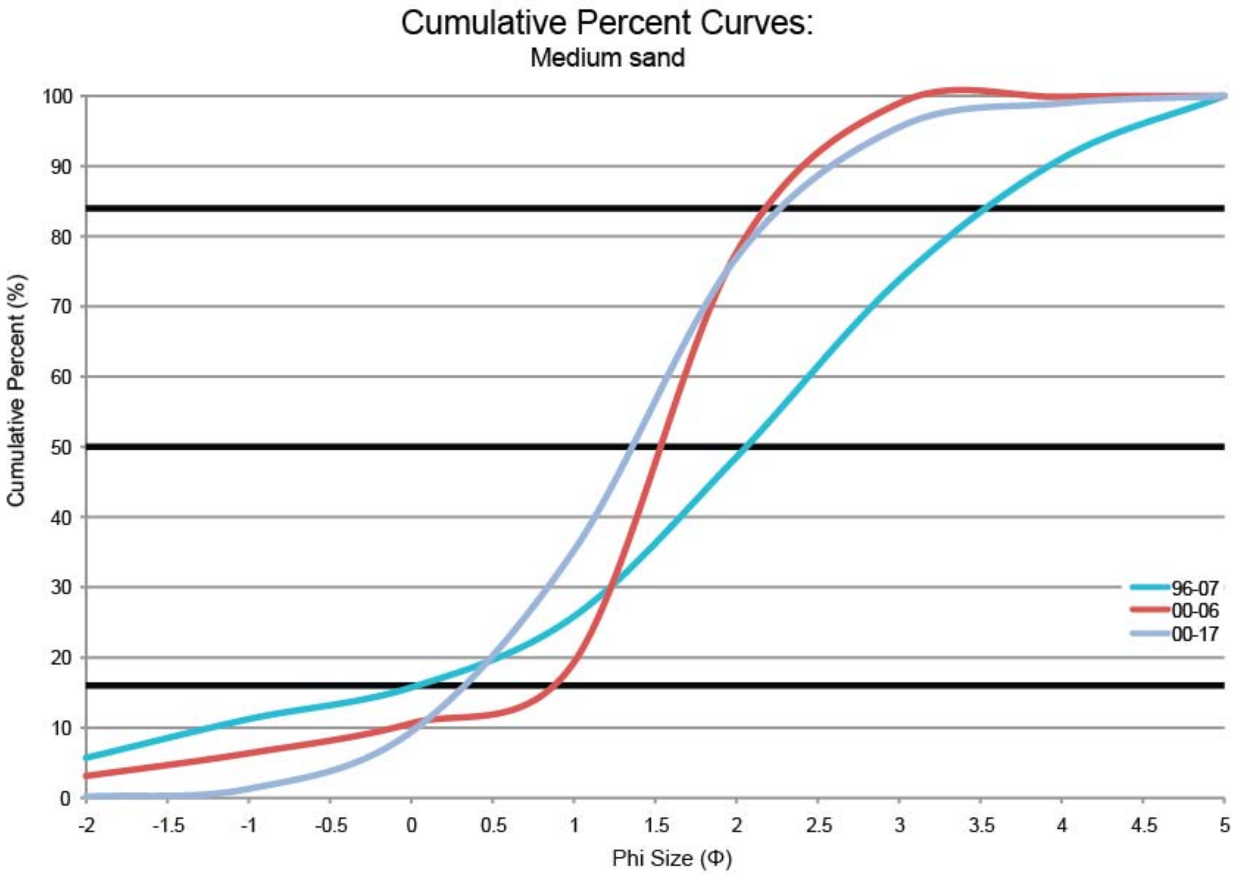

Figure A1.29. . Cumulative percent grain-size distribution for group *M* sediments.

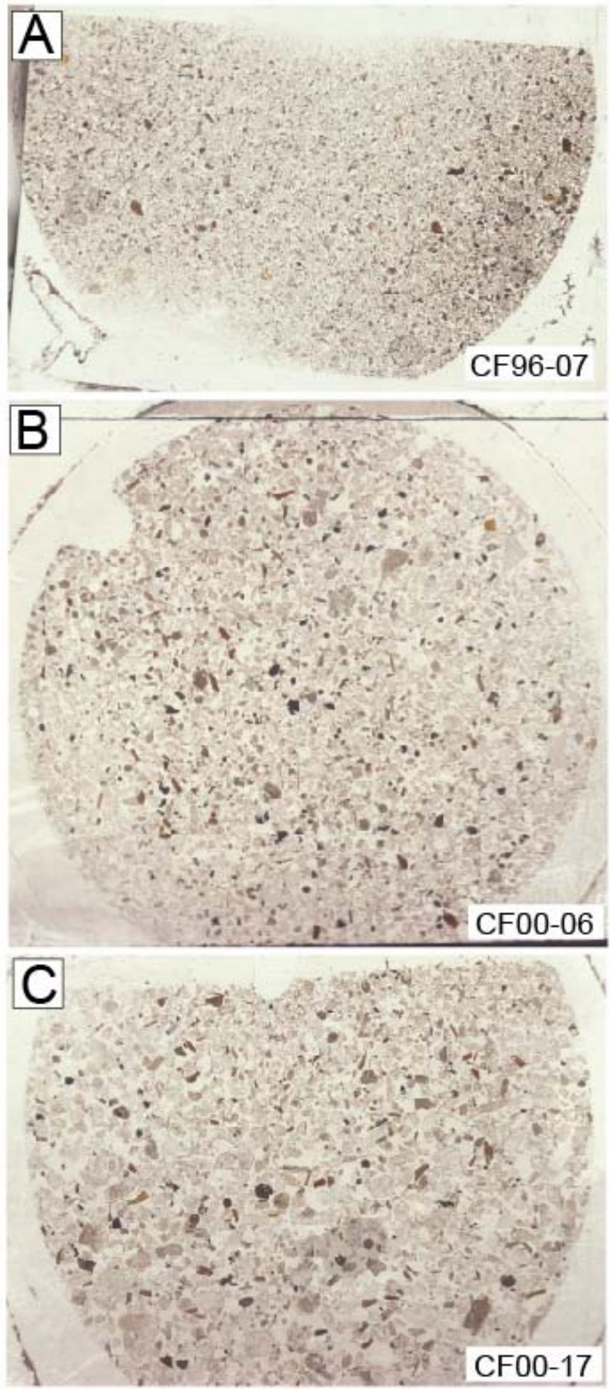

Figure A1.30. Thin section scans of the four samples in group *M*: (A) CF96-07 (B) CF00-06 (C) CF00-17. Pucks = 2.5 cm.

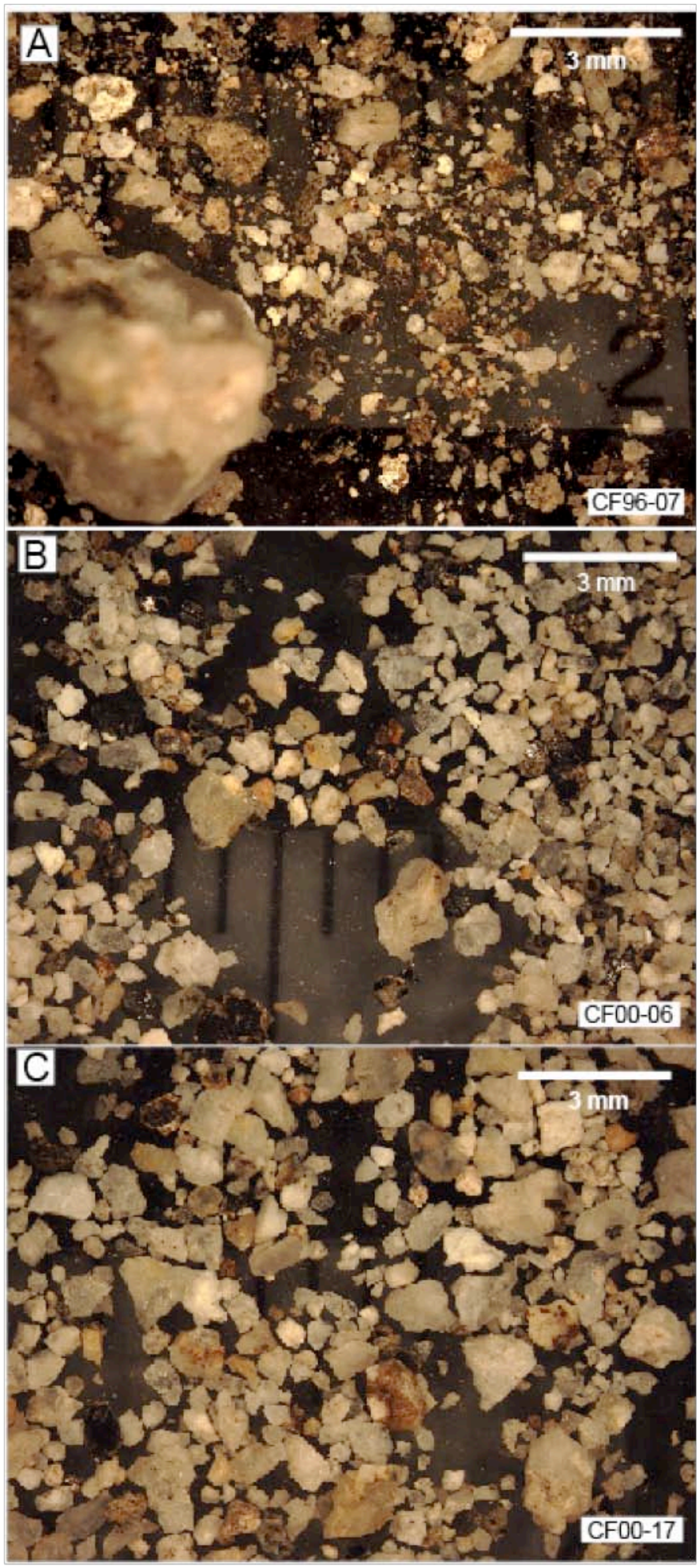

Figure A1.31. Loose sediment in group *M*. (A) CF96-07 (B) CF00-06 (C) CF00-17.

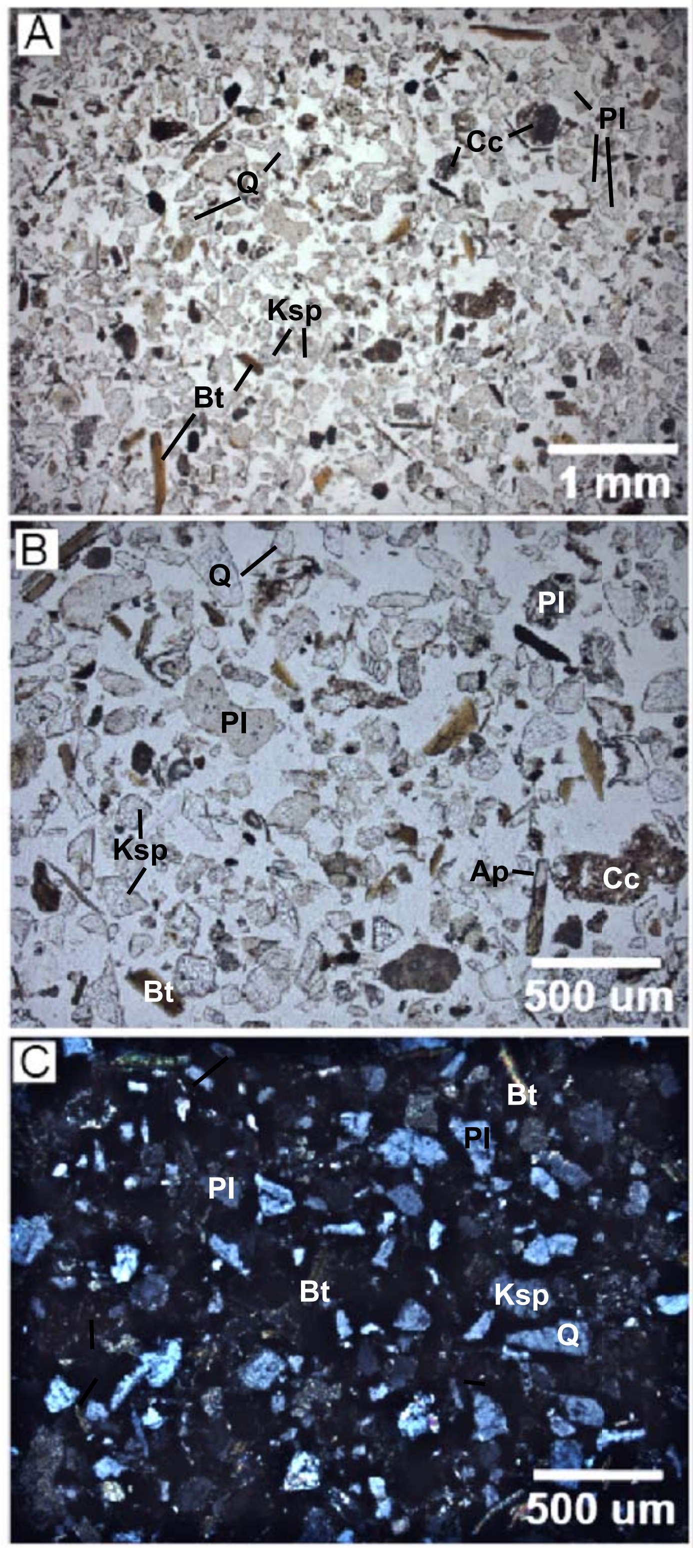

Figure A1.32. (A) and (B) Plane light (C) crossed polarized photomicrographs of group *M* sediment.

A1.4.5. Group *F* sediment samples

Group *F* includes sediment samples CF00-14, CF00-03, CF96-23, CF00-29, CF96-35, and CF96-39. Samples CF00-14 and CF00-03 were collected in zone II, while CF96-23, CF00-29, CF96-35, and CF96-39 were collected in zone IV (Fig. 1B). Texturally, about 70 % of sediments in each group *F* sample are between 2 and 5 Φ (Fig. A1.33). All three samples relatively similar grain size distributions, and are apparent in thin section (Fig. A1.34) and loose sediment (Fig. A1.35).

Mineral phases present (Fig. A1.36): plagioclase (oligoclase), K-feldspar (perthite), quartz, biotite, apatite, zircon, chlorite, opaque oxides (magnetite-ilmenite), titantie, allanite, hematite, and calcite (present as caliche and as a secondary phase).

Rock fragments present (primary rock-forming mineral phases only): plagioclase-K-feldspar-quartz, plagioclase-K-feldspar-quartz-biotite, plagioclase-K-feldspar-biotite, plagioclase-quartz, plagioclase-K-feldspar, plagioclase-biotite, K-feldspar-quartz-biotite, and K-feldspar-biotite.

Associated/host-minerals for accessory phases (most common): zircon = plagioclase and biotite; apatite = biotite; chlorite = biotite; titanite = plagioclase, K-feldspar, quartz, biotite; and allanite = plagioclase.

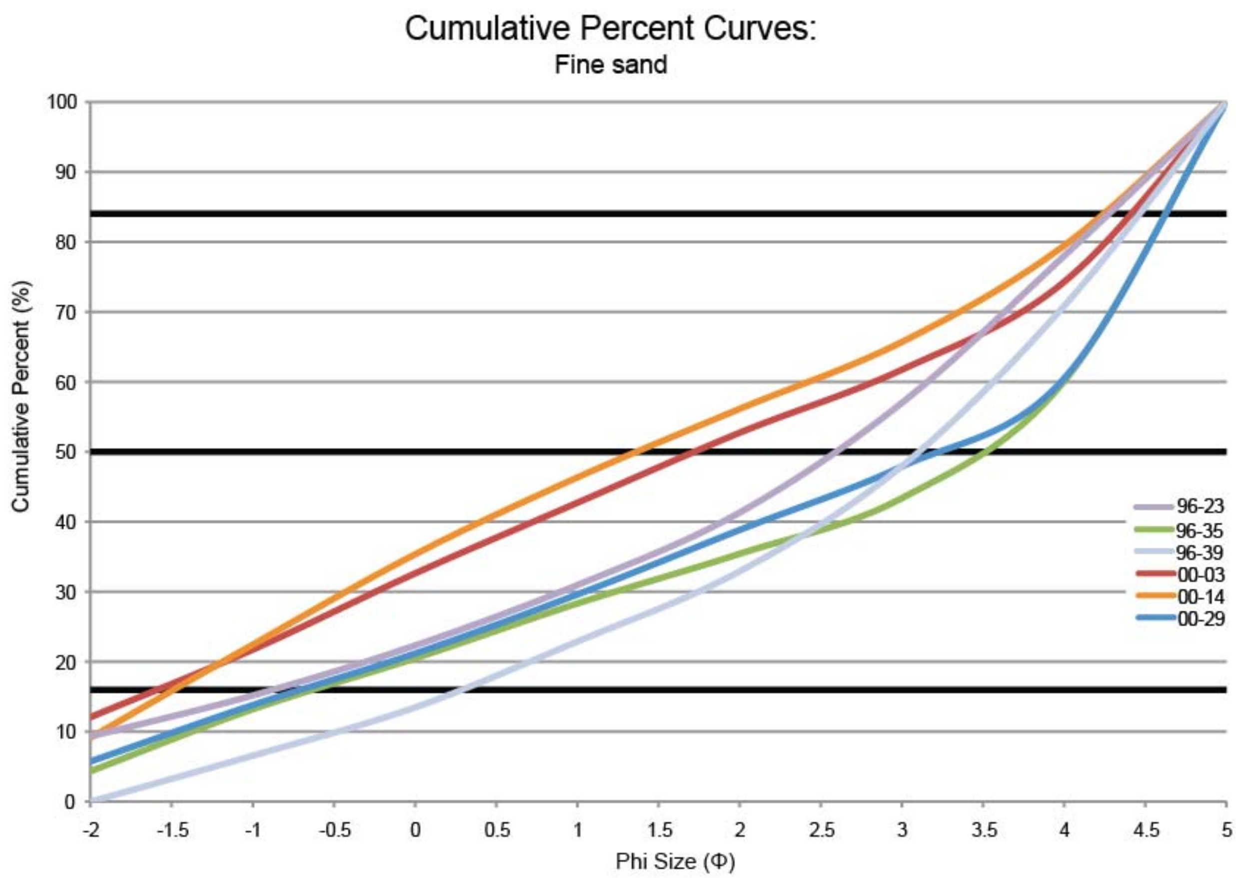

Figure A1.33. . Cumulative percent grain-size distribution for group *F* sediments.

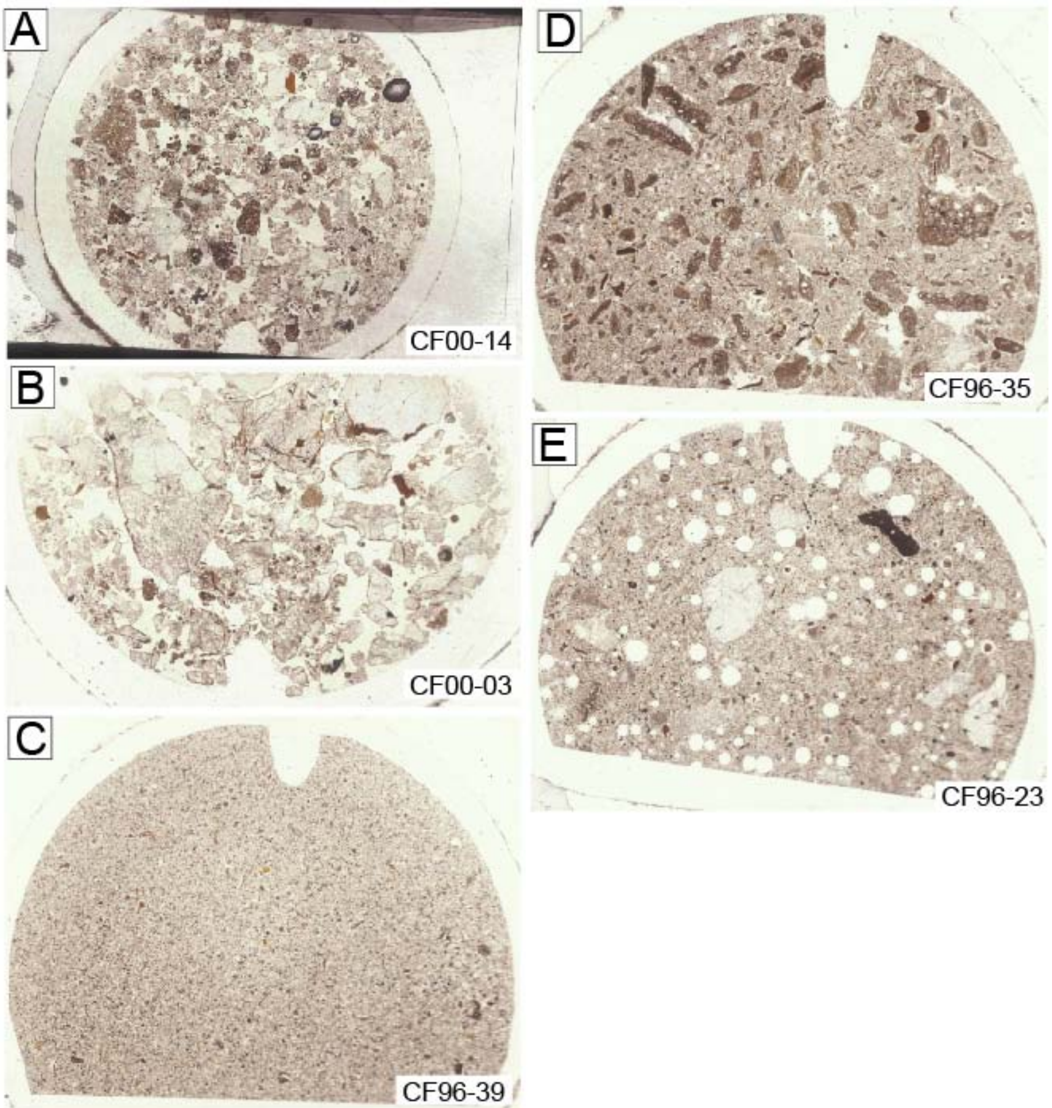

Figure A1.34. Thin section scans of the four samples in group *F*: (A) CF00-14 (B) CF00-03 (C) CF96-39 (D) CF96-35 (E) CF96-23. Pucks = 2.5 cm.

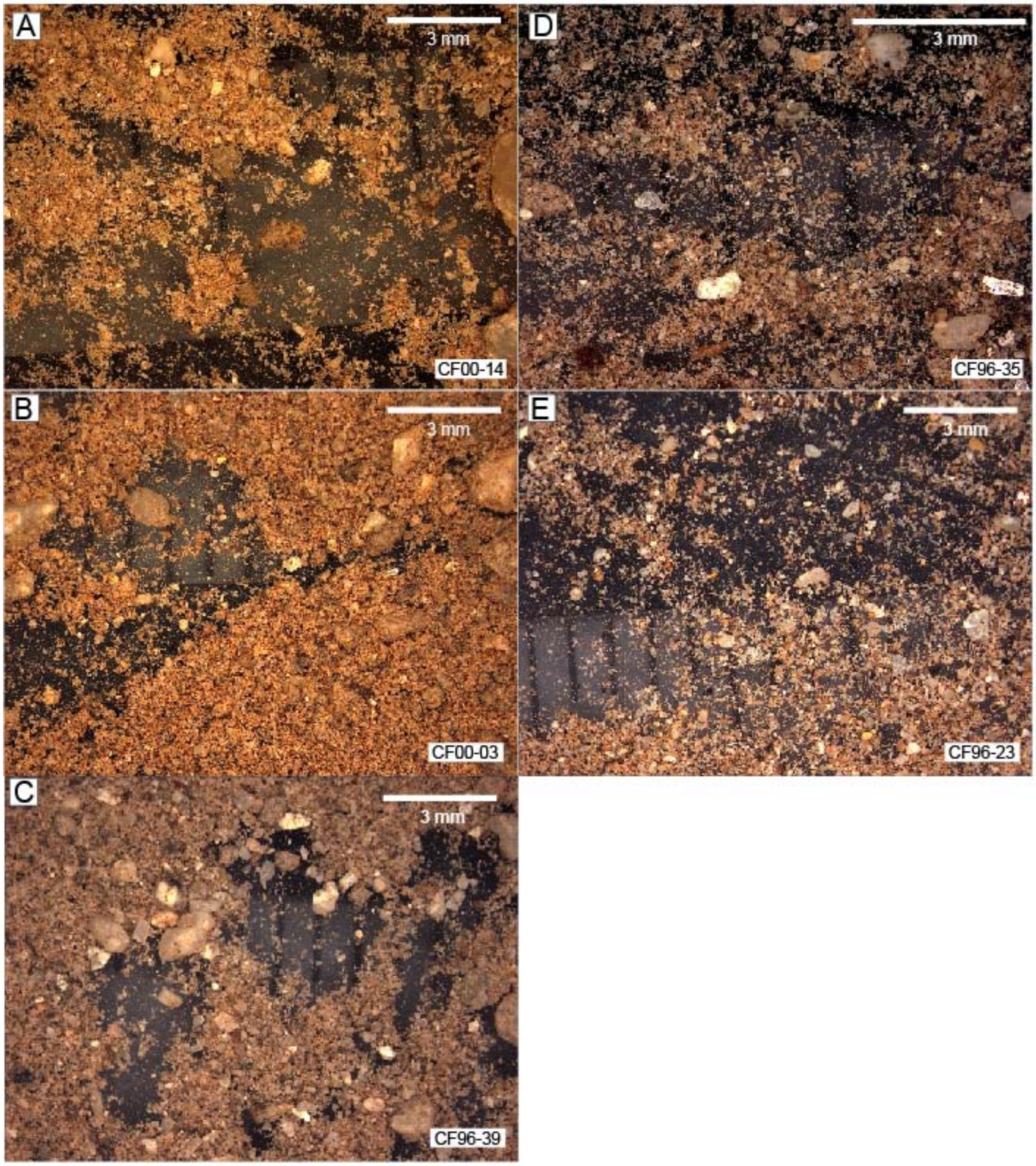

Figure A1.35. Loose sediment in group *F*. (A) CF00-14 (B) CF00-03 (C) CF96-39 (D) CF96-35 (E) CF96-23.

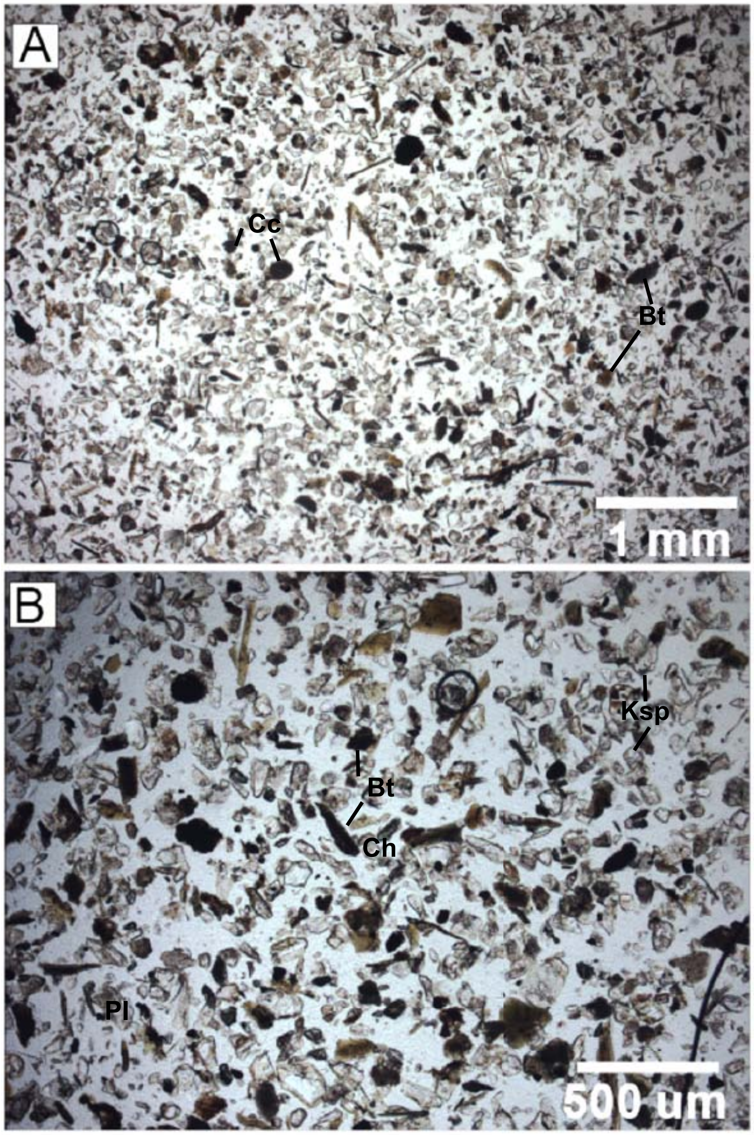

Figure A1.36. Plane light photomicrographs of group *F* sediments.

A1.4.6. Group V*F* sediment samples

Group *VF* includes sediment samples CF96-21 and CF96-10. Sample CF96-21 was collected in zone III, while CF96-10 was collected in zone II (Fig. 1B). Texturally, about 60 % of sediments in each group *VF* sample are greater than 4 Φ (Fig. A1.37). All three samples relatively similar grain size distributions, and are apparent in thin section (Fig. A1.38) and loose sediment (Fig. A1.39).

Mineral phases present (Fig. A1.40): plagioclase (oligoclase), K-feldspar (perthite), quartz, biotite, apatite, zircon, chlorite, opaque oxides (magnetite-ilmenite), titantie, allanite, hematite, and calcite (present as caliche and as a secondary phase).

Rock fragments present (primary rock-forming mineral phases only): plagioclase-K-feldspar-quartz, plagioclase-K-feldspar-quartz-biotite, plagioclase-K-feldspar-biotite, plagioclase-quartz, plagioclase-K-feldspar, plagioclase-biotite, K-feldspar-quartz-biotite, and K-feldspar-biotite.

Associated/host-minerals for accessory phases (most common): zircon = plagioclase and biotite; apatite = biotite; chlorite = biotite; titanite = plagioclase, K-feldspar, quartz, biotite; and allanite = plagioclase.

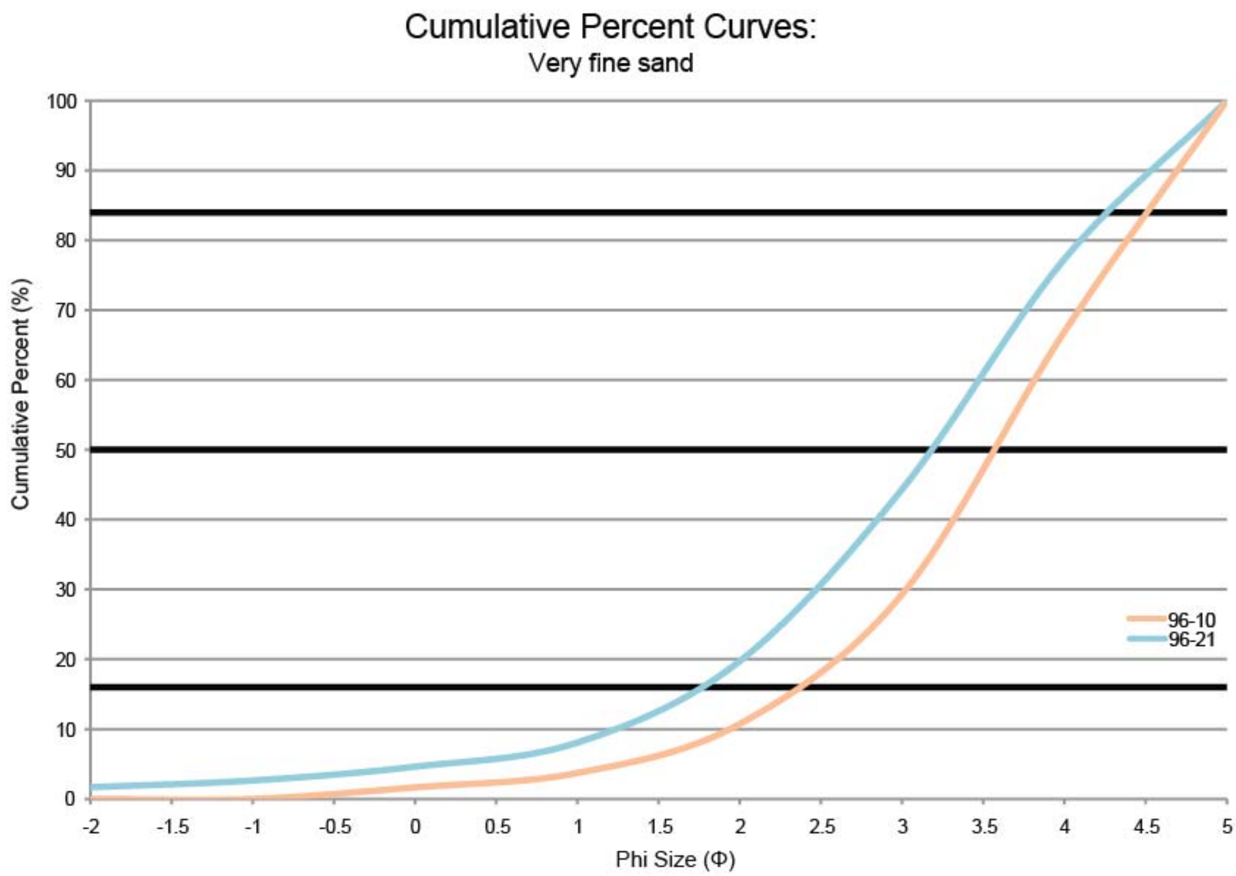

Figure A1.37. . Cumulative percent grain-size distribution for group *V*F sediments.

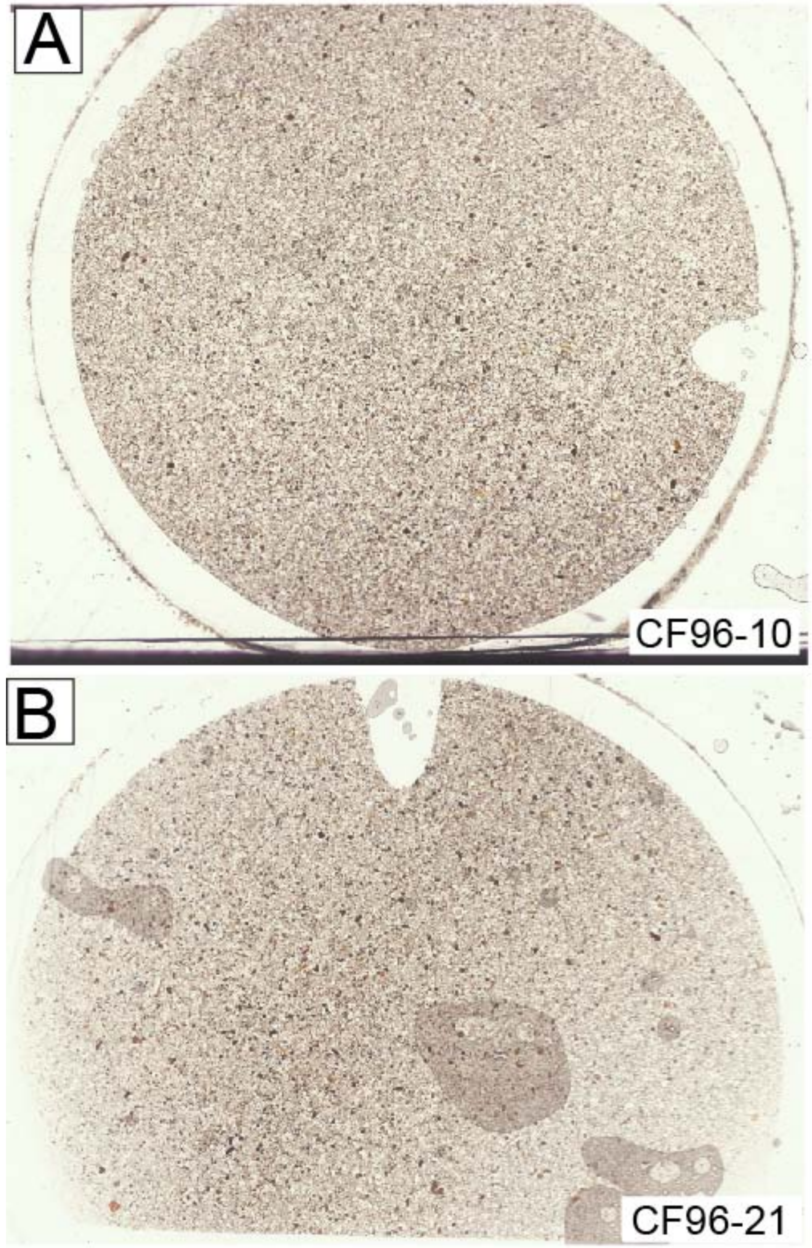

Figure A1.38. Thin section scans of the four samples in group *VF*: (A) CF96-10 (B) CF96-21. Pucks = 2.5 cm.

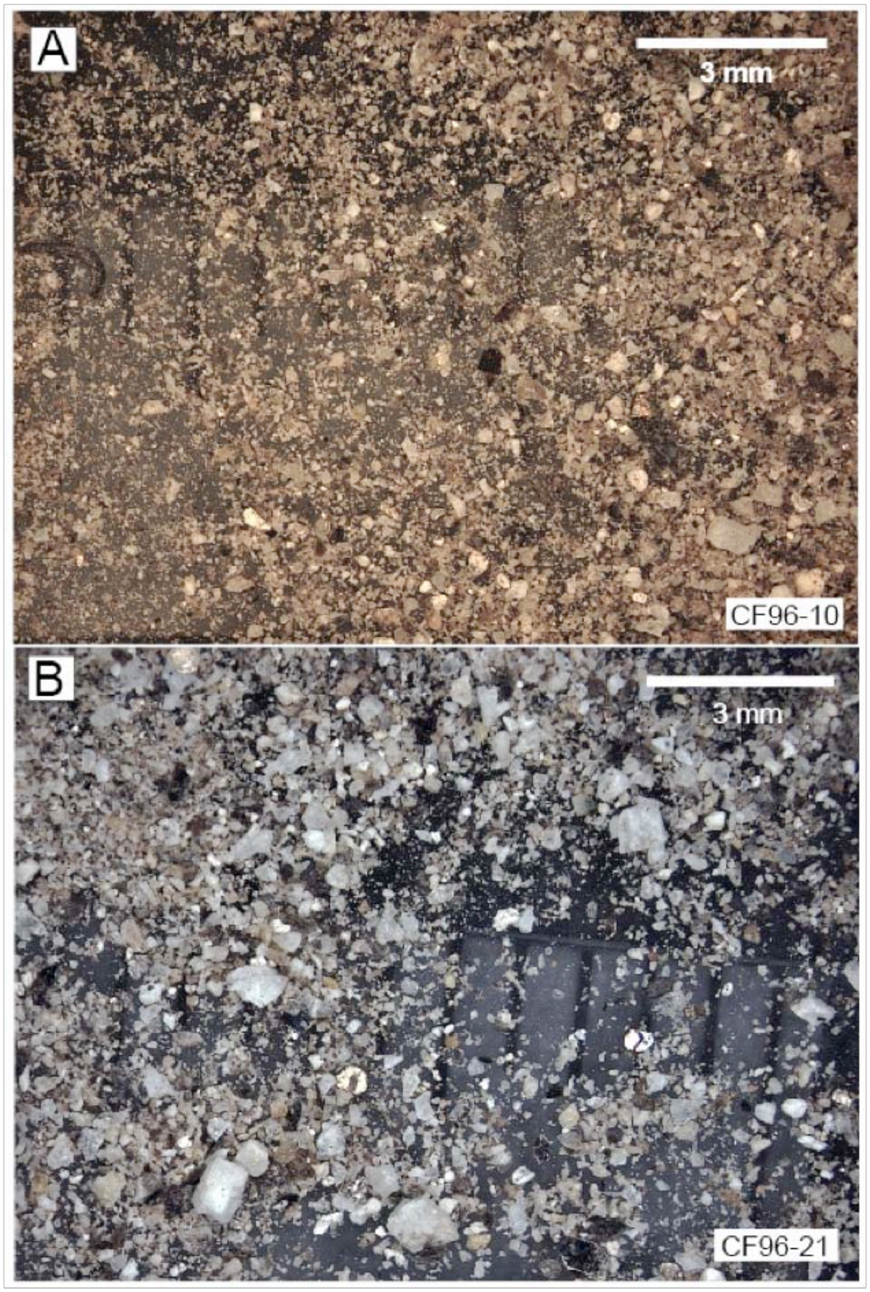

Figure A1.39. Loose sediment in group *VF*. (A) CF96-10 (B) CF96-21.

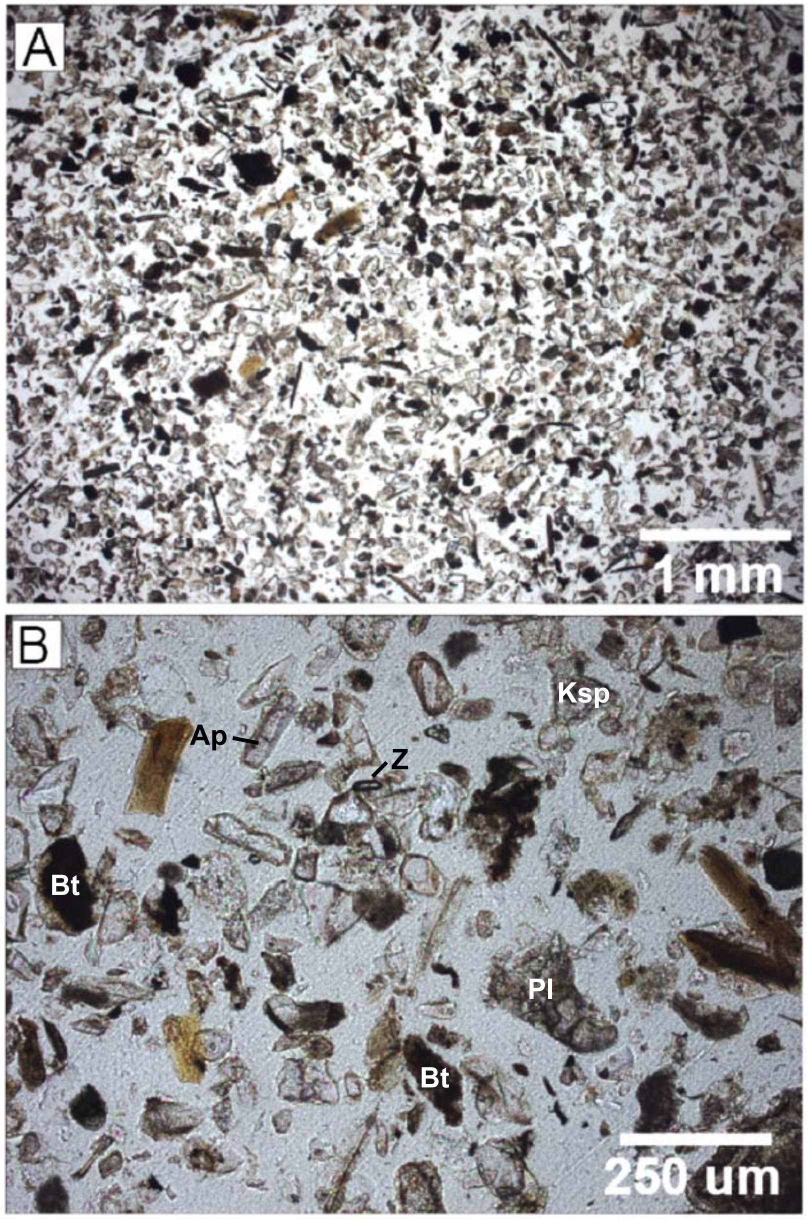

Figure A1.40. Plane light photomicrographs of group *VF* sediment.

Appendix 2:

Supplementary geochemical material

The following appendix contains the geochemical provenance plots not included in the main text. Figures A2.1 to A2.6 are plots where some plots have the sediment data grouped by geomorphic zone (rather than grain-size). These plots were not discussed in the main text because of the lack of compositional control the geomorphic zones had on the sediments. The figures are presented in the same order as they are in the text.

Table A2.1. Major oxide ratios of Stepladder samples.

Sample	Na_2O/K_2O	SiO_2/Al_2O_3	Fe_2O_3/SiO_2	Al_2O_3/SiO_2	A/CNK
Fresh Bedrock					
ST09-02	1.31	4.60	0.03	0.22	1.47
CF00-18	1.35	4.76	0.02	0.21	1.45
CF96-4	1.01	4.66	0.02	0.21	1.47
CF96-8	1.31	5.00	0.02	0.20	1.52
Avg	*1.23*	*4.75*	*0.02*	*0.21*	*1.48*
Regolith					
CF00-04	1.03	4.92	0.03	0.20	1.43
CF00-05	1.08	5.09	0.02	0.20	1.45
Avg	*1.05*	*5.01*	*0.02*	*0.20*	*1.44*
Grus					
CF96-01	0.89	4.89	0.04	0.20	1.60
Gravel Group (G)					
CF96-11	0.87	6.00	0.02	0.17	1.39
CF00-10	0.83	5.92	0.02	0.17	1.38
CF96-36	1.02	5.32	0.02	0.19	1.36
CF00-09	1.29	4.57	0.04	0.22	1.51
Avg	*0.99*	*5.41*	*0.03*	*0.18*	*1.41*
Very Coarse Sand Group (VC)					
CF96-40	0.98	5.69	0.05	0.18	1.43
CF96-22	1.28	4.82	0.03	0.21	1.35
CF00-07	0.99	5.66	0.02	0.18	1.39
Avg	*1.08*	*5.37*	*0.03*	*0.19*	*1.39*
Coarse Sand Group (C)					
CF96-19	1.35	4.05	0.02	0.25	1.34
CF96-12	1.43	4.26	0.03	0.23	1.45
CF96-15	1.57	4.15	0.03	0.24	1.43
CF96-34	1.53	4.54	0.02	0.22	1.47
CF96-20	1.24	4.59	0.02	0.22	1.42
CF96-26	1.53	4.24	0.02	0.24	1.47
Avg	*1.44*	*4.30*	*0.02*	*0.23*	*1.43*
Medium Sand Group (M)					
CF00-17	1.75	3.91	0.04	0.26	1.44
CF00-06	1.78	4.10	0.08	0.24	1.38
CF96-07	1.49	3.86	0.06	0.26	1.38
Avg	*1.67*	*3.96*	*0.06*	*0.25*	*1.40*
Fine Sand Group (F)					
CF00-14	1.00	4.89	0.04	0.20	1.19
CF00-03	1.16	4.43	0.05	0.23	1.60
CF96-23	1.24	4.46	0.05	0.22	1.34
CF00-29	0.97	5.13	0.04	0.19	1.46
CF96-35	0.97	4.44	0.05	0.23	1.42
CF96-39	1.15	4.60	0.06	0.22	1.49
Avg	*1.08*	*4.65*	*0.05*	*0.22*	*1.41*
Very Fine Sand Group (VF)					
CF96-21	1.49	4.01	0.05	0.25	1.41
CF96-10	1.30	4.04	0.06	0.25	1.42
Avg	*1.40*	*4.03*	*0.06*	*0.25*	*1.42*

Table A2.2. Trace element ratios of average Stepladder samples (bedrock, regolith, grus, and the six grain-size groups) and select reference rock compositions.

Average Ratios	La/Th	Nb/Ta	Zr/Hf	Y/Ho	La/Sc	Th/Sc	La/Co	Th/Co	Eu/Sm	La/Lu	Ba/Co	Th/Co
Bedrock	3.3	15.7	36.0	32.1	35.0	7.2	17.9	5.4	0.3	307.1	612.4	5.4
Regolith	3.6	15.0	35.8	26.3	36.8	10.0	17.6	4.9	0.3	335.7	649.3	4.9
Grus	2.0	14.6	37.0	26.0	12.8	6.4	12.4	6.2	0.1	208.1	204.4	6.2
Gravel Group (G)	2.8	15.6	36.9	26.4	10.3	9.0	9.7	3.4	0.2	179.1	347.3	3.4
Very Coarse Sand Group (VC)	2.7	13.1	36.6	27.5	24.0	10.8	16.2	6.0	0.2	206.9	407.7	6.0
Coarse Sand Group (C)	2.5	13.7	35.8	27.6	9.8	6.6	6.4	2.6	0.2	190.6	275.8	2.6
Medium Sand Group (M)	2.7	13.4	36.2	26.6	19.2	19.9	13.0	4.9	0.2	193.9	131.8	4.9
Fine Sand Group (F)	2.8	14.7	38.9	26.5	8.8	16.3	7.9	2.8	0.2	120.8	150.5	2.8
Very Fine Sand Group (VF)	3.0	15.3	38.5	26.7	8.8	19.5	7.5	2.5	0.2	134.3	93.5	2.5
PAAS[a]	2.6	15.8	42.0	27.2	2.4	0.9	1.7	0.6	0.2	87.8	28.3	0.6
Mesozoic-Cenozoic Granite[b]	2.7	12.5	39.1	--	2.2	0.8	4.7	1.7	0.2	35.9	141.7	1.7
Mesozoic-Cenozoic Andesite[b]	5.0	16.0	40.0	--	1.1	0.2	0.9	0.2	0.3	64.5	29.5	0.2
Mesozoic-Cenozoic Basalt[b]	4.6	21.7	38.5	--	0.3	0.1	0.3	0.1	0.4	25.6	11.7	0.1
Phanerozoic TTG[b]	2.5	12.3	33.3	--	1.8	0.7	1.8	0.7	0.2	89.3	57.1	0.7

[a] Compositions from McLennan (1989)
[b] Compositions from Condie (1993)

Table A2.2. *(cont.)*

Average Ratios	Ba/Sc	Rb/Sr	Zr/Sc	Th/U	Ba/Rb	Zr/Y	Ti/Zr	Zr/Nb	La/Th	Ni/Co	Cr/V	V/Ni	Cr/Zr
Bedrock	1199.2	0.1	274.3	22.9	16.7	27.6	11.1	23.0	3.3	0.7	0.1	26.4	--
Regolith	1347.4	0.2	238.4	14.8	11.8	28.9	11.8	23.3	3.6	0.7	0.1	20.3	--
Grus	211.3	0.2	82.2	15.7	12.8	19.7	11.0	22.6	2.0	1.9	0.4	6.0	0.1
Gravel Group (G)	370.7	0.2	96.9	9.7	11.6	25.9	10.6	23.0	2.8	1.4	0.3	8.0	--
Very Coarse Sand Group (VC)	602.0	0.2	180.8	11.1	12.6	24.4	11.1	20.7	2.7	1.6	0.2	11.5	--
Coarse Sand Group (C)	424.0	0.2	89.5	5.9	10.3	25.3	14.3	14.3	2.5	1.7	0.4	4.3	--
Medium Sand Group (M)	194.7	0.1	131.7	14.6	17.4	18.3	14.2	16.8	2.7	2.3	0.4	5.8	0.1
Fine Sand Group (F)	167.0	0.2	80.9	8.3	14.5	17.9	9.5	25.6	2.8	2.0	0.5	4.9	0.1
Very Fine Sand Group (VF)	110.5	0.2	69.7	8.8	13.5	16.3	9.6	24.3	3.0	2.0	0.6	3.9	0.1
PAAS[a]	40.6	0.8	13.1	4.7	4.1	7.8	47.6	11.1	2.6	2.4	0.7	2.7	0.5
Mesozoic-Cenozoic Granite[b]	65.4	0.8	16.5	4.1	6.5	6.5	15.8	10.8	2.7	1.3	0.2	3.8	--
Mesozoic-Cenozoic Andesite[b]	36.1	0.1	8.9	2.0	15.9	8.0	48.8	20.0	5.0	1.9	0.3	3.3	0.3
Mesozoic-Cenozoic Basalt[b]	12.4	0.1	4.0	2.0	14.1	4.9	110.7	26.2	4.6	1.9	0.6	3.8	1.1
Phanerozoic TTG[b]	57.1	0.3	10.0	4.0	8.9	5.6	39.3	17.5	2.5	1.1	0.4	5.3	0.2

[a] Compositions from McLennan (1989)
[b] Compositions from Condie (1993)

Table A2.3. Normative mineralogy of the four bedrick samples and average Stepladder bedrock.

Sample	CF09-02	CF00-18	CF96-04	CF96-08	BRavg
Normative mineralogy					
Quartz	23.43	25.44	25.25	29.79	25.98
Plagioclase	50.29	49.58	45.70	46.45	48.01
Orthoclase	23.15	21.75	26.18	21.07	23.04
Corundum	--	--	0.18	0.29	0.12
Diopside	0.16	0.59	--	--	0.19
Hypersthene	1.69	1.77	1.83	1.68	1.74
Ilmenite	0.62	0.28	0.27	0.23	0.35
Magnetite	0.43	0.37	0.39	0.33	0.38
Apatite	0.21	0.19	0.19	0.15	0.19
Zircon	0.02	0.03	0.01	0.01	0.02
Total	100.00	100.00	100.00	100.00	100.00

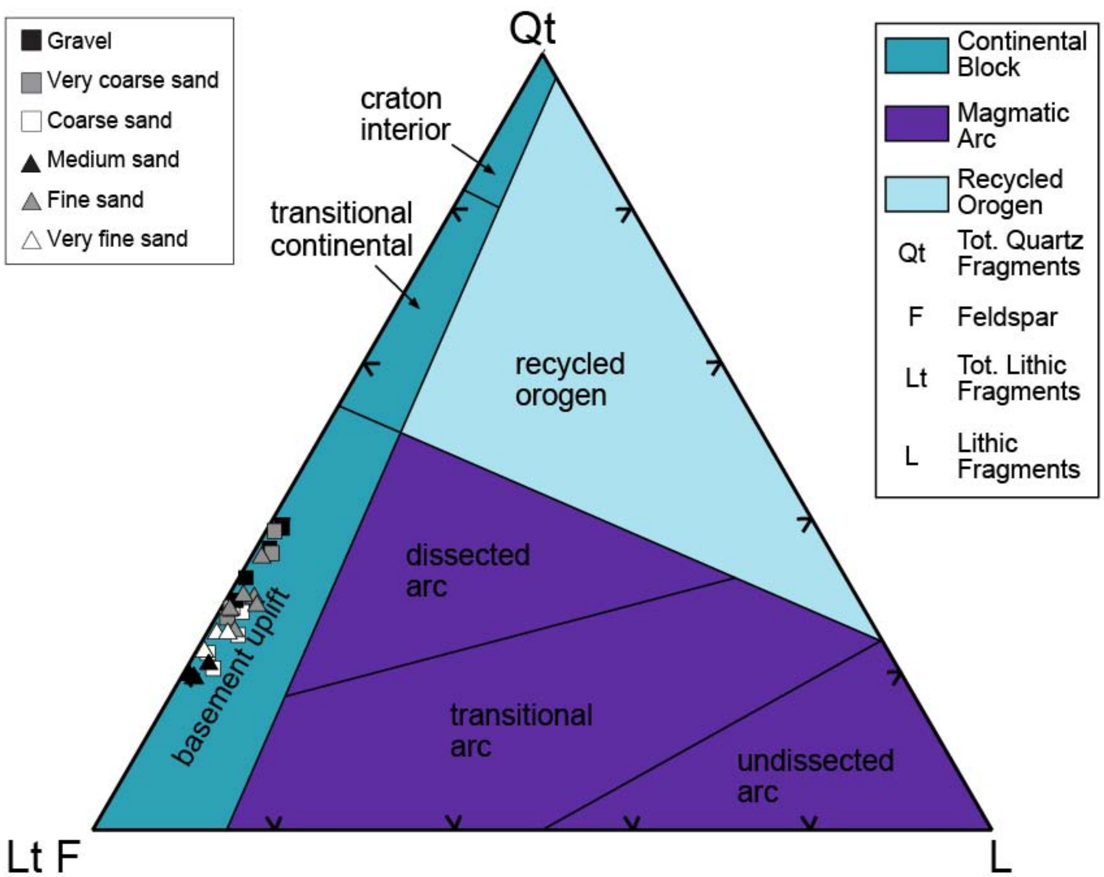

Figure A2.1. QFL diagram with all Stepladder sediments plotting in the basement uplift field.

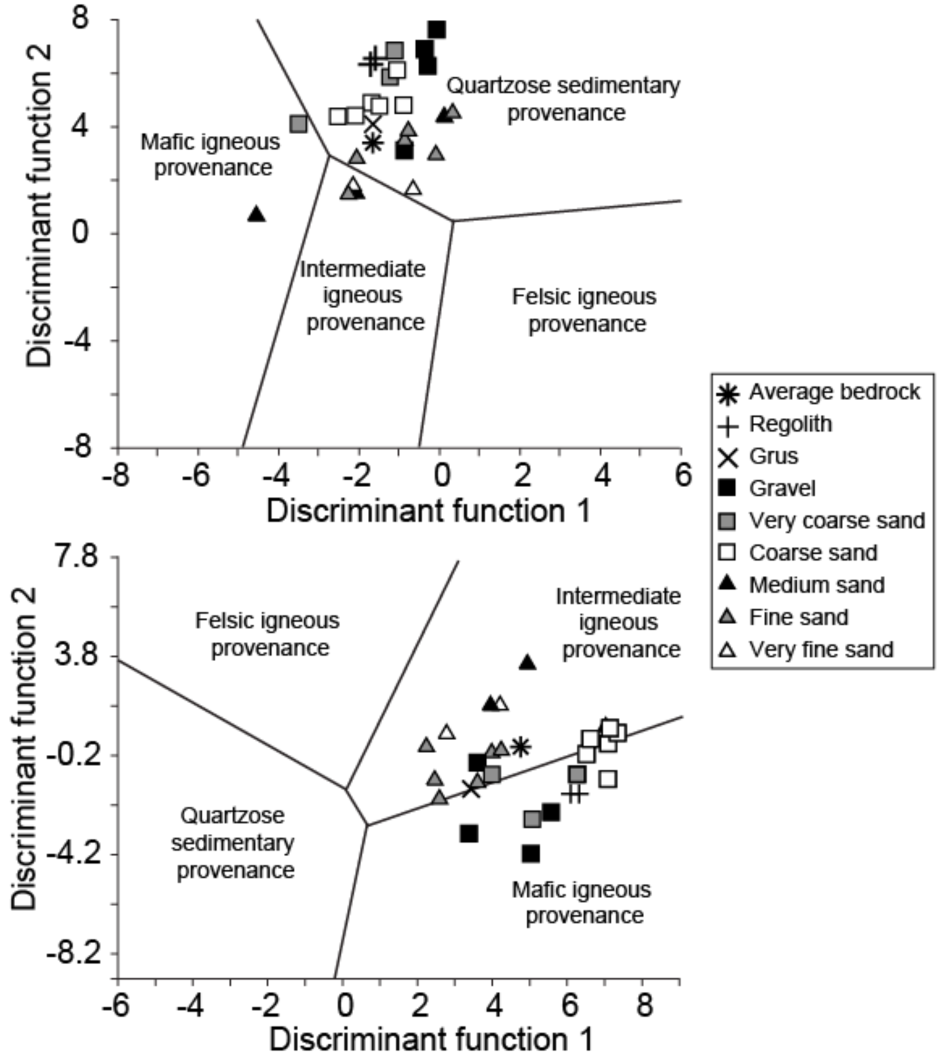

Figure A2.2. Discrimination diagrams after Roser and Korscg (1988) with sediment grouped according to average grain size.

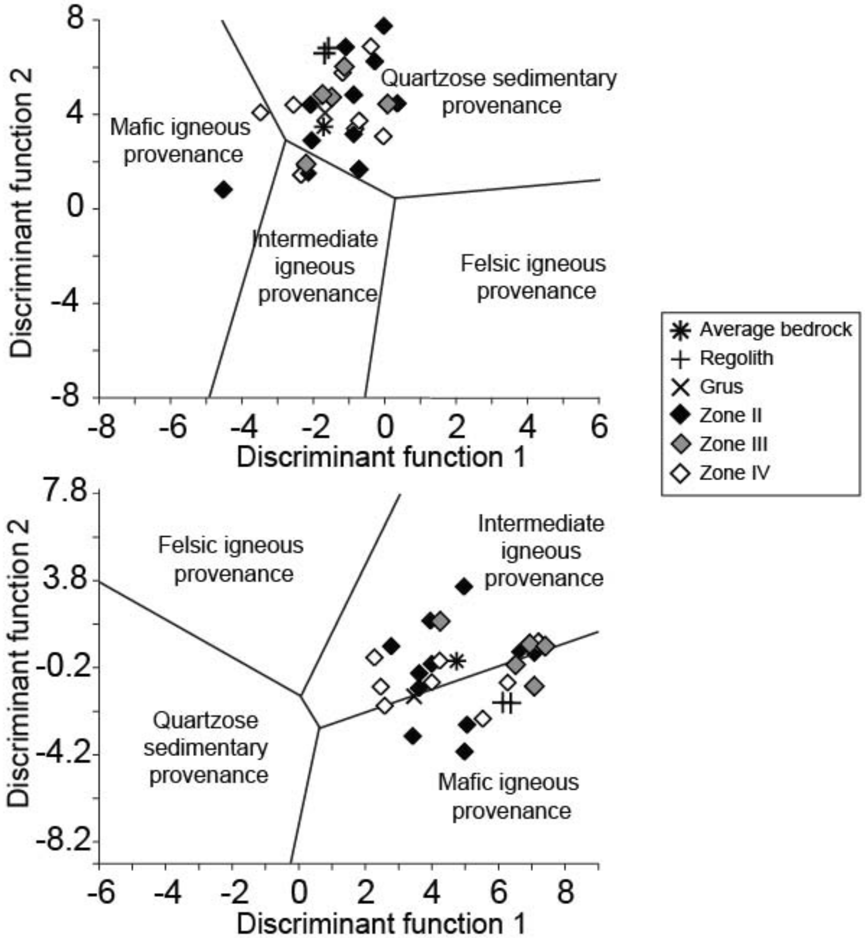

Figure A2.3. Discrimination diagrams after Roser and Korscg (1988) with sediment grouped according to geomorphic zone.

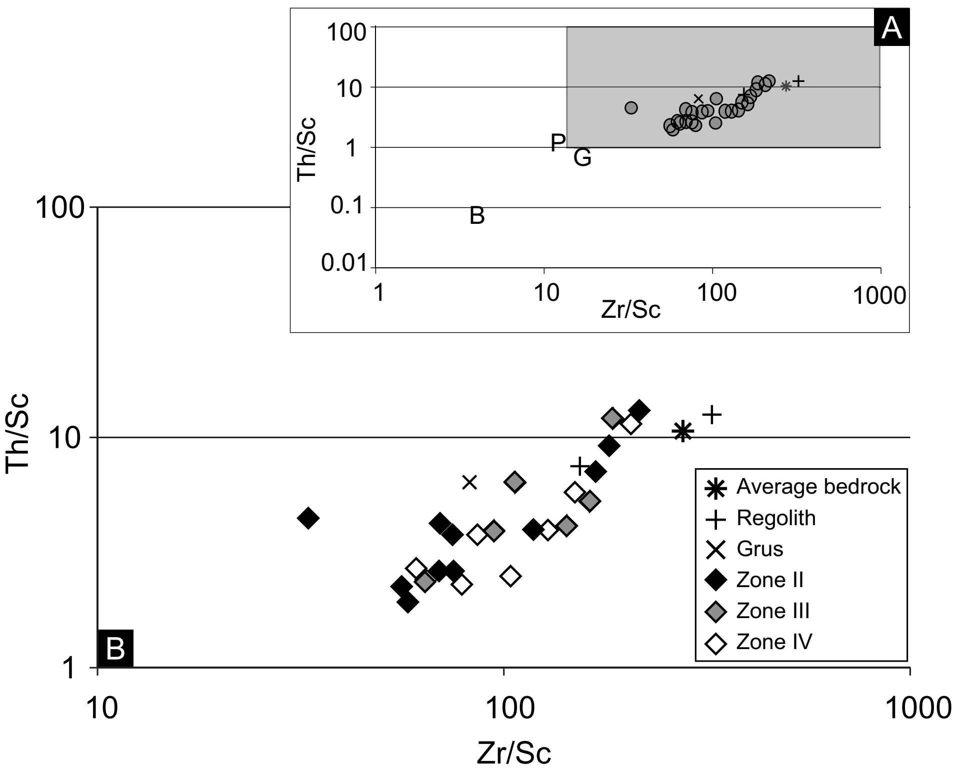

Figure A2.4. Plot of Th/Sc versus Zr/Sc — sediments grouped by geomorphic zone. (a) Diagram includes average Stepladder bedrock, regolith, grus, sediments, and average rock compositions (plotted for reference: B: Meso-Cenozoic basalt, G: Meso-Cenozoic granite, T: Phanerozoic TTG, and P: Post-Archean Australian average shale (PAAS)). Data from Condie (1993) and McLennan and Taylor (1989). Shaded gray box shows location of (b). (b) Detail of sediments plot with respect to geomorphic zone.

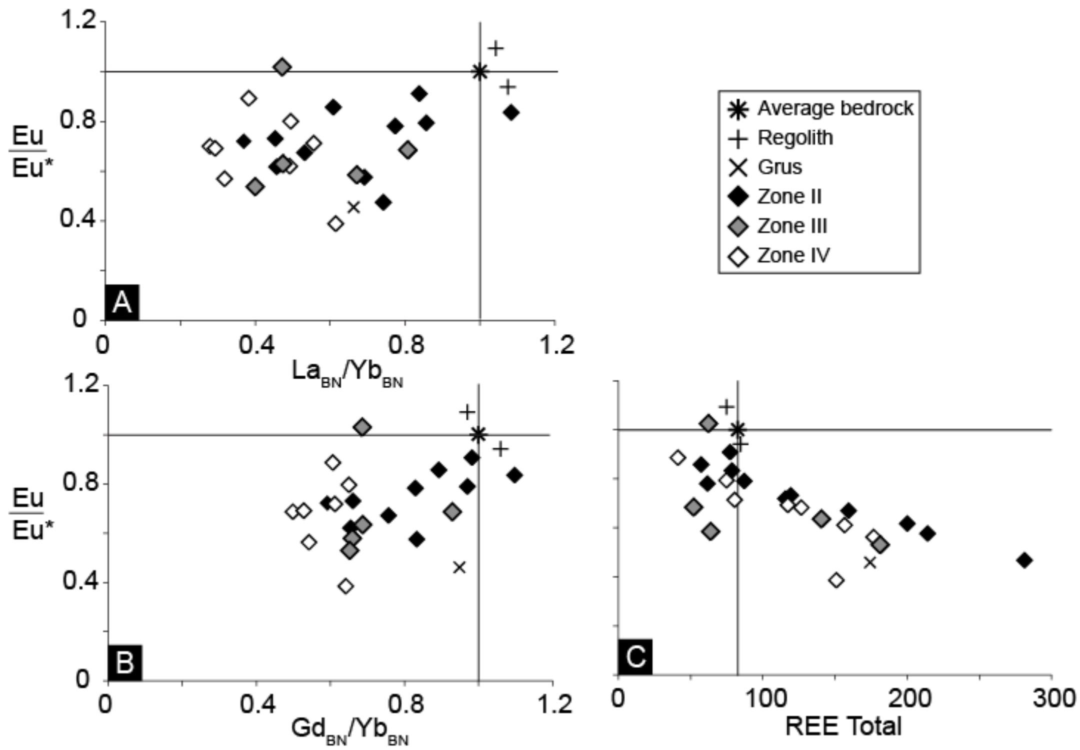

Figure A2.5. Eu* plots with sediments grouped by geomorphic zone and plot versus (A) $(La/Yb)_{BN}$ (B) $(Gd/Yb)_{BN}$ (C) REE Total.

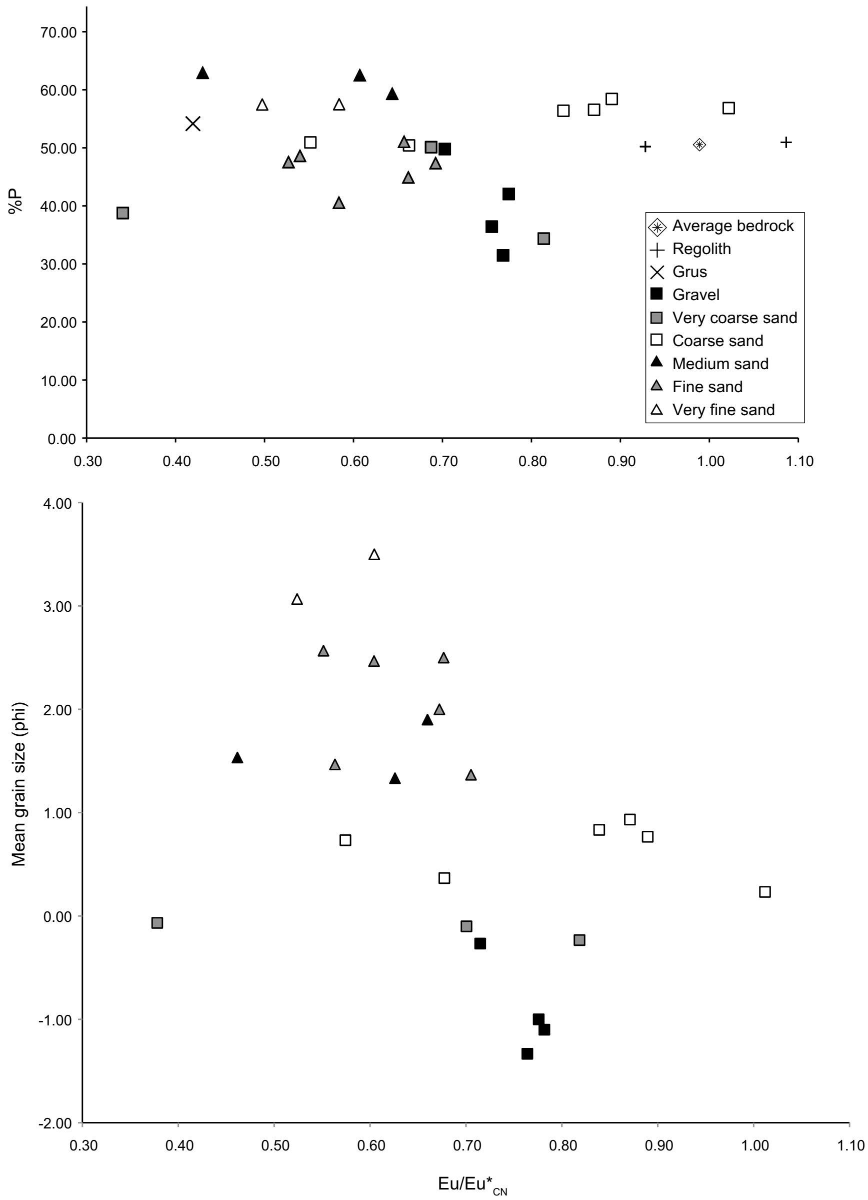

Figure A2.6. Eu* plots versus (top) percent plagioclase and (bottom) mean grain size.

Vita

Aubrey Modi was born in Atlanta, Georgia in September 1984 to Thomas and Anne Modi. She graduated from Chattahoochee High School in Alpharetta, Georgia, in 2002. Aubrey earned her Bachelors of Science in Geology at Sewanee: The University of the South, where she graduated cum laude with honors in 2006. While attending Sewanee, she was active in research within the geology department and was a member of the Order of the Gownsmen and the varsity equestrian team. Soon after graduation, Aubrey began her graduate research at the Department of Earth and Planetary Sciences at the University of Tennessee, Knoxville.